Table top system for angle resolved light scattering measurement

Dissertation

Zur Erlangung des akademischen Grades

Doktoringenieur
(Dr.-Ing.)

vorgelegt an der
Fakultät für Maschinenbau der
Technischen Universität Ilmenau

von Herrn
M.Sc. Alexander von Finck
geboren am 28.01.1980 in Würzburg

1. Gutachter: Prof. Dr. rer. nat. habil. Stefan Sinzinger, TU Ilmenau
2. Gutachter: Dr. rer. nat. Angela Duparré, Fraunhofer IOF Jena
3. Gutachter: Prof. Dr. sc. techn. Michael Pfeffer, Hochschule Ravensburg-Weingarten

Tag der Einreichung: 04.12.2013
Tag der wissenschaftlichen Aussprache: 21.05.2014

urn:nbn:de:gbv:ilm1-2014000214

Abstract

In the last decades, the measurement and analysis of scattered light gained importance. The lack of compact, yet comprehensive tools motivated this thesis to develop a highly universal table top instrument for angle resolved light scattering (ARS) measurement, as well as according measurement and analysis techniques.

A table top scatterometer with a compact footprint of 0.8x0.8 m^2 is described. It enables full 3D spherical detection at illumination wavelengths of 405 nm, 532 nm, and 640 nm.
With sensitivities limited only by Rayleigh scattering at air molecules, a dynamic range of 14 orders of magnitude was achieved. The compact layout of the scatterometer was realized by a specific arrangement of the axes where the optical path lengths are artificially increased by beam folding mirrors. The realized instrument is validated by a comprehensive performance analysis focused on instrument signature and measurement uncertainty. Corresponding optimizations are derived by means of simulations and analytic models.

Based on frequency division multiplexing, a concept is proposed that enables wavelength and/or polarization multiplexed ARS measurements. It allows parallel ARS measurements over the complete dynamic range and with high sensitivity.

A new quantity for anisotropy is introduced which is spatial frequency resolving and directly linked to scattering losses and roughness properties. It is utilized to discriminate four roughness components in ultra-precision diamond turned surfaces by 3D-ARS measurements. The impact of anisotropy as a function of the illumination wavelength is analyzed.

Experiments at three illumination wavelengths are conducted to provide highly relatable roughness information. The analysis is used to detect contamination on coatings and substrates, as well as to analyze roughness growth on thin film layers.

3D-ARS measurements are demonstrated to be capable of characterizing diamond cuts in all grading relevant categories. It is shown that light scattering analysis has a direct access to the optical performance of gemstone. A method is proposed that allows one to assess the polish of the individual facets from 3D-ARS measurements.

Kurzfassung

Die Messung und Analyse von Streulicht hat in den vergangenen Jahren wesentlich an Einfluss gewonnen. Der Mangel an Messsystemen die sowohl flexibel als auch kompakt sind, motivierte diese Arbeit zur Entwicklung eines winkelauflösenden Table-Top Streulichtmesssystems mit dazugehörigen Auswertemethodiken.

Das realisierte Table-Top Goniometer weist kompakte Abmaße von $<0.8\text{x}0.8\text{x}0.8\,\text{m}^3$ auf und ermöglicht die Messung von 3D-Streulichtverteilungen bei Beleuchtungwellenlängen von 405 nm, 532 nm und 640 nm. Mit erreichten Sensitivitäten, die nur durch die Luftstreuung begrenzt sind, wurde eine Dynamik von 14 Größenordnungen erzielt. Die kompakte Konstruktion wurde durch ein spezielles Achsdesign und über Faltung der Strahlengänge erreicht. Messunsicherheit und Instrumentesignatur wurden anhand von neu entwickelten Modellen und Simulationen analysiert. Darauf aufbauend erfolgten Optimierungen.

Basierend auf dem Frequenzmultiplex-Prinzip wurde ein Konzept zur Ermöglichung paralleler Streulichtmessungen mit hoher Sensitivität und Dynamik entwickelt. Hiermit lässt sich das gestreute Licht unterschiedlicher Beleuchtungswellenlängen und/oder -polarisationen in verschiedenen Messkanälen gleichzeitig detektieren.

Es wurde eine streulichtbasierte Analysemethode anisotroper Oberflächen eingeführt, die einen direkten Bezug zu optischen und rauheitsbeschreibenden Eigenschaften aufweist. Hiermit ließen sich erstmals Rauheitskomponenten unterschiedlicher Ursache bei ultrapräzisionsbearbeiteten diamantgedrehten Oberflächen als Funktion der Ortsfrequenz trennen. Der Einfluss von Anisotropie bei unterschiedlichen Beleuchtungswellenlängen wurde untersucht.

Über Streulichtanalyse mit mehreren Beleuchtungswellenlängen wurde eine hochrobuste Rauheitscharakterisierung demonstriert. Hiermit ließen sich Kontaminationen auf beschichteten und unbeschichteten Substraten sowie Rauheitswachstum in Dünnschichtfilmen nachweisen.

Es wurde gezeigt, dass sich Diamantschliffe über die Auswertung von 3D-Streulichtverteilungen charakterisieren lassen. Es können beispielsweise die Politurgüte einzelner Facetten sowie die optische Performance von Brillanten bewertet und klassifiziert werden.

Contents

1 Introduction

The last decade experienced an increasing demand of high-precision optical components. This affected the need of sensitive, fast, and flexible measurement tools for the quality assessment of surfaces, materials, and coatings. Light scattering techniques are however not only limited to quantify the negative impacts of scattered light in optical systems such as the reduction of contrast, resolution, or the optical throughput. A characterization by light scattering analysis moreover provides a highly sensitive and non-contact access to surface and material specifications.

With the availability of highly sensitive and dynamic photomultiplier tube detectors, the appearance of first publications of light scattering measurements dates far back to the 1940s [1]. Angle resolved light scattering measurements were e.g. used to study chemically related characteristics of polystyrene solutions [2], yet not much interest was gained in the optical industry. From today's perspective, the effective start of optical light scattering analysis was in 1961 [3], a few years after the laser was invented, where H. Bennett and Porteus reported an instrument to link light scattering losses to the rms surface roughness [4]. With the further development of adequate theories connecting light scattering to surface statistics [5,6], measurement of scattered light received increasing attention [7]. At first, the state-of-the-art instrumentation of the early 70s mostly lacked automation [6, 8, 9]. But with the growing availability of compact computers in the late 70s to 80s, the number of facilities for light scattering measurement and the diversity of according instrumentation increased [10, 11]. This resulted in 1987 in the first commercially available high-end scatterometer CASI [12], an abbreviation for "complete angle scatter instrument". This instrument was, however, limited to in-plane measurements. Nevertheless, to this day, this instrument has defined the state-of-the-art market with an only marginally modified robust design [13]. Light scattering theories were proven to work very accurately [14–16], and today laboratories around the world have dedicated themselves to the investigation of light scattering phenomena [17–20].

At present, a huge range of measurement tasks is covered by light scattering measurement techniques, from the process control of paper sheet or beer can fabrication [3, 21], over measurements for rendering applications [22], up to ultra sensitive particle scans for the silicon industry [23, 24]. Various kinds of instruments to measure scattered light have been developed: integrating light scattering spheres with specular or diffuse collector optics, matrix sensor based instruments with scattering angle or sample surface resolving capabilities, and fiber optics based compact sensor heads.

Most of these measurement concepts were tailored to very specific applications that often do not require sensitivity and always no flexibility. A few laboratories have developed comprehensive high-end scatterometers [18, 25–27] that allow to scan the whole 3D sphere surrounding the sample - with sensitivities down to the scattering at the air molecules. A demanding task, as the scattering characteristic of polished surfaces can cover dynamic ranges from the

10^{-10} fraction of the incident power up to the specular reflected beam, which makes stray light control, detection linearity, and beam preparation crucial. Because of their complexity and aspired universality, these systems have significantly increased in size and consequently lost capability for close-to-process application. For highly sensitive compact scatterometers, most of the anyway challenging specifications become even more demanding. Especially stray light control and beam preparation are affected by limited space. The few existing compact 3D angle resolving table top scatterometers were designed to characterize rather rough technical surfaces for rendering calculations [28, 29] and are consequently limited in sensitivity. Hence, there is a lack of compact, highly sensitive table top instruments for light scattering measurements with 3D spherical capability.

Nearly all surfaces, coatings, and materials reveal different light scattering characteristics at different illumination wavelengths and with different polarization parameters. Moreover, light scattering measurements performed at multiple illumination wavelengths or polarizations allow a more profound analysis to solve inverse scattering problems (e.g. to discriminate between different light scattering effects). State-of-the-art scatterometers only enable a sequential characterization with different measurement parameters, which typically involve more or less time-consuming refits of the instrument including realignments and recalibration. Current multiplexing concepts for instruments to measure scattered light by means of polychromators are very limited in dynamic range and sensitivity [29]. According polarization multiplexing approaches have not been published yet. There is consequently a demand for concepts that allow multiplexed or at least quickly changeable parameters in light scattering measurements with high dynamic range and sensitivity.

This work is therefore dedicated to the development of a compact and at the same time highly sensitive and comprehensive table top scatterometer with full 3D spherical capability. It is designed to meet the requirements for the characterization of optical and technical surfaces, components, and materials. To allow highly sensitive multiplexed light scattering measurements, a concept is tailored and implemented into the developed scatterometer.

The thesis is organized as follows:

After introducing the most important definitions, Sec. 2 reviews state-of-the-art instrumentation, standardization, and theories linking light scatter phenomena to surface statistics.

Sec. 3 discusses different concepts, including state-of-the-art approaches, considering their suitability to meet the requirements of a compact high-end table top instrument. Based on this research, the main components of the system layout are designed. Moreover, a novel concept for wavelength and polarization multiplexing in highly sensitive light scattering measurements is introduced. Afterwards, the instrument concept is validated by analyzing the performance of the realized system including a comprehensive measurement uncertainty model and an in-depth analysis of the instrument signature. Based on the performance analysis, systematic optimizations are introduced.

Sec. 4 utilizes the developed instrument for the investigation of optical components. A new quantity for anisotropy is introduced and used to describe and analyze the performance of ultra-precision diamond turned and float glass surfaces. The multi-wavelength capability of the instrument is used to detect contamination on coatings and substrates, as well as to analyze roughness growth on thin film layers. A new method for the characterization of gemstone cuts by light scattering techniques is introduced.

2 Basics

2.1 Light scattering

2.1.1 Definitions

The investigation of light scattering from optical components demands - as well as any other profound measurement technique - defined quantifies to yield repeatable and comparable measurements as well as to enable a quantitative post-measurement analysis. The most important definitions and nomenclature used in this work are introduced.

Geometry

The basic geometry for the definitions of the scattered and the specular beam directions [30] is shown in Fig. 2.1. The sample (1) is illuminated by a beam (2) at an angle of incidence θ_i. The specular reflected beam (3) leaves the sample at $\theta_R = \theta_i$. Scattered light is off-specularly redirected into the solid angle $\Delta\Omega_s$ at the polar and azimuth scattering angles θ_s and ϕ_s, respectively. The sample coordinates are denoted by X and Y.

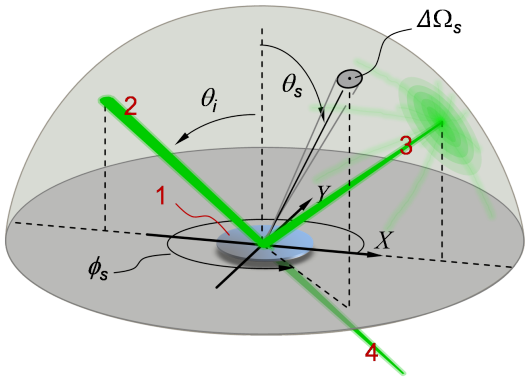

Figure 2.1: Basic geometry conventions: 1 - sample, 2 - incident beam, 3 - specular reflected beam, 4 - specular transmitted beam, θ_i - angle of incidence, θ_s - polar scattering angle, ϕ_s - azimuthal scattering angle, $\Delta\Omega_s$ - solid angle, X, Y - lateral sample coordinates.

Specular transmittance and reflectance

The specular reflectance R is defined by normalizing the specular reflected power P_R to the incident power P_i

$$R = \frac{P_R}{P_i} \ . \tag{2.1}$$

The specular transmittance T is accordingly defined as the specular transmitted power normalized to P_i.

Angle resolved scattering

The angle resolved scattering (ARS) is defined as the power ΔP_s scattered into the solid angle $\Delta\Omega_s$, normalized to $\Delta\Omega_s$ and P_i [16, 31]:

$$\mathrm{ARS}(\phi_s, \theta_s) = \frac{\Delta P_s\left(\phi_s, \theta_s\right)/\Delta\Omega_s}{P_i} \ . \tag{2.2}$$

Alternatively, the BSDF (bidirectional scattering distribution function) is sometimes used. It is defined as the radiance of the sample L_e normalized to the irradiance E_e and consequently contains an additional cosine factor [32]:

$$\mathrm{BSDF}(\phi_s, \theta_s) = \frac{L_e\left(\phi_s, \theta_s\right)}{E_e} = \frac{\Delta P_s\left(\phi_s, \theta_s\right)/\Delta\Omega_s}{P_i \cos\theta_s} \ . \tag{2.3}$$

Total scattering

Total backscattering TS_b is defined as the power P_b scattered into the reflection hemisphere and normalized to P_i

$$\mathrm{TS}_b = \frac{P_b}{P_i} \ , \tag{2.4}$$

where the total forward scattering TS_f is accordingly defined in the transmission hemisphere. TS_b can be calculated from the ARS by hemispherical integration within the appropriate limits according to ISO 13696 (see next chapter):

$$\mathrm{TS}_b = \int_{0°}^{360°} \int_{2°}^{85°} \mathrm{ARS}\left(\phi_s, \theta_s\right) \sin\theta_s d\theta_s d\phi_s \ . \tag{2.5}$$

For smaller integration ranges, the integrated scattering is denoted as S_b or S_f, respectively. Alternatively to TS, the total integrated scattering (TIS) is sometimes used. It is calculated by normalizing P_b to the diffuse reflectance instead of P_i, where the diffuse reflectance is approximated by P_R [4]. Hence, TS_b and TIS can be converted into each other if the reflectance of the surface is known. However, TIS is not defined in forward scattering direction.

Energy balance

The sum of the specular components, TS, and absorption A yield unity, which is usually referred to as the energy balance:

$$R + T + A + \mathrm{TS}_b + \mathrm{TS}_f \ = 1 \ . \tag{2.6}$$

2.1.2 Standardization

ARS / BSDF

A standard procedure for angle resolved scattering measurements was defined in ASTM standard E1392 [33]. It was successfully implemented and verified in various round-robin experiments at different wavelengths [26, 34], though it is restricted to opaque samples only. In the late 1990s, several documents relating to the semiconductor industry were moved from ASTM to SEMI standards, which was also the case for ASTM E1392 that became SEMI ME1392 [35] and was rewritten to cover a wider range of applications [3]. A few years later, the similar ASTM standard E2387 was published with only minor differences [30], however, both standards are active. Currently, an ISO standard procedure for ARS measurements is being developed by the international working group TC172/SC9/WG 6 of the International Organization for Standardization [36].
The referred standards contain information about nomenclature and terminology, instrument layouts, and measurement procedures. However, the probably most important issue discussed is calibration, where the standards suggests four different methods. Considering Eq. (2.2), the detectors of a scatterometer measure voltages (or currents) rather than absolute powers. As $\Delta P_s/P_i$ equals V_s/V_i , where V_s and V_i represent the appropriate detector signals, the ARS can be calculated by:

$$\mathrm{ARS} = \frac{\Delta P_s/\Delta\Omega_s}{P_i} = \frac{V_s/\Delta\Omega_s}{V_i} \ . \tag{2.7}$$

The proposed calibration routines in the ASTM can be roughly categorized into two groups (the exact calculation can be reviewed in [30, 35]):

Incident power normalizations assume that $\Delta\Omega_s$ was previously determined from geometric considerations, and V_i is determined by recording the specular beam signal without a sample ("absolute normalization"). If the scatterometer does not allow to move the detector into the incident beam, it is suggested to alternatively determine V_i by measuring the signal of the specular reflected beam of a sample with known reflectance ("specular normalization") [30,35].

Reference calibrations determine $\Delta\Omega_s \cdot V_i$ by measurement of a sample with either known ARS/BRDF ("relative normalization") or known diffuse reflectance ("diffuse reflectance normalization"). This allows traceability to a national or international standard, which is e.g. mandatory for ISO17025 certified calibration laboratories [37].

TS

TS is defined in the international standard ISO 13696 [38] according to Eq. (2.4), where the range of scattered radiation to be detected (range of acceptance angles) is defined as $0° \leq \phi_s < 360°$ with polar scattering angles covering *at least* the section between θ_s=2° and θ_s=85° in the corresponding backward or forward hemispheres. However, the specular beam may not be truncated, and the standard suggests to specify the acceptance angle range with

TS values. In this work, TS values calculated from ARS data are integrated from 2° to 85° by means of Eq. (2.5).

2.1.3 Light scattering measurement principles

This sub-chapter provides an overview of different state-of-the-art light scattering measurement principles. They are discussed regarding their general properties and functionality.

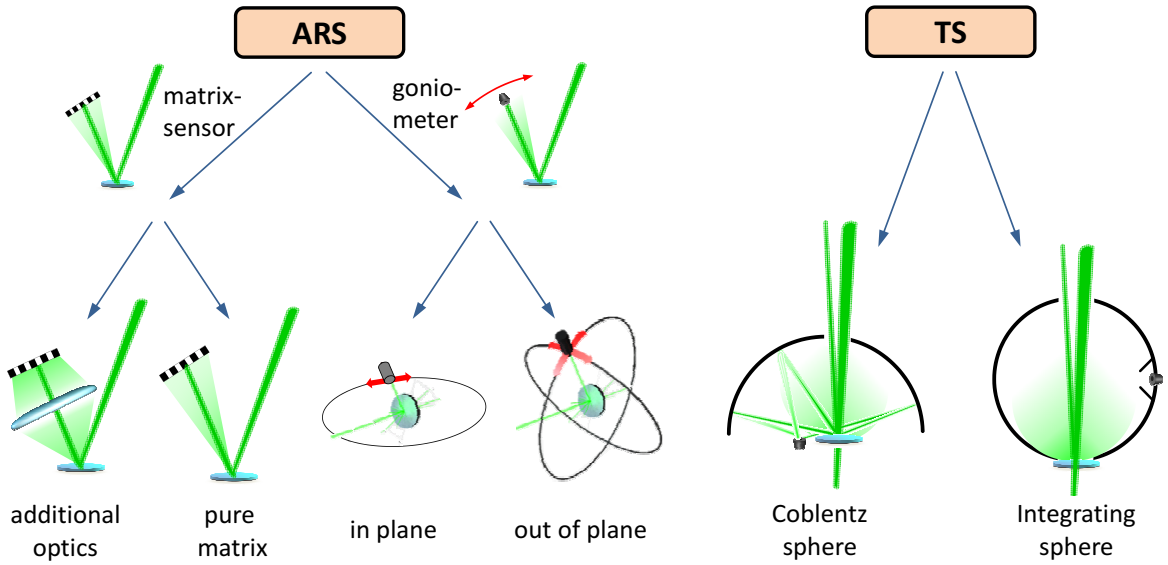

Figure 2.2: Overview of different techniques for light scattering measurement

Light scattering measurement principles can to a large extent be divided into angle resolved (ARS / BRDF) and total integrating (TS / TIS) scattering techniques (see Fig. 2.2) [7,17,39]. ARS measurements are originally performed by means of a scanning detection system on a goniometer arm but are also possible by means of a matrix sensor. Matrix systems can be further subdivided into sensors with and without additional optics to increase the observable ARS section, while goniometers are separated into instruments with in-plane and 3D measurement capability. For TS measurements integrating optics are used to collect the total scattered light in the reflection (backward scattering) and / or transmission hemisphere (forward scattering). Either diffuse (Ulbricht or integrating sphere) or reflective optics (Coblentz sphere) are used to collect the scattered light. The individual light scattering techniques are discussed in this chapters in more detail.

TS / TIS instrumentation

In 1961, Bennett and Porteus described the first instrument where the scattered light of a sample is integrated by a reflective hemisphere [4]. They defined a measure called TIS and linked it to rms roughness value of the sample by scalar diffraction theory. Various arrangements for TS and TIS measurements have been reported in the recent decades from a number of laboratories with reported sensitivities of <0.1 ppm and wavelength ranging from 157 nm to 10.6 µm [40–46].

They mainly differ in the used integrating optic, which is either a Coblentz or an integrating sphere (or Ulbricht sphere) to collect the scattered light. The Coblentz sphere is a hemispherical mirror, which images the sample illumination spot onto the detector for scattering angles of 2° to 85° according to ISO13696 (see chapter 2.1.2). The integrating sphere (or Ulbricht sphere) is a spherical optic with a highly reflective (typically 99% for the VIS and the NIR spectrum) diffuse coating, that distributes the scattered light homogeneously inside the sphere. The field of view (FOV) of the detector is hereby limited by baffles, to prevent light to directly scatter from the sample onto the detector. Unlike Coblentz spheres, the sample is not imaged onto the detector, which results in a lower alignment sensitivity and therefore smaller and more feasible sphere sizes. However, the diffuse scattering process in the sphere reduces sensitivity and increases the Rayleigh scattering limited, which is in contrary reduced by the limited detector FOV in the Coblentz sphere. Additionally, the range of possible illumination wavelengths is more restricted by the diffuse than by the reflective coating.

Sometimes a smaller section of scattering angles is covered by the collection optics, which is accordingly not ISO13696 conform but yields a more compact system layout. Consequently, TS values can only be estimated by assuming scattering distributions and introducing corresponding correction factors [47].

The beam preparation system is similar to ARS-goniometers described in the next section, with special care taken on beam stops and apertures to minimize the background signal. TIS instruments unlike TS instruments would include an additional detector to capture the reflected beam.

As TS / TIS instruments use integration optics, angle resolved light scattering measurements are, of course, not possible. An interesting concept to impair this drawback involves a spinning device inside the Coblentz sphere, which obscures different azimuthal fractions of the reflection hemisphere to enable at least anisotropy sensitivity [48].

ARS-goniometer

ARS measurement based on goniometer type instruments is probably the oldest light scattering measurement technology. Early angle resolving goniometers for the analysis of polystyrene solutions are reported back in the 1940s [1, 2, 49]. Sensitivities were - of course - limited at that time. Interestingly, these instruments were already based on “recently developed” photo multiplier tubes (PMT) and lock-in-amplifier (LIA) resembling metrology [2]. Therefore, it was exploited that the light source was naturally modulated at 120 Hz by the local AC power line, instead of using external optical modulators as in today state-of-the-art light scattering instruments. In the late 80s, the first high-end scatterometer CASI (Complete Angle Scatter Instrument) was developed [12], enabling highly sensitive in-plane ARS light scattering measurements. The instrument was designed modular, so the illumination and detection system are separated and consequently the whole system is typically operated on optical benches. 3D scattering measurements are not being supported with this scatterometer.

A schematic sketch of a mirror based goniometer for light scattering measurements is shown in Fig. 2.3. Different lasers (1) ranging from 325 nm up to 10.6 µm are typically implementable

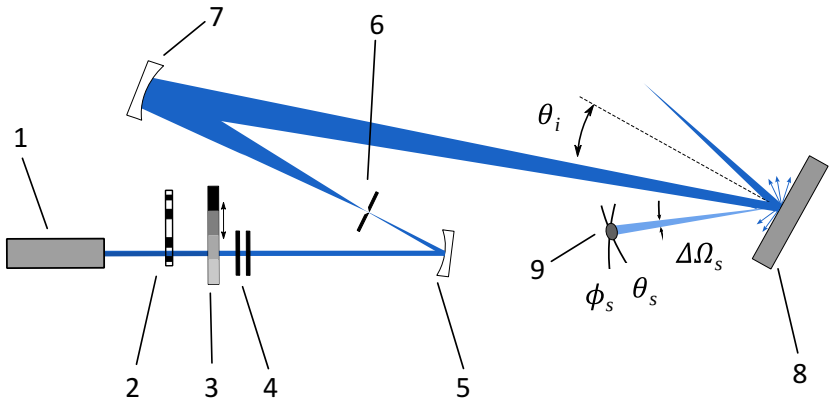

Figure 2.3: Schematic picture a goniometer for light scattering measurements.

as light sources [13, 18, 27]. Yet, instrumentation operating at 193 nm, 157 nm, and even at 13.5 nm has also been developed [45, 50–52]. For extremely sensitive light scattering measurements a high signal-to-noise ratio is necessary, which is achieved by using a chopper (2) and lock-in amplification of the detected signal. Power drifts of the laser are sometimes compensated by a reference detector. Additional attenuators (3) are essential to spread the dynamic range over several orders of magnitude by adjusting the incident power according to the detector signal. To obtain a clean and homogeneous laser beam for sample illumination, special effort is taken on elaborated beam preparation systems. For the system optics, mirrors are usually being preferred over lenses to support a broader wavelength range. A spatial filter is used comprising a mirror (5) and a pinhole (6) to clean out higher order wavefront errors and stray light of the beam preparation system optics. The pinhole is imaged onto the detector aperture (9) by means of a mirror (7). Different baffles are used to adjust the spot size on the sample surface (8) and to block residual stray light from the illumination system. Illumination and detection polarization can be adjusted from s- to p-polarization by means of a polarizer (4) and an analyzer, located in the illumination and the detection system, respectively. A sample positioning system allows to automatically adjust the illumination spot position as well as the angle of incidence. Raster scans e.g. for homogeneity analysis are provided by scanning the sample with the illumination spot while θ_i and θ_s are kept fixed. The receiver (9) is typically based on photo multiplier tubes (PMT) or photo diodes, where the field of view (FOV) is limited by either baffles or by means of a field lens [30]. 3D or 2D positioning systems are used to enable spherical or at least in-plane scans, respectively.

A variety of goniometric instruments for angle resolved light scattering measurement have been developed at the Fraunhofer IOF, enabling ARS analysis from the EUV (λ=13.5 nm) up to wavelengths in the FIR (λ=10.6 µm) region [27, 45, 50]. All of these comprehensive but rather large and complex scatterometers were designed for laboratory purposes rather than for application close to fabrication processes. This also holds for the majority of light scattering goniometers described elsewhere. An overview of achieved specifications of the most important ARS goniometers is given in Table 2.2. The individual concepts are discussed in Chapter 3.2 in more detail.

Prior to this thesis, there has been no table top system with full 3D spherical capability and high sensitivity.

Table 2.1: Overview of the most important ARS instruments developed at Fraunhofer IOF and in other laboratories. The instruments are being compared regarding the most relevant specifications: λ - illumination wavelength, DR - dynamic range, ARS signature limit (at λ=532 nm or closest), MR - accessible measurement regime.
BB - broad band source, OPO - optical parametric oscillator laser (tunable), SC - supercontinuum laser (tunable), IP - in-plane detection capability, 3D - hemispherical or spherical detection capability, † - no VIS instrument, "-" - unpublished specifications, * - best value estimated from published measurements (in the VIS spectrum if applicable).

Instrument	Laboratory	λ (µm)	DR (OOM)	Signature limit (sr^{-1})	MR
ALBATROSS [27]	IOF	0.325 – 10.6	15	10^{-8}	3D
MERLIN † [50]	IOF	0.0135	7†	10^{-4}†	IP
DUoSTAR † [45,53]	IOF	0.157, 0.193	12†	10^{-7}†	IP ([1])
CASI [12,13]	SMS	0.325 – 10.6	14	$5 \cdot 10^{-8}$	IP
TASC [25,54]	SMS	0.325 – 10.6	-	$2 \cdot 10^{-7}$	3D
TASC [55,56]	"	0.23 – 14.0 (BB)	-	$<7 \cdot 10^{-5}$ *	3D
GOSI [19,26,57]	NIST	0.325 – 0.633	-	$<10^{-8}$ *	3D
- [58,59]	NIST	0.380 – 1.050 (BB)	7	-	3D
REFLET [29,60]	LightTec	0.42 – 1.7 (BB)	- ([2])	-	3D
Gonio2π-BSDF [61]	OPSIRA	-	11	-	3D
- [62] †	Institut Fresnel	0.847	-	$3 \cdot 10^{-8}$ †	IP
- [18,63]	Institut Fresnel	0.325 – 10.6	>7	$<10^{-7}$ *	3D
- [64]	Institut Fresnel	0.480 – 2.000 (SC)	12	$<10^{-6}$ *	IP
- [65]	PTB	0.250 – 1.700 (BB)	-	-	3D
OMS4 [66]	OPTIS	0.633	7	-	3D
"	"	0.360-1.040 (BB)	-	-	"
- [20]	LZH	0.633, 1.064	>11 *	-	3D
Lambda950 [67]	PerkinElmer	0.175– 3.300 (BB)	-	-	IP
- [68]	The Aerospace Corporation	- (OPO)	-	10^{-5}	-
pgII [69]	pab Ltd.	0.532, 0.650, BB	>8 *	-	3D

ARS-matrix sensors

Recent sensitivity improvements of matrix sensors enable 3D-ARS measurements with increased sensitivity where the light scattering distributions are spatially resolved by means of a CCD or a CMOS sensor [70–73]. This concept allows quick one-shot 3D-ARS measurements in a couple of seconds, whereas goniometer based 3D-measurements typically range in the order of several hours. However, the size of the recordable ARS sections and the noise equivalent ARS level are too restricted to allow ARS matrix sensors to replace the more general goniometer type instruments.

Beam preparation systems are designed analog to those in goniometer type instruments. Sometimes additional optics are used to expand the measurement regime up to even hemispherical measurement capability [74,75]. Detectable ARS sections without additional optics are limited by the finite chip size but therefore achieve a better near angle signature. Scattering angle sections of about ±5° to ±12° around the specular beam can be recorded with

[1] The instrument also features a Coblentz sphere for TS measurements.
[2] A dynamic range of 9 OOM is specified if the scattered power of the broad band illumination is spectrally integrated by a wavelength blind detector (restricted post measurement analysis).

this concept [76, 77]. Herffurth et. al. introduced a special design comprising a second illumination source at a grazing angle of incidence. This allows to extend the spatial frequency range to regions that are e.g. relevant for the characterization of thin film coatings [70, 77]. A noise equivalent ARS of about $10^{-4}\,\mathrm{sr}^{-1}$ was reported, which allows the characterization of optically smooth surfaces (inside the limited ARS section). Most of the matrix sensors described elsewhere are limited to the characterization of rough surfaces and are typically used to obtain data for render calculations. The sensor ScatterScope3D [71, 78] uses a 635 nm laser source and allows 3D-ARS measurements in a scattering angle section of ±20° from the specular beam. The sensor achieves sensitivities between $10^{-2}\,\mathrm{sr}^{-1}$ to $10^{-3}\,\mathrm{sr}^{-1}$ as a function of the scattering angle.

An overview of the most important matrix sensors is given in Table 2.2.

Table 2.2: Overview of the most important matrix sensor based instruments developed at Fraunhofer IOF and in other laboratories. The instruments are being compared regarding the most relevant specifications: λ - illumination wavelength, DR - dynamic range, NEARS - noise equivalent ARS level, and the accessible measurement regime. The measurement regime is quantified in sr or the scattering angle section around the specular beam. BB - broad band source, "-" - unpublished specifications.

Instrument	Laboratory	λ (µm)	DR (OOM)	NEARS (sr^{-1})	Measurement regime
horos [70, 77]	IOF	0.650, 0.405	5	$<10^{-4}$	±5°
ScatterScope3D [71, 78]	The Scatter Works	0.635	6	$\approx 10^{-2}$ to $\approx 10^{-3}$	±20°
LARISSA [79, 80]	HSU-HH	0.488, 0.670, 0.810	7	-	$\approx\pi$ sr
PSS [76]	HSU-HH	0.686, 0.820	7	-	±12°
IS-SA [75]	Radiant Imaging	BB	- ([3])	-	$\approx 2\pi$ sr
OS-500 [81]	Optosurf	- (LED)	-	-	-

Other light-scattering measurement techniques

An interesting concept to measure scattered light was reported by Zerrad [62], where the sample is imaged by a camera based receiver. Instead of scanning the detector, the angle of incidence is goniometrically scanned between $|\theta_i|$=13.5° and 90° while the camera stays fixed at θ_s=0°. This allows to avoid pixel assignment errors (e.g. by image distortion) and allows to obtain a spatial resolved ARS(θ_i) to generate e.g. roughness maps [82]. However, OOP scans are not possible and the near angle signature is restricted by the camera objective.

Different instruments are reported that were designed with multiple receiver heads [83], which basically aim at reduced measurement times. The receivers are sometimes fixed and located at different scattering angles [84–88]. This enables one-shot ARS measurements at a trade-off of resolution. If the sample is additionally scanned, the measured data can be used to calculate roughness maps.

Similarly, particles can be detected on silicon wafers by scanning the whole sample with the illumination beam focused on the surface [3]. Exploiting the different scattering mechanisms under polarized illumination, this allows to discriminate between particles, pits, and surface roughness.

[3] The pure CCD sensor is specified with a dynamic range of 16 bit, which corresponds to 4.8 OOM.

A variety of commercial instruments has been developed to analyze the dynamic light scattering and/or the scattering distribution of small particles or polymers in solution (e.g. [89,90]). The time dependent fluctuations (caused by Brownian motion) and the light scattering distribution allow to determine e.g. the molecular size distribution and the molecular weight of dissolved molecules. Those highly specialized instruments are usually very restricted in their application and consequently not further described here.

Discussion

The major advantage of TS/TIS instruments is the high sensitivity combined with fast measurements. This e.g. allows surface roughness maps to be quickly obtained. Of course, ARS measurements are not possible. ARS matrix sensors lack universality because (i) the measurement regime and the ARS resolution are typically coupled parameters; (ii) hemispherical measurements require additional optics which limit the near angle signature; and (iii) matrix sensors are usually limited in sensitivity. ARS goniometers are considered as the most universal light scattering measurement technique. They are unique regarding dynamic range, sensitivity, measurement regime, and resolution.

The conception of the table top instrument for light scattering measurement in chapter 3 is accordingly restricted to goniometer type instruments only.

2.2 Relations between roughness and light scattering

For the qualified and quantified interpretation of light scattering phenomena discussed in chapter 3 and 4, theoretical models are required that allow to connect experimental observations to their origins. Scattered light arises from various surface and material imperfections, including surface roughness, bulk inhomogeneity, contamination, sub-surface damage, and defects. However, the examples discussed in this work are focussed on the analysis of surface roughness, which is typically the dominating scattering mechanism for high-quality optics. The according theory is briefly summarized in this chapter. Therefore required roughness describing quantities are introduced first.

2.2.1 Roughness

The rms roughness is defined as the standard deviation of the surface topography $z(x, y)$ from its mean value $\bar{z}$:

$$\sigma_\infty^2 = \lim_{L_x, L_y \to \infty} \frac{1}{L_x L_y} \int_{-L_x/2}^{L_x/2} \int_{-L_y/2}^{L_y/2} (z(x,y) - \bar{z})^2 \, \mathrm{d}x\mathrm{d}y \ , \tag{2.8}$$

where L_x and L_y denote the lateral surface dimensions. It is probably the most widespread form of describing roughness, although it contains only integrated vertical information. A more general form including both vertical and lateral roughness information constitutes the power spectral density function (PSD), which is simply the squared modulus of the Fourier transform of the surface:

$$PSD_{2D}(f_x, f_y) = \lim_{L_x, L_y \to \infty} \frac{1}{L_x L_y} \left| \int_{-L_x/2}^{L_x/2} \int_{-L_y/2}^{L_y/2} z(x,y) e^{-j2\pi(f_x x + f_y y)} \mathrm{d}x\mathrm{d}y \right|^2 \ . \tag{2.9}$$

The PSD expresses the power of different roughness components as a function of the (lateral) spatial frequencies f_x and f_y of the surface. Most surfaces are generated by stochastic processes, such as grinding, polishing, etching or thin film depositions, which causes the PSD to exhibit a polar symmetry. These so called isotropic surfaces can be described by 2D-isotropic PSDs as a function of f_r, which are simply azimuthally averaged 2D-PSDs

$$PSD(f_r) = \frac{1}{2\pi} \int_{2\pi} PSD_{2D}(f_r, \phi) \, \mathrm{d}\phi \ , \tag{2.10}$$

with the polar coordinate transformation:

$$f_r = \sqrt{f_x^2 + f_y^2} \quad , \qquad \phi = \arctan\left(\frac{f_y}{f_x}\right) \ . \tag{2.11}$$

Integration of the PSD results in the rms roughness σ

$$\sigma = \sqrt{2\pi \int_{f_{min}}^{f_{max}} PSD(f_r) \cdot f_r \, \mathrm{d}f_r} \ , \tag{2.12}$$

which yields σ_∞ for the special case of $f_{min} = 0$ and $f_{max} = \infty$. However, real world

measurement techniques are *always* limited in the accessible spatial frequency range within f_{min} and f_{max}. This is traceable to both numerical limitations in sampling and size of L_x and L_y by the finite measurement field, as well as to physical limitations. E.g. the vertical waviness in the lateral positioning range ("scanner bow") of atomic force microscopes (AFM) and the finite size of the AFM tip; or the limited optical resolution of a white light interferometer (WLI) and residual wave front errors in the optical system. Consequently, the rms roughness is also always bandwidth limited, which - of course - holds for both derivations of σ by either Eq. (2.8) or (2.12).
Another common roughness descriptive measure is the autocorrelation function ACF of the surface [39], which represents a Fourier pair to the PSD. Because of the strong theoretical connection of the ARS to the PSD (see next section), as well as the better comparability of different measurement techniques, the PSD is used throughout this work.

2.2.2 Light scattering

In the last century, approximations based on scalar physical optics and vector perturbation theories were developed to describe the relation between light scattering and surface roughness. The best known are the scalar Beckmann-Kirchhoff approach [5] and the Rayleigh-Rice perturbation theory [91]. The latter also includes polarization properties of incident and scattered light while the former works for rougher samples. Originally used in radar applications to analyze the scattering of the sea, Church was the first who introduced vector perturbation for optical wavelength regimes in the mid 70s [6, 92, 93]. Identical perturbation results were later published by Elson and Bennett [94]. Because these theories are based on first order perturbation models, they are limited to smooth surfaces only with $\sigma \ll \lambda$ (which, however, holds for the vast majority of optical surfaces). They were later experimentally verified to be very accurate [3, 16, 95], and resulted in the sometimes called "golden rule" [3, 96] which connects the ARS to the PSD via a linear relationship

$$ARS(\phi_s, \theta_s) = \frac{16\pi^2}{\lambda^4} \cos\theta_i \cos^2\theta_s \, Q \, \mathrm{PSD}(f_x, f_y) \ , \tag{2.13}$$

where Q is an optical factor containing material constants, as well as scattering and polarization geometries. The spatial frequencies and the scattering angles are linked by the grating equation for first order diffraction

$$\begin{pmatrix} f_x \\ f_y \end{pmatrix} = \frac{1}{\lambda} \begin{pmatrix} \sin\theta_s \cos\phi_s - \sin\theta_i \\ \sin\theta_s \sin\phi_s \end{pmatrix} \ , \tag{2.14}$$

which - together with Eq. (2.9) and (2.13) - leads to the simple relationship of the ARS and the Fourier transform of the surface:

$$ARS \propto |\mathcal{F}\{z(x,y)\}|^2 \ . \tag{2.15}$$

Considering that integration of the ARS yields TS, and integration of the PSD yields σ, the link of TS to the rms roughness is not surprising:

$$\mathrm{TS}_b = R\left(\frac{4\pi\sigma}{\lambda}\right)^2 \ , \tag{2.16}$$

which holds for normal incidence. Later on, models were developed to work also in higher regimes of surface roughness for forward calculation [97, 98].

In contrast to single surface scattering, predicting light scattering from multilayer coatings is more complex as interference effects have to be considered [99–103]. The ARS of a thin film stack of M layers is given by [100]:

$$ARS(\phi_s, \theta_s) = \sum_{i=0}^{M}\sum_{j=0}^{M} Q_i Q_j^* \,\mathrm{PSD}_{ij}(f_x, f_y) \ , \tag{2.17}$$

where Q_i denotes the optical factor at the i-th interface and Q_j^* the conjugate complex optical factor at the j-th interface. The PSD_{ij} represents the PSD function of the i-th interface (for $i = j$) and its cross correlation properties ($i \neq j$). If the interfaces are fully correlated, Elson stated that for scattering "reasonably near the specular direction" the scattered light of a multilayer coating will behave like a single opaque surface with a corresponding effective reflectance and the same PSD [104] (single surface approximation).

It is obvious that Eq. (2.17) leads to an impracticable high number of parameters growing with M^2, except for the special case of single films [105, 106]. A simplified model with a reduced number of parameters was published [50] that allows to retrieve information of multilayer coatings if the design and the top layer PSD are known. Therefore, the parameters δ and β were introduced, describing the average deviation of the layer thickness from the design, and the roughness growth properties from interface to interface, respectively. By forward calculation of Eq. (2.17), the parameters are iteratively adapted until a good fit to the measurement is achieved.

3 Conception and realization of a new table top instrument

This chapter describes the conception of a highly sensitive table top scatterometer with full 3D spherical capability. As has been already announced in chapter 2.1.3, the concept analysis will only include goniometers, which constitute the most general and flexible ARS instrument type.

The requirements for the development of a high-end table top scatterometer are being discussed resulting in definitions of target parameters of the instrument. The following conception discusses and evaluates concepts, including state-of-the-art approaches, to achieve those target parameters. Based on the conception, the design of the main systems of the instrument (axes arrangement, illumination system, detection system) are described. Additionally, a novel concept to enable multiplexed light scattering measurements with high sensitivity and dynamic range is proposed. The performance of the realized instrument, including a measurement uncertainty analysis, is discussed in more detail. Based on the performance analysis, optimizations are being introduced.

3.1 Requirements & objectives

For the development of a high-end table top scatterometer, that aims for a flexible characterization of high quality optics comparable to laboratory instrumentation, specific requirements need to be met. In the following, the requirements are being discussed resulting in definitions of target parameters of the instrument.

1. Sensitivity and dynamic range
   The ARS of a superpolished aluminum surface with rms roughness of σ_{rel}=0.1 nm (for 0.066 µm$^{-1} < f_r <$ 1.88 µm^{-1} and a constant PSD slope of -2 in log-log scale) exhibits levels down to about 10^{-7} sr^{-1}. For small detector apertures with a full angle of $\Delta\theta_s$=0.1° the maximum detectable ARS level is calculated by $1/\Delta\Omega \approx 4 \cdot 10^5$ sr^{-1}. Hence, a scatterometer capable of measuring high quality optics needs a sensitivity and dynamic range of:
   - Noise equivalent ARS level of $<10^{-7}$ sr^{-1} for λ=532 nm and other illumination wavelengths in the VIS spectrum.
   - Dynamic range of at least 12.5 OOM.
2. Beam quality
   The width of the specular beam at the detector aperture determines the near-angle limit for ARS measurements. It is typically reduced by focussing the incident beam on

the detector aperture plane, while the spot size on the sample should yield about 3 mm in diameter [30]. However, the beam convergence should be small (NA'<0.01) so that no relevant effect on the measurement uncertainty has to be expected [30]. The illumination system has to be accordingly capable of compensating curved sample surfaces by adjustment of the beam focus position. In order to enable a roughness equivalent spatial frequency range of at least 2 OOM for λ=532 nm, the range of scattering angles between θ_{min} and θ_{max} that needs to be covered can be calculated by the grating equation. For θ_{max}=85°, the smallest scattering angle that has to be detected is θ_{min} =0.5°. Hence, to achieve the required beam quality a scatterometer needs to exhibit the following parameters:

- Detector arm length of at least 150 mm to enable NA'<0.01 for an illumination spot size of 3 mm in diameter.
- Specular near angle signature smaller than 0.5° from the specular beam.
- Beam focus position adjustable.

3. Spectral purity
   Light scattering strongly varies with λ regarding the ARS level, as well as the scattering angle for a fixed spatial frequency. A poor spectral purity broadens diffraction orders of e.g. gratings and is accordingly capable to superimpose scattered light of a sample. The acceptable relative spectral linewidth $\Delta\lambda/\lambda$ of a source that causes the diffraction order located at the diffraction angle θ_s to be broadened by $\Delta\theta_s$ can be calculated by the grating equation. For θ_s=80° and $\Delta\theta_s$=±0.5° the acceptable relative spectral linewidth results in $\Delta\lambda/\lambda$≈3000 ppm [1].
   - Illumination with λ=532 nm and $\Delta\lambda/\lambda$<3000 ppm (corresponds to $\Delta\lambda$=1.6 nm for λ=532 nm).

4. Measurement regime
   Most light scattering distributions of optical and non-optical components can be assumed as isotropic over the reflectance and transmission hemispheres, which allows a sufficient characterization by IP ARS instruments. However, as soon as anisotropic roughness components, complex surface geometries or non-zero angles of incidence generate anisotropic light scattering behavior, OOP measurements become increasingly mandatory [107, 108]. A flexible scatterometer has to be capable to perform 3D measurements in both the transmission and the reflection hemispheres for all possible measurement conditions:
   - Full spherical detection capability at all angles of incidence with minimum obscuration of the incident beam.

5. Instrument size
   Size does not matter - at least for laboratory instruments for light scattering measurements. However, to be able to perform measurements close to fabrication processes, a compact table top system size is mandatory. To enable a transport of the scatterometer by two persons, weight and size should yield:

[1] For more precise measurements with $\Delta\theta_s$=±0.1° of e.g. high quality gratings, a spectral linewidth of $\Delta\lambda/\lambda$≈600 ppm is required.

- System size smaller than (1x1x1) m^3.
- Transport weight lower than 80 kg.

3.2 Concept analysis

In the following, different concepts, including state of the art approaches, are discussed with respect to their suitability to meet the target parameters defined in the previous chapter:

1. Sensitivity

   Typically, either PMTs or silicon photo diodes are used for ARS measurements in the VIS spectrum to achieve the required NEARS values[2] [109]. PMTs [27, 57, 61, 111] allow a lower NEARS in the VIS spectrum [110] whereas photo diodes [12] are chosen for a maximum dynamic range of the bare detector. The signal-to-noise ratio (SNR) is generally improved by lock-in amplifier based metrology [30] to effectively decrease the noise bandwidth. Therefore, the light source is modulated typically in the lower kHz regime by a mechanical chopper [13,27,30,111] or other external optical modulators [63]. The instrument sensitivity grows only linear with the detector solid angle and the incident power (until limited by Rayleigh scattering). Sensitivity scaling by source power and detector aperture size is accordingly only possible within limited ranges. Highly sensitive systems, where the NEARS is lower than the Rayleigh scattering at the air molecules are possible by proper metrology [19,27]. Rayleigh limit improvements are restricted to a (practically limited) reduction of the detector FOV [112, 113] (see chapter 3.6.1), or to exchanges of the surrounding medium. As Rayleigh scattering grows with λ^{-4}, vacuum or flood gas chamber instruments become especially cruical in sub VIS scatterometry [45,51,52]. However, they are not reported for VIS illumination wavelength, where the Rayleigh limit does typically not impose any relevant boundaries for the characterization of even extreme low scattering samples.

2. Dynamic range

   The dynamic range of bare PMTs and photo diodes are typically limited to some few orders of magnitude. Increasing the dynamic range of the instrument over the detector limit can be done in two ways: either the incident power on the detector or the detection sensitivity have to be made scalable in a calibration maintaining way.

   The incident power on the detector can be scaled by changing the optical power at an arbitrary position of the optical path, or by enabling a variable solid angle size (adjustable detector aperture size [12,57,114] or adjustable aperture distance [18]). Rather than scaling the actual source power (up to now limited to some few OOMs), power scaling is typically enabled by a variable attenuation system in the illumination beam path [27, 52, 61, 115, 116].

   The detection sensitivity can be adjusted by scaling amplification gain levels [12], integration time [12], the PMT's acceleration voltage [20,45,50], or by simply using different detector types for different scatter levels [50, 57]. However, the maximum ratings of the detector(s) have to be considered.

[2] Detector sensitivity is generally characterized by the detectivity D (or D*) which is simply the reciprocal of the noise equivalent power. D* is moreover normalized to the detection area [109, 110].

3. Spectral purity

   A high spectral purity can be achieved by simply using laser sources. However, additional methods to increase spectral purity become especially crucial at shorter wavelengths [50] or when broad band sources are being used. Spectral purity can be enhanced by implementing either a spectral selective illumination or detection system. This generally represents a tradeoff between illumination power and spectral purity. The simplest way to increase spectral purity is either source side [50, 116] or detector side optical filtering. Making these filtering processes tunable additionally enables spectral resolved ARS measurements or Raman scatterometry. Spectrally scanning illumination is practicable by monochromator concepts [56, 64, 67, 117, 118] or by using (typically large and expensive) tunable laser sources [68, 119]. Spectrally resolving detection can be implemented by means of either a monochromator (scanning process) [65] or a polychromator [29, 59, 60, 120] (multiplexing process) in the receiver. Monochromators are typically based on grating components, but were also realized for scatterometers by a Fourier-transform spectrometer concept [25]. However, as the illumination power of the source is distributed over a broad spectrum, these concepts typically lack sensitivity. Reported maximum VIS sensitivities of concepts with spectral scanning capability are yet limited to NEARS=10^{-06} sr^{-1} [64]; current multiplexing concepts are even more limited in sensitivity.

4. Beam quality

   Almost all reported instruments for light scattering measurement include a spatial filter and diverse apertures to ensure a clean core beam. Near angle scattering can be minimized by using as few as possible high quality optics after the pinhole. Especially mirror optics are seen advantageous versus a lens optic design because of the fewer surface, less aberrations and the absence of ghosting effects [3]. To reduce diffraction effects, Gaussian-apodized apertures are sometimes implemented in the illumination system [52, 121].

5. Measurement regime

   There are several axes layouts possible to provide full spherical detection capability. Stover describes two OOP instrument configurations [3, pp. 140] (see Fig. 3.1) where

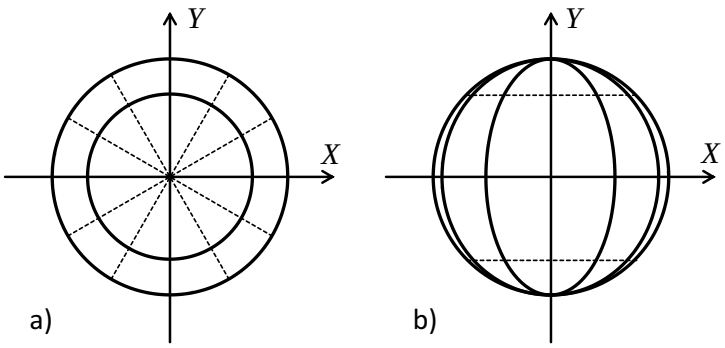

Figure 3.1: Hemispherical natural receiver paths (when only one positioner is moving) projected onto the sample plane XY for two different axes layouts [3]. Analogously to a globe, the receiver naturally scans either parallel to the equator or between the two poles.

the sample and the illumination beam can stay in a fixed position to ensure invariant illumination conditions during the detector scan period. Often, layout a) is chosen [20, 25, 27, 28, 60] in favor of layout b) [18, 69, 111, 115], as it allows the receiver to move naturally along scattering geometry consistent paths with constant θ_s or ϕ_s [3, pp. 139]. This is especially beneficial because the analyzer can stay in a fixed position during s- or p-polarization measurements; whereas layout b) requires an automated analyzer positioner as well as receiver movements where two positioners have to move to follow paths with constant θ_s or ϕ_s.

Layout b) is typically chosen for "practical reasons" [3, pp. 139]. Illumination systems are mostly rather complex and therefore aligned horizontally on optical tables, so that the samples are mounted in an upright position. Hence, gravity induces only for layout b) mechanical stress that is parallel to the polar (symmetry) axis. This is especially crucial for large scatterometers, where mechanical stress related receiver positioning errors gain importance. To achieve gravity stress along the polar axis direction of layout a), the sample has to be mounted horizontally (as realized e.g. in [25, 60]). This however affects that the illumination system has to be uncomfortably configured in a vertically orientation.

Both layouts affect the concepts to enable θ_i adjustments. Sample tilting represents the conventional approach for θ_i adjustments within IP ARS measurement systems [6–8,11–13]. Alternatively, θ_i adjustments can be realized by rotating the incident beam around the sample which is usually the mechanically more complex approach. Therefore, the whole illumination system is rotated on rather big optical benches [25] (at the expense of instrument size and design). Alternatively, a fixed illumination system is connected with fiber optics to a more compact moveable illumination head [60] (at the expense of instrument signature because of the nearby illumination optics). The angle of incidence for layout b) can be easily adjusted by rotating the sample stage around Y [18,111,115], as it only results in an offset in the coordinate system. This is especially beneficial for large laboratory system as it allows the big illumination systems to stay in fixed position on an optical table. However, for layout a) this would mean tilting the sample normal out of the ϕ_s axis which affects polarization as well as scattering geometries. Hence, sometimes an additional rotation stage is used [114,122] to readjust the ϕ_s axis orientation into the sample normal. Otherwise, at least an automatically adjustable analyzer is required.

It is also possible to provide full spherical capability with axes layouts, where the degrees of freedom are not restricted to the receiver positioning system. The degrees of freedom can be moreover distributed over receiver, sample, or illumination rotations. These layouts all require additional polarizer and / or analyzer movements to keep the polarization states constant. A possible axes configuration comprises a fixed illumination system, combined with an IP moveable detector (or vice versa), and a sample positioner with three rotational axes [57, 65, 118]. Another introduced layout provides full spherical capability with a one axis moveable illumination, a one axis OOP movable detector, as well as two rotatable sample axes [61].

However, especially light scattering measurements strongly depend on constant illumi-

nation conditions. System and sample misalignment generates slightly different illumination conditions during measurements if sample and/or illumination movements are used to provide 3D capability. This can cause significant deviations in the ARS if the sample is not perfectly homogeneous. Moreover, the reflected beam sweeps through the lab, which is on the one hand a potential safety problem [3] and on the other hand can cause stray light problems of arbitrary degree. The latter is especially critical for compact or housed instruments. Consequently, these axes layouts would require a moving beam dump if highly sensitive light scattering measurements are pursued. Axes layouts with distributed degrees of freedom over sample and detection movements are typically found in instruments for source characterization measurements as suggested in the corresponding DIN 5032 "Photometry Part 1: Methods of measurement" [123]. However, beam dumping or laser-safety issues are rather irrelevant here. If source characterization is an issue, modularity reasons between instruments for light scattering and illumination measurement would anticipate to use DIN5032-1 compatible goniometer designs, rather than those proposed by Stover.

6. Instrument size

   The vast majority of reported light scatterometers are laboratory systems, where typically the illumination system is separated from the detection system. This increases the effective instrument size and mostly requires an isolated operation on optical tables in rooms that are separated from the fabrication process (to avoid contamination of the scatterometer with dust and light as well as for laser-safety reasons). However, there are some few instruments reported where the illumination system and the detection system are merged into a single but rather large system [25, 61, 66, 69]. Only one instrument is published that is completely enclosed [60]. All of these instruments are limited in sensitivity, dynamic range, or even spectral purity (see chapter 2.1.3).

Recapitulatory, there is no table top system reported that meets all specifications.

3.3 System design

Based on the concept analysis of the previous chapter, the individual concepts pursued in this work are discussed and described in the following.

3.3.1 Axes arrangement

To achieve stable illumination conditions during 3D measurements, it is mandatory to keep the sample as well as the incident beam in an unchanged configuration. Moreover, stray light effects have a greater impact in a compact and housed instrument rather than in laboratory environment. Hence, a sweeping reflected beam during 3D measurements is not tolerable. This restricts the possible axes layouts to those proposed by Stover (see Fig. 3.1).

Both layout a) and layout b) can be designed to a compact setup. The main advantage of layout a) comprises the polarization and scattering geometry consistent receiver paths, which abandons the necessity of additional polarization positioners. However, it requires a moving illumination system for θ_i adjustments. The mechanical stability advantage of layout b) is rather negligible for table top size instruments. In fact, the main advantage of layout b) consists of a possible rotating sample stage to adjust θ_i, which is mechanically less complex than the moving illumination system of layout a).
Consequently, layout a) will be pursued to avoid unnecessary motorized stages.

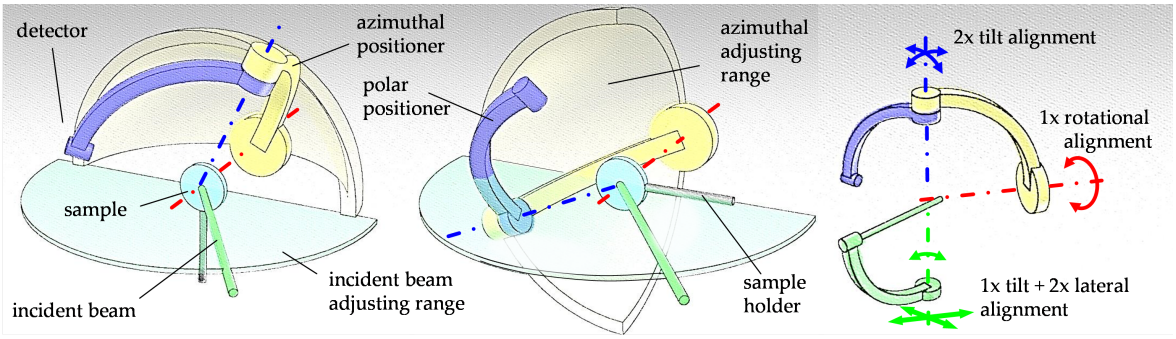

Figure 3.2: The final axes layout (left). Axes layout with minimized obscuration for positive angles of incidence (center). Required degrees of freedom to align the axes arrangement (right).

To integrate source and beam preparation optics without increasing the instrument size, either fiber optics or beam folding mirrors can be used. The latter approach was pursued to obtain more space for the beam preparation system and larger optical distances (less optical surfaces needed to correct aberrations which also means less scattered light). The sample will be in an upright position which is mechanically easier to implement. Furthermore, it allows a more compact overall design because the illumination platform can be arranged in a horizontal orientation and hidden in the basement of the instrument. Rotation stages are applied rather than gear drives in favor of a more compact and layout with less weight. The final axes layout is shown in Fig. 3.2 on the left. The layout in Fig. 3.2 (center) shows less obscuration for large and only positive angles of incidence, but comprises a larger layout. However, changing the system from layout a) to b) can be done with a tolerable effort. Vignetting of the incident beam by the detector arm can be completely avoided with an additional sample rotation stage, which can be integrated with low effort.

As misalignment of all axes contributes to the error budget (see chapter 3.6.3) a complete alignable axes arrangement is beneficial. An ideal alignment of the axes would include a perpendicular θ_s and ϕ_s axis, as well as a collinear θ_i and θ_s axis for $\phi_s = 0$. For a cost effective design, a minimum number of alignment degrees is achieved with the adjustment layout shown in Fig. 3.2 (right) which allows full alignability. Adjustable counter-weights are used to minimize asymmetrical mechanical stress.

The axis layout presented in this subchapter shows full 3D capability with low obscuration and a low degree of complexity. It enables a very compact design and alignment of the axes arrangement within all necessary degrees of freedom.

3.3.2 Illumination system

The illumination system can be designed with either lens or mirror optical elements. Instruments for light scattering measurements typically include a spatial filter (see Fig.2.3) that eliminates stray and scattered light of the optical components in the beam preparation system. The optics following the spatial filter are consequently of specific concern. Using a mirror as the last focusing element typically achieves a better near angle signature because of the absence of optical ghosting [3]. It is especially interesting when multiple sources are implemented because chromatic aberration can be avoided. However, lens optics pose the possibility of a compact and linear optical design. Moreover, the beam focus adjustment can be realized more easily. Hence, lens optics are overall especially attractive for single wavelength illumination systems. The optical components in front of the spatial filter can be realized with either mirror or lens elements as long as aberrations are kept at to an acceptable level. For the table top instrument, both a lens and a mirror illumination system version were realized.

Preliminary considerations

In this section, the influence of instrument size on the near angle limit is discussed. The critical parameters of the optical design regarding an optimized performance are identified.

Following Gaussian optics starting from the last focussing mirror, Cady showed that the theoretically smallest scattering angle θ_{spec} that is separable from the specular beam with a scatterometer can be caluclated by: [124]:

$$\theta_{spec} = \frac{2}{\pi}\frac{\lambda}{d_{ill}} \ . \tag{3.1}$$

It is constant for a given λ and a given sample illumination spot diameter d_{ill} ([3]). Please note that the numerical aperture has no effect on θ_{spec}. The theoretical limit for d_{ill}=3 mm and λ=532 nm is consequently θ_{spec}=0.007°. Eventually, diffraction effects by the truncated

[3] Interesting but off-topic: Solving Eq. (3.1) by the grating equation yields the smallest by light scattering techniques accessible spatial frequency $f_{min,spec} \approx 1/d_{ill}$. It is not a function of the illumination wavelength! For a typical spot size of d_{ill} =3 mm, $f_{min,spec}$ is $3 \cdot 10^{-4}$ 1/µm. However, at least 3 sampled spatial waves by the illumination spot are considered as being required for reliable PSD calculations [125] that in turn correspond to a minimum scattering angle of θ_{spec}=0.02°. A simple but effective trick to artificially increase the illumination spot diameter and thus to improve the specular near angle limit is to measure at grazing incidence [125].

Gaussian beam at the system apertures as well as 3rd order optical aberrations and surface irregularities typically broaden the beam. Measurements down to scattering angles of about 0.01° have been reported [124]. However, measurements in this very near specular region are considered as being not generally reliable due to the low sampling rate [125]. Eq. (3.1) is especially interesting, as instrument size parameters are not a limiting factor. Certainly, Cadys assumption is only valid for diffraction limited designs, which are more easily achievable for laboratory size instruments. It is shown in the following that even the optics in front of to the spatial filter can affect θ_{spec}.

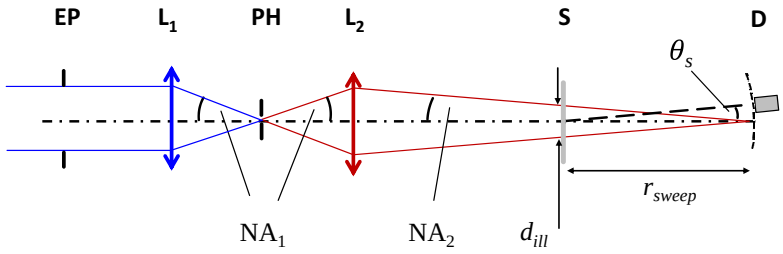

Figure 3.3: Schematic optic design of a scatterometer.

A schematic optic design for the illumination system is shown in Fig. 3.3. The laser beam is expanded and collimated onto the adjustable aperture EP that defines the illumination spot size d_{ill} on the sample S. A spatial filter is realized by means of L_1 which focusses the beam on pinhole PH with the numerical aperture NA_1. The last optical element L_2 images the pinhole onto the detector D aperture plane with NA_2 and the magnification β'_{L2}. The receiver-sample distance is denoted by r_{sweep}. It can be shown that Eq. (3.1) can also be derived for the whole optical system when starting from L_1 with Gaussian optics. Hence, any aberrations in this optical chain, including aberrations in front of to the spatial filter[4], increase θ_{spec}.

For single wavelength (on-axis) illumination systems, spherical aberration is usually the predominant aberration and is scaled by NA [126]. Optical systems with mirror optics additionally inhibit astigmatism, which grows with the field angle to the power of 2 [126].
To reduce astigmatism, simply the mirror tilt needs to be minimized as much as possible. A reduction of the aberrations by decreasing the NAs in the optical path is, however, limited by the instrument geometries, because the illumination spot size on the sample is not scalable. For a fixed illumination spot size, NA_2 can only be decreased by increasing r_{sweep}. Hence, aberrations in L_2 can be reduced by either (1) increasing the instrument size, or by (2) using a periscope mirror in front of the detector. Aberrations in both L_1 and L_2 can be reduced by minimizing NA_1, making it a key parameter to improve θ_{spec}. This can be achieved by increasing the distance $\overline{L_1 L_2}$. As space is limited, beam folding mirrors in front of to the spatial filter can be used without contributing additional light scattering to the near angle-signature. NA_1 could be minimized by moving L_2 as close to the sample as possible. However, it is more reasonable to increase the distance $\overline{L_2 D}$ as much as possible as this can significantly improve near angle scattering effects (see chapter 3.6.1).

[4] If the spot size at the pinhole is not diffraction limited, optimization of the aberrations in front of the spatial filter still allows an improvement of the near angle limit.

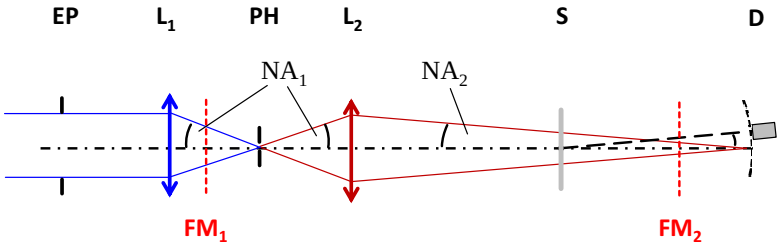

Figure 3.4: Proposed positions for two folding mirrors FM_1 and FM_2 to decrease NA_1 and NA_2 with only low contribution to near angle scattering.

Regarding the optical specifications, the optics in front of to the PH should introduce as less wavefront error as possible to yield a diffraction limited pinhole size, while their light scattering level is not critical. Wavefront errors can be introduced by aberrations as well as higher order surface irregularities. The optics after the PH should, however, achieve low light scattering without introducing aberrations.

To sum up, two beam folding mirrors (FM_1 and FM_2) are beneficially introduced in the optical design to decrease aberrations and improve the specular near angle limit (see Fig. 3.4). Both beam folding mirrors are at positions where the contribution to near angle scattering is low. Two further folding mirrors are placed between L_2 and S to reduce the instrument size, as mentioned in chapter 3.3.1.

Lens system

The lens illumination system was designed using the commercial sequential ray tracing software ZEMAX [127]. The complete optic layout is shown in Fig. 3.5. It was optimized separately for the beam preparation (blue) and the pinhole imaging (red) system by minimizing the rms spot sizes at the pinhole and at the detector aperture plane, respectively. The 532 nm Nd:YAG laser beam is expanded by two plano-concave lenses (1) onto an adjustable aperture (2) that defines the system's NA and therefore the illumination spot size at the sample. The truncated beam is subsequently focused on the pinhole (4) by means of two achromatic lens pairs (3) for a minimum of spherical aberration. The last lens (5) images the pinhole on the detector aperture plane. The whole system is designed for adjustable illumination spot diameters on the sample from 1 mm up to 5 mm when the focus is located at the detector aperture. If the beam is collimated by lens (5), illumination spot diameters of up to 18 mm are possible.

In favor of a smaller construction volume and weight, NA_1 was not additionally reduced by inserting folding mirrors as suggested in the previous chapter. Consequently, ten spherical surfaces were needed to achieve the almost diffraction limited spot diagram for the beam preparation system at the PH (blue layout in Fig. 3.5, geometrical spot diameter $\approx$10 µm) . Practically, the pinhole size is chosen to a diameter of about 2-3 times the size of the beam focus [46], which would yield a pinhole diameter of about 25 µm.

Spot diagrams for the focussing system (red layout in Fig. 3.5) on the detector aperture plane were calculated for a spherical plano-convex lens (PCX), an achromat, and a specially designed plano-aspherical lens. In fact, only the spot diagram of the achromat is shown in Fig.

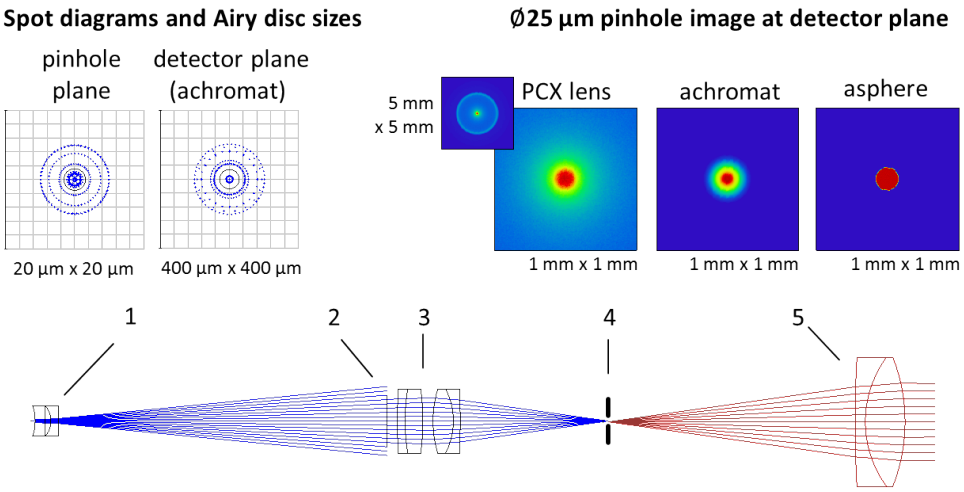

Figure 3.5: Optic design of the lens illumination system with the beam preparation (blue) and the focussing system (red). The last lens (5) is designed axially movable to allow focus variations without changing the beam alignment. Upper left: spot diagrams at the pinhole and the image (detector) location, the circles correspond to the Airy disk size. Upper right: simulated geometric spot sizes calculated for a Ø25 µm object.

3.5. At the expense of the high NA_1 the spot diagram for a single spherical plano-convex lens shows too strong aberrations. This results in the need of an achromat or a plano-aspherical lens to correct for the spherical aberration. The resulting beam focus sizes for the focussing system at the detector plane is shown in Fig. 3.6 in the upper right. They were simulated by geometrically imaging the pinhole at the detector plane. Scatter and diffraction effects are neglected here to evaluate the optic design. A corresponding analysis is performed in chapter 3.6.1.

The plano-spherical lens yields an intolerable geometrical focus size of about 3 mm in diameter (see Fig. 3.5, inset diagram 5 mm x 5 mm) at the detector aperture for a sample illumination spot size of 3 mm. Both the achromat and the asphere yield equal focus sizes of about 0.4 mm in diameter under the same conditions. As the optical light scattering performance of the two elements is not clear, especially with respect to the achieveable polish and cement quality, both solutions were pursued.

Lens (5) is anti-reflective coated for the illumination wavelength of 532 nm. The coating reduces ghosting issues, but even more important, it also reduces the amount of light that is back reflected onto the pinhole plane and subsequently reimaged by the lens (5) onto the detector aperture plane [3]. After the last lens the beam is guided by two folding mirrors onto the sample. The folding mirrors were realized by superpolished Si-Wafers for a minimum of surface scattering. Both wafers are aluminum coated to reduce polarizing effects and increase the reflectance. Polarization optics ($\lambda/4$-plate and polarizer), as well as the attenuation system (chapter 3.3.2) were integrated previously to the spatial filter. A miniature chopper is capable of modulating the cw beam up to 4 kHz for lock-in based signal processing.

Mirror system

The optic design of the mirror system was also calculated with ZEMAX. The layout was again optimized separately for the beam preparation and the focussing system with respect

to the rms spot size at the pinhole and the detector aperture plane, respectively. This more complex and less compact layout was realized to achieve a better near angle signature, and to allow the easy integration of additional laser sources for working at other wavelengths.

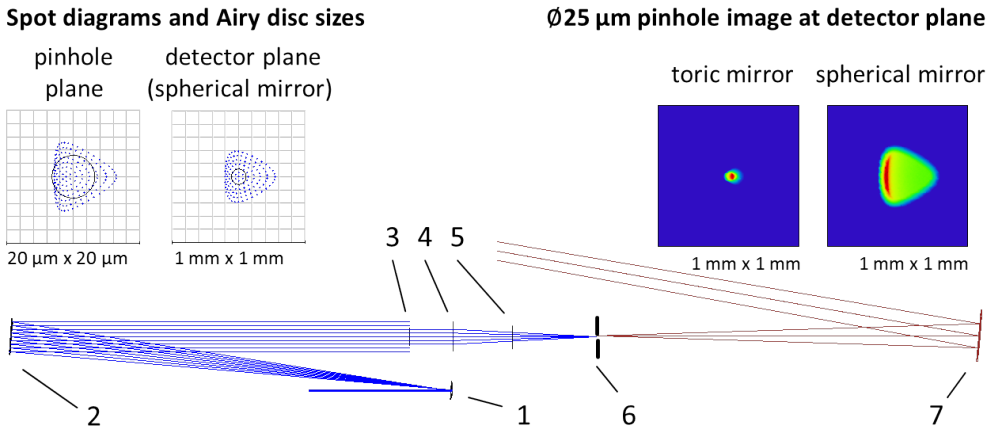

Figure 3.6: Optic design of the mirror illumination system with the beam preparation (blue) and the focussing system (red). The mirrors (3,4) and the pinhole are designed axially movable to allow focus variations without changing the beam alignment. Upper left: spot diagrams at the pinhole and the image (detector) location, the circles correspond to the Airy disk size. Upper right: simulated geometric spot sizes calculated for a Ø25 µm object.

The laser beam is expanded by two spherical mirrors (1, 2) onto an adjustable aperture (3) that defines the illumination spot size on the sample. A spatial filter is realized by means of a parabolic mirror (4, folded illustration) which focusses the beam on pinhole (6). The last mirror (7) images the pinhole onto the detector aperture plane. For a minimized NA_1, the distance between mirror (4) to (7) is maximized by means of an additional folding mirror (5) in front of the pinhole as anticipated in the "preliminary considerations" of this chapter. This design moreover allows to move the beam focus without changing the beam alignment, which is particularly beneficial to compensate for sample curvatures. The whole system is capable to adjust the illumination spot diameter on the sample from 1 to 3 mm if the beam is focussed onto the detector aperture plane. If the beam is collimated by mirror (7), illumination spot diameters of up to 15 mm are possible.

The geometrically simulated spot size in the detector plane by the imaged pinhole with 25 µm diameter is shown in Fig. 3.6 in the upper right. Its diameter was found to yield about 300 µm for a spherical mirror (7), and 50 µm for an aspherical toric mirror. Certainly, diffraction effects have to be considered as the Airy disk size has a diameter of 100 µm. The beam focus exhibits residual astigmatism, though the (half-angle) mirror tilt could be minimized down to 5° (mechanically limited). Obviously, mainly the aberrations of mirror (7) limit the specular performance of this optic design. However, only the spherical mirror layout is pursued, as the improvement of the beam profile by an aspherical surface is traded for an expected increase of surface scattering.

Attenuation system

To expand the dynamic range of the instrument over the dynamic range of the detector element, additional attenuators are essential to spread the dynamic range over several orders of magnitude (see chapter 3.2).

They were placed inside the illumination system for a more compact detection layout. Three magnetic coils are implemented instead of the state-of-the art filter wheels. Each of them moves an optical density filter into or out of the laser beam, where the optical density of the filters is combined to achieve an attenuation dynamic range of 7.5 OOM. For the different attenuation levels the first attenuator is always placed in the beam. This comprise three major advantages compared to filter wheels:

- The filters' off/on positions are highly repeatable as they include mechanically defined stops.
- Only the first filter reflects a secondary beam to the laser head which is constant in intensity and adjustable in position over the different attenuation levels. The reflected beams of the later filters are attenuated by the first filter down to a negligible level. This ensures a stable laser performance.
- Laser safety can be enhanced if the magnetic coils are designed to drop back in the attenuation position in case of electronic failures.

3.3.3 Detection system

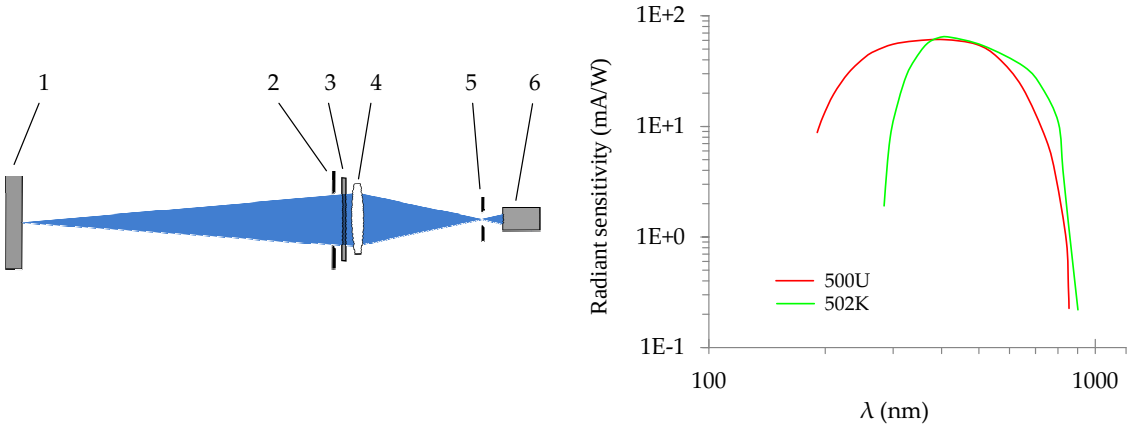

Figure 3.7: Schematic diagram of the detection system (left): 1, sample; 2, solid angle aperture; 3, insertable polarizer; 4, field lens; 5, field stop; and 6, PMT; Sensitivity as a function of wavelength for different Hamamatsu head-on PMTs (right) [128]. The red solid line marks the sensitivity of the used PMT R1463 [129].

The detection of light scattered by the sample (1, Fig. 3.7 left) is based on a PMT (6) in favor of the more dynamic but less sensitive photo diode (see chapter 3.2). The spectral response of different Hamamastsu head-on PMTs is shown in Fig. 3.7 [129]. It is mainly a function of the used photocathode and window material. The often more sensitive side-on PMTs are not considered because of their disadvantageous mechanical layout. As the favored spectral sensitivity curve 502K (solid green line) is not available for compact detector

heads, a PMT with the spectral sensitivity curve 500U (solid red line) is used. The head-on PMT Hamamatsu R1463 [129] is finally chosen, applicable for highly sensitive light scattering measurements from 185 nm to 850 nm (see Fig. 3.7 right) with low dark current rates. The detector layout design (see Fig. 3.7 left) corresponds to the layout #1 proposed in the ASTM E2387-05 norm [30]. Signal processing is based on a computer controlled lock-in amplifier Ametek 7230 DSP.

According to the scan resolution, sensitivity, and required reduction of speckle influence on the measurement, the solid angle aperture (2) can be changed from diameters of 0.2 mm up to 8.8 mm. This corresponds to full angles of 0.05° to 2°, or solid angles of $5 \cdot 10^{-7}$ to 10^{-3}, respectively. For additional separation of s - or p-polarized light, a linear polarizer (3) can be inserted. The field of view (FOV) can be adjusted by a field lens (4) / field stop (5) combination from 7 mm up to 20 mm in diameter in the sample plane. As the instrument far angle signature is a function of the the FOV (see chapter 3.3.1), a minimized FOV is often preferable. However, the FOV must not vignette the illumination spot on the sample. Especially when measuring with large angles of incidence, the FOV must be carefully adapted to the illumination spot size that grows with $\cos^{-1}\theta_i$ (e.g. an illumination spot of 3 mm at normal incidence is broadened at θ_i=80° to 17 mm). Therefore, the field aperture size is realized to be adjustable.

3.3.4 Summary

In chapter 3.3.1, a layout of the axes arrangement based on a design proposed by Stover [3] was chosen to enable full 3D-spherical detection capability with constant illumination conditions and low obscurations. In chapter 3.3.2, the critical parameters of the optical design were analyzed with respect to optimal system performance under restricted space conditions. Based on this analysis, the original layout was adapted by means of additional folding mirrors in the detection and illumination system. This results in:

- A decrease of the NAs in the optical path. Less optics are accordingly required to compensate aberrations (which reduces the number of light scattering surfaces).
- A minimization of the obscuration of the incident beam for $\theta_s \approx \theta_i$ and ϕ_s=0
- An increase of the effective receiver arm length (which improves the near angle signature).

This concept enables a better performance without increasing instrument size. Two further folding mirrors are introduced in the illumination system to reduce the instrument size. The detection system described in chapter 3.3.3 was designed according to ASTM E2387-05 and is based on a PMT. It enables highly sensitive detection within the whole VIS spectrum including parts of the NIR and UV spectrum without changing the detector. The detection dynamic range is increased by optical filters in the illumination system mounted on highly repetitive actuators.

3.4 Realization

3.4.1 Completed System

A photograph of the realized table top system is shown in Fig. 3.8. The background shows the instrument with mounted housing (1) which reduce external influences like contamination or stray light to a minimum. A compact size of 0.8x0.8x0.8 m^3 was achieved, which enables the operation on ordinary tables. The systems overall weight is 100 kg and 110 kg, for the lens and the mirror illumination system, respectively. If the top system cover is removed, the system weighs 70 kg (or 80 kg), which allows the transportation of the instrument by two persons. All relevant parts are anodized or blackened to minimize residual interior stray light. The small encapsulated instrument enables a flexible close-to-process operation, however, a clean lab environment is recommended to characterize sensitive samples.

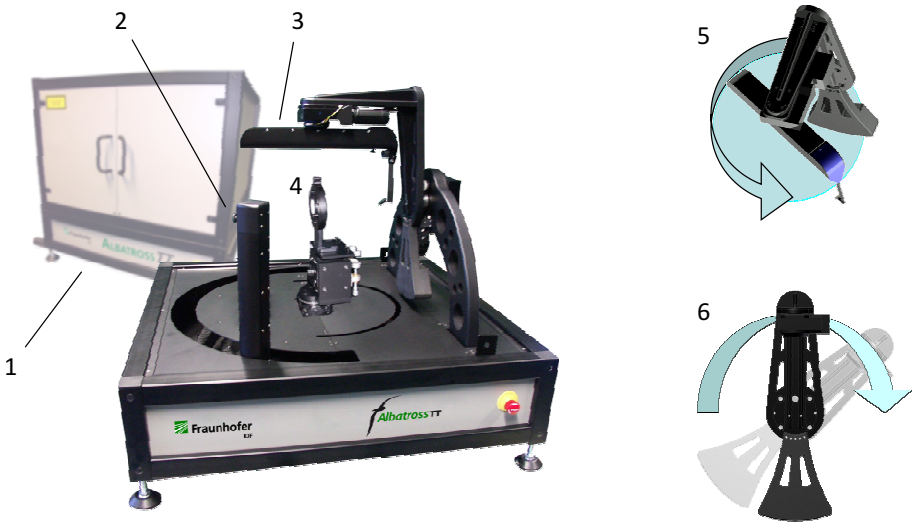

Figure 3.8: Photograph showing the complete table top system (left) with the detector positioning system (right). The instrument with mounted top cover is visible in the background (upper left).

Positioners and lock in amplifier are computer controlled by a comprehensive software enabling data analysis and automated measurements [130]. The variation of the angle of incidence θ_i of the laser beam is implemented by a movable illumination system (2). It is hidden in the lower part of the instrument and illuminates the sample by means of two folding mirrors. Light scattered from the sample (4) is recorded by the detection system (3) mounted on a 3D-positioning system that provides a scatter geometry consistent variation of the polar scattering angle θ_s (5) and the azimuthal scattering angle ϕ_s (6). All positioners are counterweighted to minimize asymmetrical mechanical stress for accurate positioning. The sample stage allows for free sample adjustment within all degrees of freedom. A second version with additionally motorized X and Y positioners was also realized to enable raster scans [131]. An elemental and light weight lens illumination system was designed. Additionally a more comprehensive mirror system, that is set up on a spacious optical bench was designed. The optical bench enables a more variable beam preparation system where modifications like the integrations of additional light sources can be performed comparably flexible as in laboratory systems.

3.4.2 Measurement procedure

Typical measurement and calibration procedures for ARS instruments are detailed in the ASTM [30]. In the following, the measurement procedure of the scatterometer is described. It is based on the relative normalization (see chapter 2.1.2).

From Eq. (2.7) follows the calculation of the ARS by the software:

$$\mathrm{ARS}(\theta_s) = \frac{\Delta P_s(\theta_s)/\Delta\Omega_s}{P_i} = \frac{V_{det}(\theta_s)/k_{cal,j}}{V_i \cdot k_{att,i(V_{det})}} \ , \tag{3.2}$$

where $V_{det}(\theta_s)$ is the detector voltage signal, V_i is the total power constant corresponding to the detector signal measured within the specular beam, and $k_{cal,j}$ corresponds to the solid angle of the different apertures j. The additional constant $k_{att,i(V_{det})}$ is used to compensate for the transmission of the attenuator levels $i(V_{det})$. Please note that the attenuator level $i(V_{det})$={1;2;...} is a function of signal voltage to optimize signal noise and to extend the effective dynamic range. Sometimes, also $k_{cal,j}$ can be a function of the scattering angle to increase optical resolution near the specular beam (small aperture) or to yield a higher signal-to-noise ratio at large scattering angles (big aperture).

The calibration constants V_i, $k_{att,i(V_{det})}$, and $k_{cal,j}$ have to be determined before a measurement can be performed. The constant V_i has no influence on the calibration if a relative calibration is performed [30]. However, it is usually performed along with the relative normalization method as it allows the calculation of e.g. reflection coefficients or diffraction efficiencies. The constants $k_{att,i(V_{det})}$ and $k_{cal,j}$ are usually determined every time the optics in the illumination system are changed. If the measurements are performed over a long period of time, it is often advantageous to refresh V_i and / or $k_{cal,j}$ to compensate drifts.

The attenuator transmission is determined from measurement of a constant ARS value with different filter levels. The relative change in transmission $T_{att,i,i-1}$ between the two adjacent attenuator levels i and $i-1$ is then calculated by averaging N measured signal values:

$$T_{att,i,i-1} = \frac{\frac{1}{N}\sum_{c=1}^{N} V_{det,i,c}}{\frac{1}{N}\sum_{c=1}^{N} V_{det,i-1,c}} \ . \tag{3.3}$$

The absolute transmission of the individual filter levels $k_{att,i(V_{det})}$ is then calculated as:

$$k_{att,i(V_{det})} = \prod_{b=1}^{i} T_{att_{b,b-1}} \ . \tag{3.4}$$

The detector aperture software constant $k_{cal,j}$ is calibrated according to ASTM from a measurement of a sample with known $ARS_{cal}(\theta_s)$ while the detector aperture $j(\theta_s)$ is kept constant. The highly Lambertian scattering sample Spectralon [132] is used because of its uniformity as a function of wavelength, its high durability, and homogeneity. The data and constants of the calibration measurement are denoted by the indices r:

$$k_{cal,j} = \frac{V_{det,r}(\theta_{s,r})}{V_{i,r} \cdot k_{att,i(V_{det,r}),r}} \frac{1}{ARS_{cal}(\theta_s)} \tag{3.5}$$

Inserting Eq.(3.4) and Eq. (3.5) in Eq. (3.2) with $V_i \equiv V_{i,r}$ yields the final equation for the calibrated system:

$$ARS(\theta_s) = \frac{V_{det}(\theta_s)}{V_{det,r}(\theta_{s,r})} \frac{\prod_{b=1}^{i_r(V_{det,r})} T_{att,r_{b,b-1}}}{\prod_{b=1}^{i(V_{det})} T_{att_{b,b-1}}} ARS_{cal}(\theta_s) \ . \tag{3.6}$$

All constants are known. As already mentioned, the previously determined total power constant is canceled out and has no influence on the calibration.

Before the actual measurement is performed, an instrument signature scan is recommended (scan without sample, see chapt. 3.6.1) to allow the separation of sample scatter from instrument scatter. Afterwards, the sample is aligned into the center of the axes arrangement and the measurement scan can be run. E.g., a specular sample is typically aligned by (see other alignment strategies in ref. [30]):

1. Move θ_i and θ_s to 3°, tilt sample until reflected beam enters receiver aperture (mind PMT max. ratings!).
2. Move θ_i and θ_s to large angle (e.g. 60°), adjust the Z position of sample until beam enters receiver aperture.
3. Adjust X / Y measurement position.
4. Repeat from step 1 until satisfied.
5. Move θ_i and θ_s to desired angle of incidence and adjust sample tilt if necessary.

3.5 Parallel measurement channels

Nearly all surfaces, coatings, and materials show different light scattering characteristics at different illumination wavelengths and for different polarization parameters. As optical components are mostly used in a broad spectral range, a comprehensive light scattering characterization at multiple wavelengths is often beneficial. A complete polarization analysis of a sample (Müller Matrix ellipsometry [3, 133]) demands four different polarization parameters on the illumination and detection side, respectively. State-of-the-art instruments to measure scattered light with high sensitivity and dynamic range enable only a sequential characterization with different measurement parameters. Moreover, a significant part of the operating time is needed for a manual refit of the instrument between the parameter changes.

This chapter will introduce a novel concept with parallel measurement channels that allows simultaneous ARS measurements with arbitrary different parameters (wavelength, polarization, coherence). In contrast to state-of-the-art developments of λ multiplexed ARS measurements (see chapter 3.2), this method enables parallel ARS measurements at the same sensitivity and same dynamic range as high-end sequentially performing scatterometers. Furthermore, the concept described in this chapter allows measurements with multiplexed polarization or coherence, which is a new feature for instruments to measure scattered light. Also, the mixing of different parameters in different channels becomes possible, e.g. polarization *and* wavelength can be multiplexed.

After the concept is introduced, the demodulation principle is analytically described. Based on this developed model, the dynamic range between the individual channels is extended by suppression of cross talk to achieve light scatter relevant specifications.

3.5.1 Frequency division multiplexing

Concept description

The concept proposed in this chapter is based on frequency division multiplexing (FDM) that is also used in e.g. telecommunication techniques [134, 135]. Light beams (1, 2, 3 in Fig. 3.9) with different parameters (wavelength, polarization) are marked with different modulations (7, 8, 9) and later on combined by dichroic or polarizing beam splitters (15, 14). The combined beam is guided through the beam preparation optics (see chapter 3.3.2), hits the sample (17), and the scattered light is detected by a color and polarization blind detector (18). Demodulation is performed subsequently by electronic devices (19, 20, 21) that separate the detector signal into the individual channels on the basis of the known modulations. These devices can be realized by bandpass filters or lock-in amplifiers (LIAs), where the latter provide a high sensitivity and dynamic range. Consequently, only lock-in amplifier based demultiplexing is described here.

Standard sequentially operating scatterometers can be easily upgraded by additional electronics and additional optics in the beam preparation system, while the detector system can be left unmodified.

Polarization multiplexing is realized by simply modulating different polarization states separately. This is possible with a second modulation step (see Fig. 3.9 right), allowing e.g.

both wavelength and polarization multiplexing with a single ARS measurement. Therefore, circularly polarized beams of different wavelengths (1, 2, 3) are first modulated (7, 8, 9) and combined. The combined beam is separated by a polarizing beam splitter (25) in s and p polarization, individually modulated (27, 28), and recombined (26). The detected scattered light is then demultiplexed by 6 LIAs (19-24) to yield a total of 6 channels with 3 separately recorded illumination wavelengths that are further divided into s and p polarized illumination, respectively. An additionally performed optical separation of the polarization states at the detector would double the total number of channels to 12 channels with 3 wavelengths, s and p polarized illumination, and s and p polarization sensitive detection.

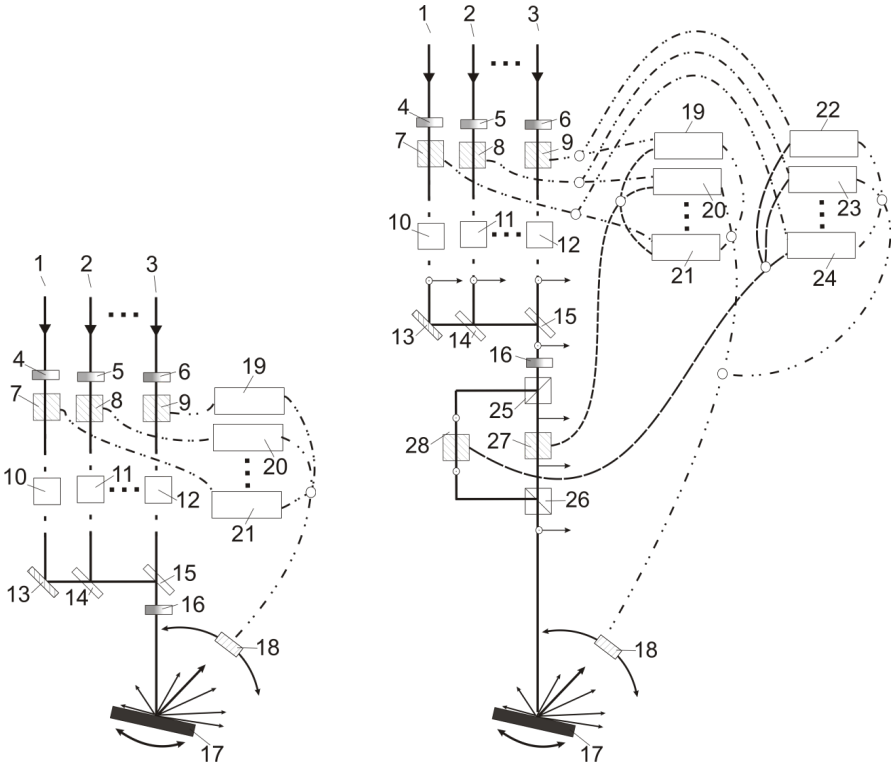

Figure 3.9: Left: sketch of the multiplexing concept. Right: device with both polarization and wavelength multiplexing channels [136].

Working principle

Extraction of modulated signals from random background noise by means of LIAs is a well understood principle. An existing LIA model [137–139] is described in this chapter and adapted to the special case of demodulating two rectangularly modulated signals. In chapter 3.5.2 the model is extended for crosstalk optimizations.

The detected rectangularly modulated signal $U_1(t)$ with amplitude A_1 and modulation frequency ω_1 is superimposed by a rectangularly modulated interfering signal $U_2(t)$ with amplitude A_2 and modulation frequency ω_2. The individual signals can be described by a Fourier series, their sum is the combined signal $U(t)$:

$$U(t) = \frac{4}{\pi} A_1 \sum_{i=1}^{\infty} \frac{1}{2i-1} cos\left((2i-1)\omega_1 t\right) + \frac{4}{\pi} A_2 \sum_{j=1}^{\infty} \frac{1}{2j-1} cos\left((2j-1)\omega_2 t\right) \ . \tag{3.7}$$

Demodulation in the LIA is performed by multiplying $U(t)$ with an internally generated reference signal of the LIA with the same frequency as $U_1(t)$ and a phase shift ϕ [139]. In most state-of-the-art LIAs, the phase is extracted by using two phase shifted reference signals [140]. Hence, the simplified assumption is made that ϕ equals 0. The demodulated signal $X_1(t)$ to measure $U_1(t)$ is then calculated by:

$$\begin{aligned} X_1(t) = \frac{2}{\pi}A_1 + \frac{2}{\pi}A_1 \left(cos(2\omega_1 t) + \sum_{i=2}^{\infty} \frac{cos(2i\omega_1 t) + cos((2i-2)\omega_1 t))}{2i-1} \right) \\ + \frac{2}{\pi}A_2 \sum_{j=1}^{\infty} \frac{cos\left(((2j-1)\omega_2 - \omega_1)t\right) + cos\left(((2j-1)\omega_2 + \omega_1)t\right)}{2j-1} \end{aligned} \quad . \tag{3.8}$$

The time independent summand $2A_1/\pi$ corresponds to the direct current (DC) of the LIA output $V_1(t)$ and is linear to the amplitude of the signal $U_1(t)$. The residual summands with higher frequency terms are ideally completely blocked by a subsequent low pass filter with the transfer function $H(\omega)$ [137]:

$$V_1(t) = \mathcal{F}^{-1}\left\{\mathcal{F}\left\{X_1(t)\right\} \cdot H(\omega)\right\} \approx \frac{2}{\pi}A_1 \ . \tag{3.9}$$

However, non-ideal filters achieve only a limited attenuation. The frequency response $|H(\omega)|$ of an analog first-order low-pass filter with integration time τ is :

$$|H(\omega)| = \frac{1}{\sqrt{1+(\omega\tau)^2}} \ . \tag{3.10}$$

For interfering signals like stochastic noise that is distributed over a broad frequency range, $V_1(t)$ consists apart from the DC output of attenuated stochastic broadband noise. However, for an interfering signal with high amplitude and a discrete frequency, the DC output is superimposed by a pronounced oscillation. As a result, measurement uncertainty increases and the readout of the signal amplitude can be distorted. Consequently, the approximation in Eq. (3.9) is valid to extract a signal buried in stochastic noise rather than to separate it from strong and discrete interfering signals originating from other channels.

3.5.2 Cross-talk suppression concept

For crosstalk of the interfering signal $U_2(t)$ into the output of the LIA of channel 1, the following expression can be approximated from Eq. (3.8) and (3.9) assuming sine-modulation and neglecting phase influence:

$$\frac{V_1}{V_{1,ideal}} = 1 + \frac{V_{2,ideal}}{V_{1,ideal}}|H(|\omega_1 - \omega_2|)| \ , \tag{3.11}$$

where $V_{1,ideal}$ and $V_{2,ideal}$ are the ideal LIA outputs (no crosstalk) of measurement channel 1 and interfering channel 2.

E.g., for identical magnitudes of signal and interfering signal with measurement parameters τ=50 ms, f_1=1 kHz, f_2=0.7 kHz, an acceptable amount of only 1% crosstalk ($V_1/V_2 = 1.01$) between the channels is present. If the signal magnitude difference between two channels increases to 1 OOM, about 10% of crosstalk can be accordingly expected.

Hence, crosstalk is naturally influenced by the dynamic between the individual channels. To reduce crosstalk between the individual measurement channels, a combination of different techniques is proposed. This concepts aims at multiparallel ARS measurements over a dynamic range of at least 8 OOM between the individual channels. This allows parallel ARS measurements of most samples with different illumination wavelengths [5]. To yield the necessary cross-talk surpression, the following techniques are considered:

- Electronic prefiltering
- Optical prefiltering
- Optical adaption
- Optimizing demultiplexing parameters

Electronic prefiltering

Electronic prefiltering is a simple, yet effective method, to decrease crosstalk. As in the experiment the modulation frequencies of all channels are known, bandpass filters can be used to attenuate the signals of other channels. However, an increase in signal noise has to be considered resulting from the additional electronics.

Optical prefiltering

Splitting the individual channels optically on different detectors is technically only reasonable when a multiplexed polarization separating detection is demanded.

Optical adaption

Crosstalk origins not due to the different ARS levels, but because of the difference in the detected signal magnitude V_1 of different channels. Hence, crosstalk can be optically effectively reduced if all channels are individually attenuated in the illumination system. The attenuation is therefore adjusted to yield detector signals of each channel within about the same OOM. This requires additional attenuators at locations in the optical path where the channels are spatially separated. Possible locations are e.g. after the source (4, 5, 6, see Fig. 3.9) or when polarization is multiplexed nearby the modulators (27, 28).

Optimizing demultiplexing parameters

Demultiplexing performance can be optimized by means of Eq. (3.8) and (3.9).

- Eq. (3.8) shows that the higher harmonics of the rectangularly modulated signals affect the LIA's output. Hence, by simply changing the modulation form from rectangular to sinusoidal can effectively reduce crosstalk. Mechanically, sinusoidal modulation can be approximately achieved by chosing a chopper slit width that has about the same diameter as the Gaussian laser beam profile. Technically more interesting are sources that can be modulated by means of an external analog signal (e.g. laser diodes), allowing a sinusoidal modulation without additional mechanical parts.

[5] Gratings are considered as being especially critical, as the scattered light of one channel can get easily superimposed by a diffraction order of another channel.

- Increasing the order of the low-pass filter can effectively reduce crosstalk. Higher order low-pass filters have an increased roll-off slope that reduces leakage (from other measurement channels). However, an increased filter order results in longer settling times and thus increases measurement times. As a consequence, a small filter order is advantageous to achieve faster measurement times.
- Crosstalk can also be reduced by configuring the modulation frequencies of all channels. As attenuation of the low-pass filter increases with ω (see Eq. (3.10)), it is often advantageous to chose modulation frequencies that are separated as far as possible. Though, care has to be taken that higher harmonics of rectangular modulated signals do not superimpose with other channels. Furthermore it has to be considered that growing ω may reduce output power of modulated laser diodes.
- The shape of the filters transfer function can also be used to optimize crosstalk without increasing the filter order. For example, digital low-pass filters introduce zeros in the transfer function (see Fig. 3.10) [141]. If the modulation frequencies are correctly chosen, this allows to completely "hide" other channels. This technique is also used in orthogonal frequency-division multiplexing (OFDM) techniques to extend the transmission capacity in modern telecommunications [142, 143].
  Digital low-pass filters are realized by multiplying a window function $w(t)$ with periodicity 2τ to the demodulated signal in the time domain. This corresponds to a weighted moving average filter and is mathematically equivalent to the convolution of the signal with $w(t)$ [141]. In its simplest form $w(t)$ is a uniformly weighted rect function [141], which is sufficient to describe the main characteristics and advantages of FIR filters:

$$V(t) = X(t) \otimes w(t) = X(t) \otimes \frac{1}{2\tau}\mathrm{rect}\left(\frac{t}{2\tau}\right) \ . \tag{3.12}$$

  In the frequency domain Eq. (3.12) corresponds to the product of the individual Fourier pairs $\mathcal{F}\{V(t)\} = \mathcal{F}\{X(t)\} \cdot \mathcal{F}\{w(t)\}$, where

$$\mathcal{F}\{w(t)\} = H_{\mathrm{rect}}(\omega) = \frac{\sin(\omega\tau)}{\omega\tau} \tag{3.13}$$

  yields the transfer function $H_{\mathrm{rect}}(\omega)$ of the rect filter. Higher low-pass filter orders N are achieved by applying the filter multiple times[6] N:

$$H_{\mathrm{rect},N}(\omega) = \left(\frac{\sin(\omega\tau)}{\omega\tau}\right)^N \ . \tag{3.14}$$

  The zeros in FIR transfer function of Eq. (3.14) can be exploited to yield high attenuation at discrete frequencies even for low filter orders (faster measurement times). Zeros in Eq. (3.14) are calculated by:

$$\omega_0 = M\pi/\tau \ \text{ for } \ M \in \{\pm 1, \pm 2, ...\} \ . \tag{3.15}$$

  With Eq. (3.11) the following condition can be derived to achieve minimized crosstalk

[6] As convolution is associative, these higher filter orders can be easily implemented in time space by a non-uniformly weighted window function. The window function is calculated by the N^{th} convolution power of $w(t)$, such that e.g. a second order filter of a rectangular window function equals a triangular shaped window function.

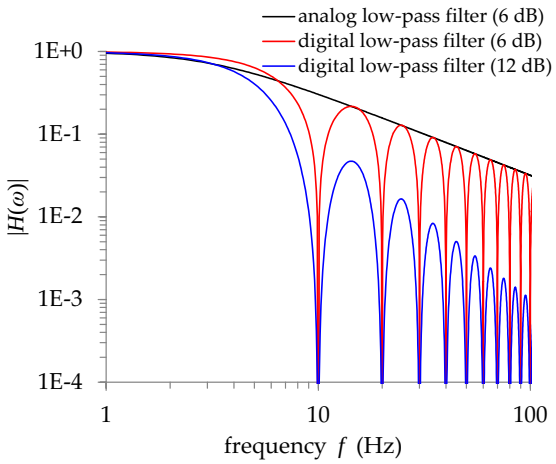

Figure 3.10: Analog and digital low-pass filter.

by adapting ω_1 and ω_2 to τ:

$$\omega_2 = \omega_1 + M\frac{\pi}{\tau} \text{ for } M \in \{\pm 1, \pm 2, ...\} , \tag{3.16}$$

which corresponds to modulation frequencies f_1 and f_2

$$f_2 = f_1 + \frac{M}{2\tau} \text{ for } M \in \{\pm 1, \pm 2, ...\} . \tag{3.17}$$

It is obvious, that adapting the frequencies with Eq. (3.17) is reciprocal. So, adapting f_2 to f_1 and τ minimizes crosstalk from f_2 to f_1, as well as from f_1 to f_2. This also holds for multiple channels. However, laser modulation waveforms are practically not perfectly sine shaped, which leads to higher (even and odd) harmonics that should be avoided, such that f_1 is not an (even or odd) multiple of f_2 or vice versa.

Crosstalk from the individual channels can theoretically be completely blocked by adapting the modulation frequencies. Practically, the limited stability in the modulation frequency increases crosstalk, and moreover, the power of interfering signals increase noise in the LIA and the detector. Experiments showed that an optimization of the demultiplexing parameters yields about two OOM dynamic between two channels for this instrument (see chapter 3.6.2).

Adapting the modulation frequencies alone is consequently not sufficient to yield the aspired 8 OOM dynamic between the channels, which makes optical adaption of the different channels mandatory. Otherwise, using solely optical adaption leads to impractical small attenuation steps sizes to adapt the individual channels. However, combining both techniques enables the required dynamic range for ARS measurements.

3.5.3 Summary

A novel concept has been proposed that enables multiplexed ARS measurements with multiple channels. It allows parallel measurements with different parameters, e.g. different wavelength, polarization, or coherence, where different parameters can also be mixed in different channels. Previously published multiplexed light scattering measurements were limited to wavelength multiplexing only [29] and with a limited sensitivity. Different crosstalk suppression concepts

were developed and combined to successfully meet the demanding specifications of high-end ARS measurements.

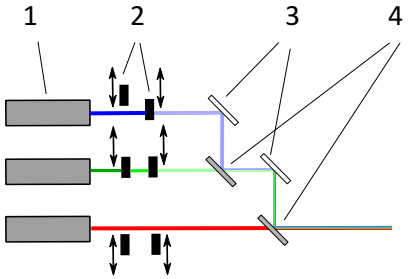

Figure 3.11: Beam combination by alignable dichroic mirrors and turning mirrors with the necessary degrees of freedom.

The mirror illumination platform (see chapter 3.3.2) is used to integrate this new concept into the table top instrument. Along with the existing Nd:YAG laser, two additional laser diodes (1) are implemented and combined by alignable folding mirrors (3) and dichroic mirrors (4) with the necessary degrees of freedom. Now, ARS measurements at λ=405 nm, 532 nm, and 640 nm are possible. Two additional LIAs are added to perform parallel signal readout under optimized demodulation parameters. Also, two automatically moveable ND filters (2) can be used after each laser source to adapt the illumination powers.

3.6 Instrument performance

In this section, the performance of the developed table top system is discussed. This includes instrument signature, the cross-talk performance of the parallel measurement channel concept (introduced in chapter 3.5), and a comprehensive ARS uncertainty analysis. Finally, the results of an optimization that was enabled by the newly obtained information are presented.

3.6.1 Instrument signature

The instrument signature corresponds to the minimum ARS signal (as a function of scattering angle) that can be detected with an instrument for light scattering measurements. It is found by an ARS measurement without a sample [30] and represents, besides measurement uncertainty, the most important performance characteristic of a scatterometer.

When measuring scattered light, the beam profile and stray light inside the instrument limit the minimum ARS signal that can be measured from samples. A low far angle instrument signature is in particular important for the analysis of low scattering samples, while a narrow beam profile grants access to the near angle ARS and can significantly influence the accessible spatial frequency bandwidth (f_r is linear towards θ_s for small scattering angles). Furthermore, light scatter analysis close to the specular beam is crucial for optical components, since it constitutes a major contribution to the point spread function.

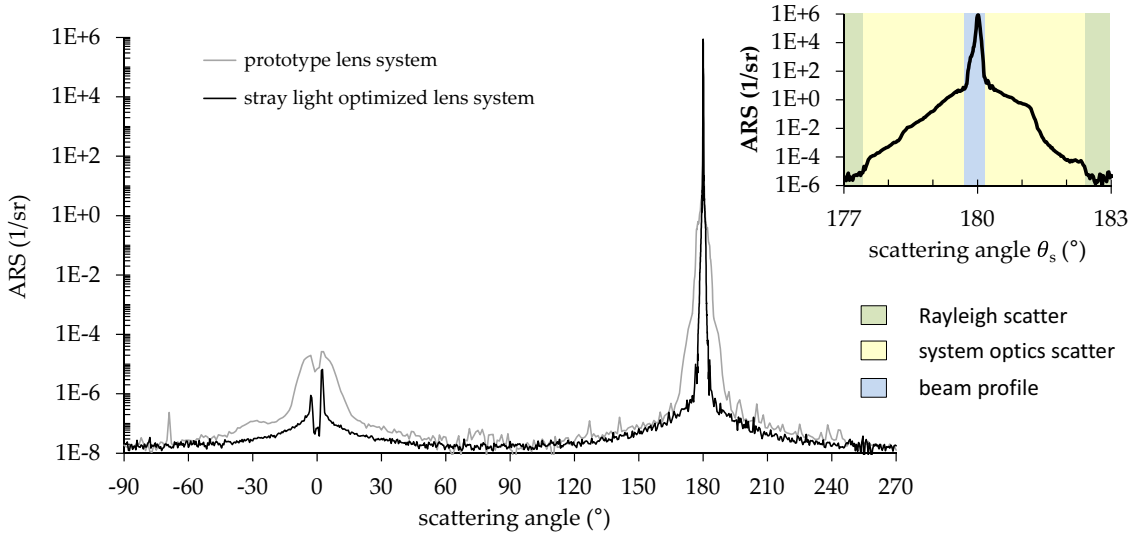

Figure 3.12: Instrument signature of the prototype instrument and a later stray light optimized version (both lens systems). Inset diagram: near angle signature of the optimized system with a color coded subdivision into their individual origins.

Fig. 3.12 shows the instrument signature of the first realized prototype compared to a subsequently optimized system. The transmitted specular beam is located at θ_s=180°, while the increased scatter level at θ_s=0° is a result of residual stray light from the beam dump. Both signatures originate from lens illumination systems and were measured at an illumination wavelength of 532 nm. Mainly stray light concerning optimizations were pursued to lower the instrument signature around the specular beam and the beam dump. Additionally, improvements in the measurement chain allowed to lower the NEARS far below the

Rayleigh background scatter limit for s-pol illumination. An extremely low ARS signature limit (s-pol) of $1 \cdot 10^{-8}$ 1/sr at θ_s=90° and a dynamic range of about 13 orders of magnitude have been achieved, which enables the characterization of even superpolished transparent substrates [144].

The instrument signature is a combined outcome of mostly separable physical effects. These effects can be subdivided according their limiting influence on far and near angle signature:

- Far angle signature limitations
  - Rayleigh scattering at the air molecules
  - Stray light
  - Signal noise (NEARS)
- Near angle signature limitations
  - Beam profile
  - Light scattering from system optics

The far angle scatter level of the high-end instruments is limited by Rayleigh scattering effects in air, if stray light within the system and the NEARS are kept low. Rayleigh limited scatterometers exhibit a typical $\sin^{-1}\theta_s$ shaped signature. The shape origins from the intersection volume of the illumination beam with the detector's field of view that is a function of the scattering angle. The NEARS corresponds to the ARS level that is only affected by signal noise in the measurement chain and is determined by an ARS measurement with the detector closed [30].

The width of the specular beam is affected by the optic design, since the beam is broadened by diffraction effects at the system apertures and aberrations. However, light scattering from the system optics additionally increases the instrument signature up to about 1° to 5° around the specular beam.

The combined instrument signature is simply calculated by the sum of each contribution.

Beam profile

The specular beam profile is limited by diffraction effects, aberrations and surface irregularities from the system optics. As already mentioned in chapter 3.3.2, even the optics preceding the spatial filter have an effect on the width of the specular beam.

To analyze the beam profile of the instrument, the spot size at the detector plane was simulated using the physical optics propagation (POP) tool of ZEMAX [145]. The POP tool propagates a sampled complex wavefront through the whole optical system surface by surface, to calculate the illuminance distribution $E(y)$ at e.g. the detector plane [127]. This allows to simulate the diffraction effects at the system apertures and the spatial filter to calculate the beam profile limited near angle signature including aberrations. The resulting illuminance distribution $E(y)$ is normalized by the output power of the simulated system P_{out} and scaled by the instrument geometries to yield the near angle signature of beam profile:

$$ARS(\theta_s) = \frac{r_{sweep}^2}{P_{out}} \cdot E\left(\frac{y}{r_{sweep}}\right) \quad . \tag{3.18}$$

The simulated beam profile of the optic design described in chapter 3.3.2 is displayed in Fig. 3.13 (blue dotted line). It is compared to the measured near angle signature recorded with an detector aperture of $\Delta\theta_s$=0.05° (full angle). Though the shape is similar, the width of the simulated beam is smaller than the measured one.

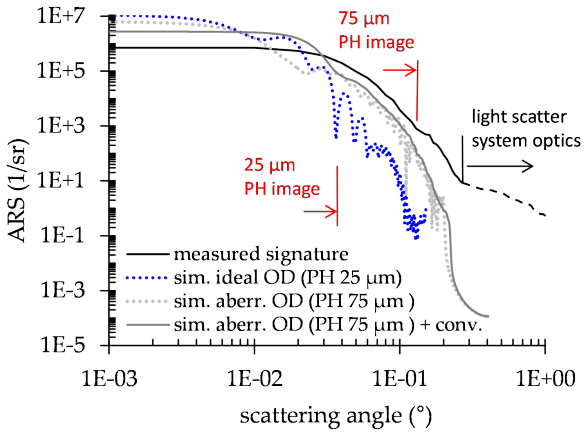

Figure 3.13: Measured near angle signature compared to ZEMAX beam profile simulations: ideal optic design (25 µm pinhole size, see chapter 3.3.2) and an optic design with additional artificial aberrations in front of the pinhole (75 µm pinhole size). The geometrical image size of the pinhole is marked for the 25 µm and the 75 µm pinhole.

Convolution of the ARS by the finite detector aperture are secondary, though, this smoothens scintillations and slightly broadens the beam. In practice, instead of the originally planned 25 µm pinhole (PH) from the optic design (chapter 3.3.2) a 75 µm PH had to be used for the spatial filter to avoid visible beam truncations. This already indicates that the beam size at the PH is not diffraction limited and probably results from surface irregularities and alignment uncertainties that were not included in the simulation. To simulate the effects of wavefront errors, artificial spherical aberration and higher order Zernike terms were introduced in the optic design to broaden the beam focus at the pinhole to about 50 µm in diameter. The simulation with this artificially aberrated optic design and the 75 µm PH (grey dotted line) was smoothed by a 0.05° moving average filter to introduce the aperture convolution effect (solid grey line). It shows a very good agreement to the measurement considering the double logarithmic scale and the fact that the measure of the aberrations was only estimated.

This explains the broadened beam profile (see chapter 3.3.2). Moreover, the beam profiles reveal a well correlation to the geometrically calculated pinhole images. Geometrical optics approaches [146] are consequently valid to estimate the beam focus width. The simulation confirms the assumption that the beam profile in this set-up is mainly degraded by surface irregularities and / or misalignment of the optics located in front of the PH. The peak height of $1 \cdot 10^7$ 1/sr of the simulation was not confirmed in the measurement. This can be explained by deviating aberrations in simulation and experiment.

A further improvement of the beam profile is consequently achievable by optimizing the beam preparation optics located in front of the PH. Similarly, the beam profile of the mirror illumination system was found to be limited by surface irregularities of the parabolic mirror in the spatial filter. This was experimentally verified by beam profile measurements with a CCD sensor at different positions in the illumination system.

Rayleigh scattering

The instrument signature originating from Rayleigh scattering at the air molecules can be calculated by [57, 112, 113]:

$$ARS_{Rayleigh,spol}(\theta_s) = \frac{4\pi^2(n_{air}-1)^2}{\lambda^4 N}\frac{d_{FOV}}{sin(\theta_s)} \ , \tag{3.19}$$

$$ARS_{Rayleigh,ppol}(\theta_s) = \frac{4\pi^2(n_{air}-1)^2}{\lambda^4 N}\frac{d_{FOV}}{sin(\theta_s)}\frac{1}{cos^2(\theta_s)} \ , \tag{3.20}$$

where d_{FOV} is the field of view diameter of the detector at the sample position, n_{air} the refractive index of the surrounding medium, and N the number of gas molecules per unit volume. The Rayleigh limited signature is linear to the enclosed volume in the intersection of the illumination beam and the detector FOV. With n_{air}=1.000293, N=2.68E19 1/cm³, λ=532 nm, and d_{FOV}=7 mm, $ARS_{Rayleigh,spol}(\theta_s)$ can be calculated and compared to the measured instrument signature, which shows a remarkably good agreement (see Fig. 3.14).

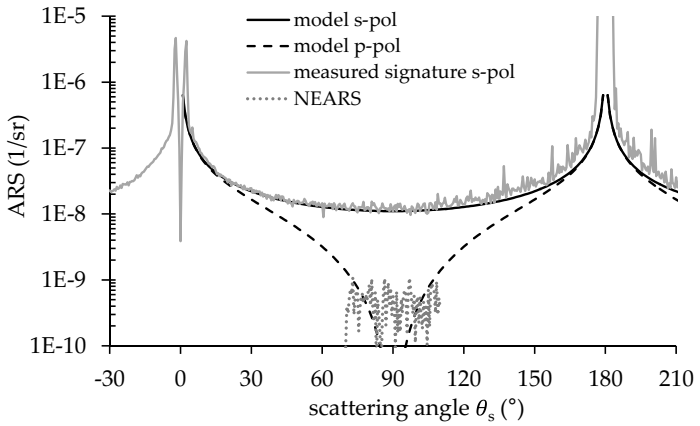

Figure 3.14: Measured instrument signature of the mirror system compared to the modeled Rayleigh limit for a FOV of d_{FOV}=7 mm at the sample surface location.

Obviously, the instrument signature is predominantly Rayleigh limited, except for the near angle scattering and residual back scattering from the beam dump. This is achieved by a NEARS level of $5 \cdot 10^{-10}$ 1/sr. Further improvement of the Rayleigh limit is only possible by decreasing the detector FOV or by changing the surrounding medium (e.g. vacuum). Changing the surrounding medium is technologically complex and thus only reported for UV scatterometry where Rayleigh scattering becomes increasingly critical. Decreasing d_{FOV} below 7 mm is practically limited by the illumination spot size, especially at grazing angles of incidence. A thinkable - though technologically very complex - optimization would be an adjustable field stop.

Remarkably, fluctuations and light scatter level slightly increases towards the transmitted beam. This can be explained by floating particles that contribute scattered light when they randomly pass the illumination beam (the Mie scattering model predicts an increased light scattering in the forward direction [147]). The number and size of particles can be easily reduced by placing the instrument in a clean room or inside a laminar flow box, however, the

effect regarding instrument signature is not “particularly” high.

However, rarely samples exist with an ARS level below the s-pol Rayleigh-limit of the instrument. A further reduction of the Rayleigh scattering limit is consequently not worthwhile.

Light scattering from system optics

A significant part of the near angle signature is dominated by scattered light from the system optics that are located after the pinhole. However, there exists no analytic treatment capable to completely describe this effect.

In the following, an analytic model will be derived that enables to predict the near angle signature from ARS or PSD data of the optical elements in the illumination system and the instrument geometries. It is used to identify the dominating scattering element in the system optics and for signature optimization. Moreover, the near angle signature for curved samples becomes also predictable, which was previously only examined by ray tracing simulation [146]. This is especially helpful as the instrument signature is significantly influenced by curved samples which makes it hard to discriminate between scattered light of the sample and the instrument.

Peterson showed that light scattering from a multi-element system can be analytically calculated from the individual ARS functions of the optical components [148], which was confirmed by comparing the model to simulations of a raytracing software [149]. Choi [150] later proved that the point spread function (PSF) of an optical system caused by aberrations and light scattering can be calculated by the convolution of the geometrical PSF (aberrations) with the scattered light PSF. Both Peterson and Choi did not investigate vignetting effects at the system apertures. However, vignetting at the detector field aperture significantly influences the shape of the near angle signature of scatterometers.

Model description: Please note that the local scattering angle coordinates of the individual optical components and the scattering angle coordinates of the instrument are denoted with θ_{sc} and θ_s, respectively.

An optical system (see Fig. 3.15) with N components j is assumed, only the first system component with j=1 is curved. The power $P_{s,j}$ from the optical element M_j, scattering with $ARS_j(\theta_{sc,j})$ and located in the distance z_j from the detector aperture, is scattered into the detector aperture A_{det}:

$$P_{s,j} = ARS_j(\theta_{sc,j}) \cdot P_i \cdot \frac{A_{det}}{z_j^2} \ . \tag{3.21}$$

The effect of the scattered light on the instrument signature ARS_{sig} for N components is then calculated by:

$$ARS_{sig}(\theta_s) = \frac{\sum_{j=1}^{N} P_{s,j}}{P_i} \cdot \frac{r_{sweep}^2}{A_{det}} = \sum_{j=1}^{N} \frac{r_{sweep}^2}{z_j^2} \cdot ARS_j(\theta_{sc,j}) \ . \tag{3.22}$$

Inserting $\theta_s = \theta_{sc,j} \cdot z_j / r_{sweep}$ from instrument geometries, where r_{sweep} denotes the receiver arm length, leads to

$$ARS_{sig}(\theta_s) = \sum_{j=1}^{N} k_j(\theta_s) \frac{r_{sweep}^2}{z_j^2} ARS_j(\theta_s \frac{r_{sweep}}{z_j}) \ , \tag{3.23}$$

where $k_j(\theta_s)$ is an attenuation factor between 0 and 1 to model the FOV clipping effects. ARS_{sig} is simply the sum of the ARS_j of the individual components weighted by the instrument geometries. Considering Eq. (3.23), it is tempting to state that - besides minimizing the number of optical components N and their individual ARS_j level - the near angle scattering $ARS_{sig}(\theta_s)$ can be minimized by making z_j as large, and r_{sweep} as small as possible. However, as will be shown this is not generally case.

A similar condition of Eq. (3.23) can be derived for the instrument signature if the sample has the focal length f'_{sample}

$$ARS_{sig}(\theta_s) = \sum_{j=1}^{N} k_j(\theta_s) \frac{\overline{\beta}_{sample}^2 r_{sweep}^2}{\left(z_j + r_{sweep}(\overline{\beta}_{sample} - 1)\right)^2} ARS_j \left(\theta_s \frac{\overline{\beta}_{sample} r_{sweep}}{z_j + r_{sweep}(\overline{\beta}_{sample} - 1)}\right) \ , \tag{3.24}$$

where $\overline{\beta}$ is the magnification of the virtual image of the detector aperture by the sample. It is calculated by

$$\overline{\beta} = \frac{f'_{sample}}{f'_{sample} - r_{sweep}} \ . \tag{3.25}$$

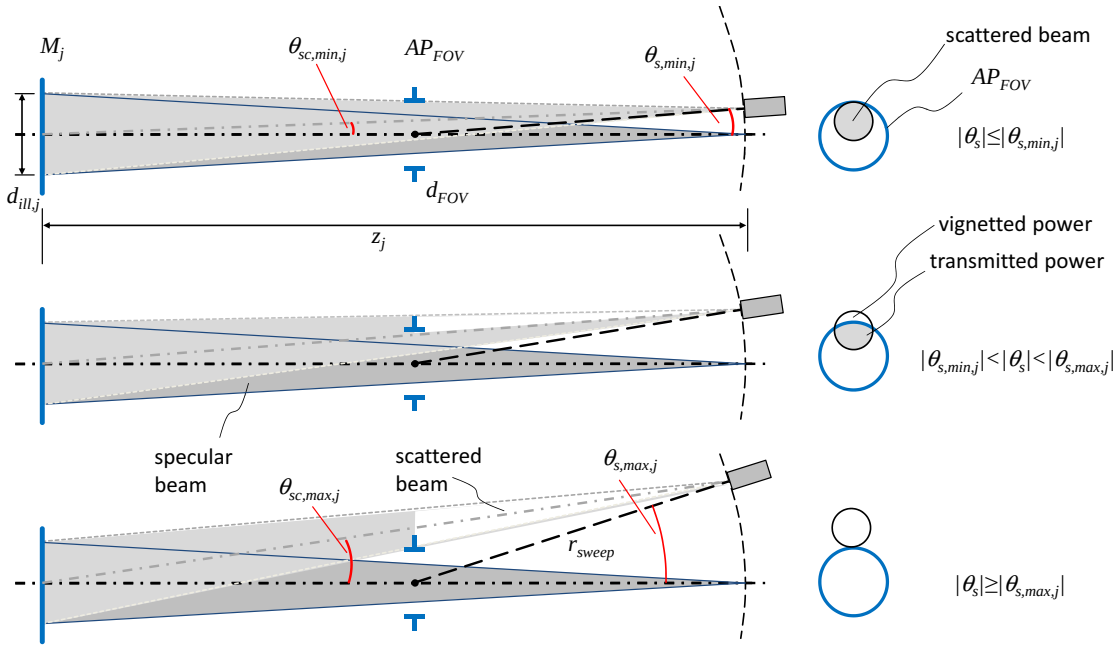

Figure 3.15: Near angle scattering from the system opics M_j vignetted by the virtual image of the field stop AP_{FOV}.

The obscuration factor $k_j(\theta_s)$ can be calculated from the scattering angles $\theta_{s,min,j}$ and $\theta_{s,max,j}$ where the scattered light of an optical component from the instrument is completely unvignetted or completey vignetted by the virtual image of the detector field stop, respectively (see Fig. 3.15). Between the angles $\theta_{s,min,j}$ and $\theta_{s,max,j}$ the ARS_j is only vignetted partially. The obscuration can be calculated by the normalized intersection of the scattered beam pro-

file and the virtual image of the field stop. For the sake of simplicity, the decrease in scattered illuminance from $\theta_{s,min,j}$ to $\theta_{s,max,j}$ is assumed to be linear with θ_s:

$$k_j(\theta_s) = \begin{cases} 0 & \text{if} \quad |\theta_s| < \theta_{s,max,j} \\ \dfrac{|\theta_s| - \theta_{s,max,j}}{\theta_{s,min,j} - \theta_{s,max,j}} & \text{if} \quad \theta_{s,min,j} < |\theta_s| < \theta_{s,max,j} \\ 1 & \text{if} \quad |\theta_s| > \theta_{s,min,j} \end{cases} . \tag{3.26}$$

The scattering angle $\theta_{s,max,j}$ was previously described by Klicker et. al. [151]. However, it was only used as a to be minimized design criterion to separate the near angle from the far angle signature. It includes effects of curved samples with the focal length f'_{sample}. A similar condition is here derived for the scattering angle $\theta_{s,min,j}$:

$$\theta_{s,max,j} = \frac{d_{FOV} + d_{ill,j}}{2(z_j - r_{sweep})} + \frac{d_{FOV}}{2r_{sweep}} - \frac{d_{FOV}}{2f'_{sample}} , \tag{3.27}$$

$$\theta_{s,min,j} = \frac{d_{FOV} - d_{ill,j}}{2(z_j - r_{sweep})} + \frac{d_{FOV}}{2r_{sweep}} - \frac{d_{FOV}}{2f'_{sample}} , \tag{3.28}$$

where d_{FOV} denotes the diameters of the detector field of view in the sample plane; and $d_{ill,j}$ the diameter of the illumination beam at M_j. As Eq. (3.27) and (3.28) only differ in the sign of $d_{ill,j}$, it becomes clear that $d_{ill,j}$ only influences the width of the spacing between $\theta_{s,min,j}$ and $\theta_{s,max,j}$. Trivially, a sample with positive focal length narrows the near angle signature, while a sample with negative f'_{sample} broadens it. Assuming $f'_{sample} = \infty$ and $d_{ill,j} \to 0$ leads to the mean obscuration angle θ_{obs}:

$$\theta_{obs} = \frac{d_{FOV}}{2} \left(\frac{1}{z_j - r_{sweep}} + \frac{1}{r_{sweep}} \right) . \tag{3.29}$$

The role of instrument geometries: Consequently, the near angle signature can be optimized by minimizing its width θ_{obs} (Eq. (3.29)) and by minimizing its level $ARS_{sig}(\theta_s)$ (Eq. 3.23).

Eq. (3.29) allows to calculate optimal instrument geometries for a minimized signature width:

- If z_j corresponds to the total instrument length, which is typically the case for most laboratory instruments, a minimum search of Eq. (3.29) shows that optimal instrument geometries (minimized θ_{obs}) are achieved for the trivial case $r_{sweep} = z_j/2$.
- If the available space or mechanical reasons restrict r_{sweep}, optimal instrument geometries (minimized θ_{obs}) are achieved by simply maximizing z_j. This is the case for this table top instruments because of the two illumination beam folding mirrors.
- Especially interesting is the case $z_j < r_{sweep}$, which corresponds to the periscope mirror in front of the detector: θ_{obs} can minimized by moving the periscope mirror as close as possible to the detector aperture (beam focus). A periscope mirror at the detector system consequently allows to increase r_{sweep} while its contribution to the near angle scattering signature is low.

The first two points are partly contradictory to Eq. (3.23), where a *small* r_{sweep} decreases the ARS_{sig} level. This will be discussed in the following.

To give a better insight on the effect of scaling the ARS_{sig} *level* by instrument geometries, the ARS functions of the elements M_j are expressed in an analytic form, an approach also used in [148]. Within limited ranges of the scattering angle, the shape of the BSDF from optically smooth surfaces can often be well described by a function with constant slope s_j on a log-log scale. The often so called two-parameter Harvey model shows this property and is defined as [9]:

$$BSDF(\theta_{sc}) = b\,(100\,|sin\theta_{sc} - sin\theta_i|)^{s_j} \quad , \tag{3.30}$$

Typically optical components can be described for s lying in the range of $-3 < s_j < -1$ [148]. Here, the optical components used for the beam preparation were measured with $-3.4 < s_j < -1.7$ (retrieved from ARS calculation based on PSD data of topography measurements [152]). For small angles and using the denotation from the earlier paragraphs Eq. (3.30) leads with Eq. (3.23) to:

$$ARS_{sig}(\theta_s) = \sum_{j=1}^{N} k_j(\theta_s) \frac{r_{sweep}^2}{z_j^2} b_j \left(100 \left|\theta_s \frac{r_{sweep}}{z_j}\right|\right)^{s_j} \quad , \tag{3.31}$$

Assuming the special case $s_j = -2$ simplifies to

$$ARS_{sig}(\theta_s) = \sum_{j=1}^{N} k_j(\theta_s) b_j \left(100^{-2} \left|\theta_s^{-2}\right|\right) = \sum_{j=1}^{N} k_j(\theta_s) ARS_j(\theta_{sc,,j}) \ . \tag{3.32}$$

This is especially interesting as Eq. (3.32) has completely dropped the instrument geometry terms r_{sweep} and z_j, so that instrument size scaling would not influence the scatter level! Neither varying both the BSDF slope between $s_j = -1.5$ to $s_j = -2$ and the instrument geometries between typical values of r_{sweep}/z_j=0.2 and 0.5 (more than doubled instrument size) affects the signature ARS level to a large extend. The $ARS_{sig}(\theta_s)$ of the largest instrument layout (with the best optic) is only by about a factor of 2 lower than the most compact layout (with the worst optic), which is less than a half OOM. Yet, for local slopes with $s_j < -2$ the ARS level can even raise by increasing the distance z_j or decreasing r_{sweep}![7]

To sum up, the signature level $ARS_{sig}(\theta_s)$ level can only be marginally altered by scaling instrument geometries (small r_{sweep}), while the signature width can be effectively narrowed (large r_{sweep}). Optimizing r_{sweep} and z_j for a small signature width is consequently the more fruitful approach. This corresponds to the proposed axes layout where a periscope mirror in front of the detector is used to artificially increase r_{sweep} (see chapter 3.3.2).

Experimental: To analyze the contributions of the used optical components on the near angle signature of the instrument, the ARS at very small scattering angles has to be known for each of the mirrors M1 to M4 (see Fig. 3.16 left), respectively. The signature relevant local scattering angles of each mirror can be calculated from the instrument geometries by means of Eq. (3.27) and Eq. (3.28), and range between θ_{sc}=0.04° and θ_{sc}=1.8°. It is obvious

[7] However, towards very low spatial frequencies the PSD may get saturated (which is sometimes referred to as the "knee" of the PSD [3]), yet, this region is typically only reachable by impracticable distances.

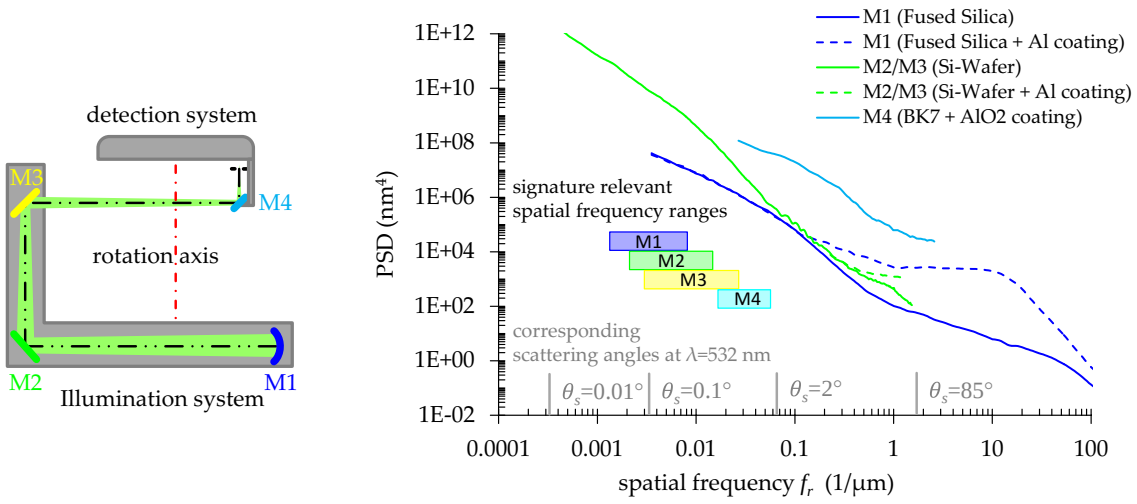

Figure 3.16: Left: sketch of the mirror positions. Right: PSD data of the individual optical components with their spatial frequency ranges relevant for the near angle signature.

that the ARS at these small scattering angles are hard to determine by light scattering measurements, especially with the same instrument they are integrated in. Two approaches are pursued: extrapolating the measured ARS of the components towards smaller scattering angles, and calculating the ARS from topographic measurements.

Hence, the master PSDs of all components were determined, for M1 to M3 both of the uncoated and aluminum coated substrate [152]. It becomes obvious that the roughness growth of the Al coatings has no influence at near angle signature relevant scattering angles (see signature relevant spatial frequencies in Fig. 3.16). For both approaches, the parameters s_j and b_j are derived by fitting Eq. (3.30) to the ARS data within the relevant scattering angles. The near angle signature is now calculated by means of Eq. (3.31) for the instruments geometries $r_{sweep} = 250\,mm$, $d_{ill} = 1.5\,\text{mm}$, $d_{FOV} = 7\,\text{mm}$; z_j is 1300 mm, 820 mm, 540 mm, and 100 mm for M1 to M4, respectively (s_j and b_j are listed in Fig. 3.17). The results are plotted in Fig. 3.17 and compared to a near angle scattering measurement of the instrument.

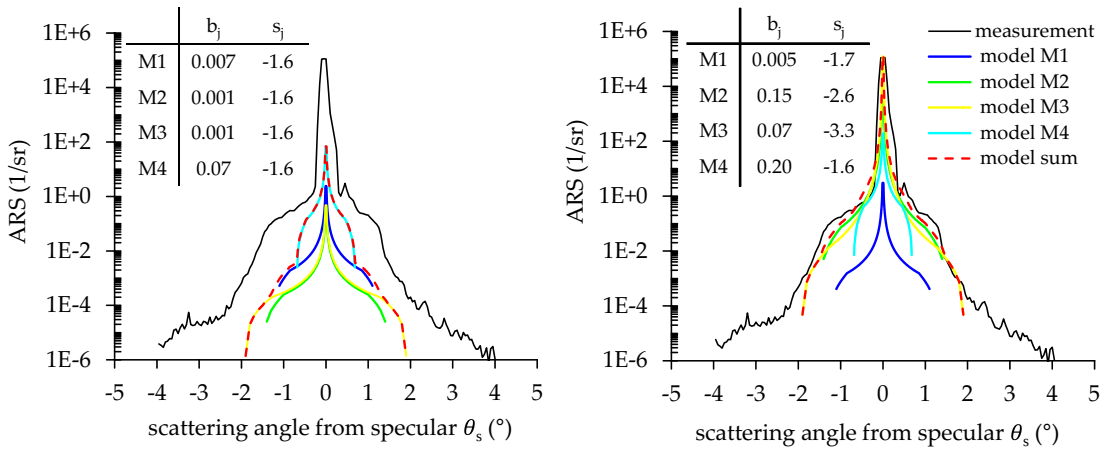

Figure 3.17: Modeled near angle signature compared to measurement data: (left) based on measured far angle ARS data extrapolation; (right) based on ARS calculation from PSD data.

The modeled signature based on topographic measurement shows a very good agreement to the measured near angle signature. However, the modeled signature based on ARS data extrapolation exhibits an underestimated signature by about two orders of magnitude. This error originates in particular from the mirrors M2 and M3, where the slopes in the PSDs show a rather large local variation compared to those of M1 and M4 (see 3.16). Describing ARS data by only two parameters can consequently lead to significant deviations in light scattering predictions when the region of validity is unknown.

Discussion: As the validity of the model is now confirmed by measurement, the effect of different parameters can be further examined. The following conclusions are summarized:

- First of all, the model shows that the near angle scattering of the instrument is dominated by M2. Hence, the near angle signature resulting from scattered light of the system optics can be further optimized by replacing M2 with lower scattering optics. Replacing M1 or M4 with lower scattering mirrors has no effect.
- The periscope mirror in front of the detector was introduced in the optic design and axes layout (chapter 3.3.2) to reduce NA (better beam profile), to reduce obscuration of the incident beam, and to artificially extend r_{sweep} (improves the specular near angle limit) without increasing instrument size.
  Fig. 3.18 shows the calculated performance of a corresponding system design without periscope mirror, where a smaller sweep radius (r_{sweep} is reduced by the 100 mm periscope arm length) is traded for less optical surfaces: clearly, the shortened r_{sweep} has a larger impact (by reducing θ_{obs}) on the near angle signature than the missing light scattering contributor. This confirms the favored periscope concept perused in chapter 3.3.2 and constitutes a significant improvement of the near angle signature.
- Fig. 3.18 (right) shows the effect of sample curvature on the near angle signature calculated by Eq. (3.24). The model is compared to ray tracing simulation using the commercial software FRED [153] for different focal lengths of the sample. Model and simulation show a remarkably good agreement for samples with low to medium refractive power. For samples with short focal length the paraxial approximation loses validity and affects deviations.
- Minimizing the illumination beam diameter and the detector FOV affect a better near angle signature regarding scattering of the system components (though the diffraction limit is impaired). However, regarding FOV and illumination spot alignment uncertainties, a good compromise was already chosen for the FOV.
- A sample with positive focal length (concave mirror) leads to a better near angle signature (when aberrations can be neglected), while a sample with negative focal length (convex mirror) degrades it. This can be especially interesting when scatter sources other than surface scattering need to be examined (e.g. for the analysis of particle scattering it would be advantageous to deposit particles on curved surfaces rather than on plane substrates). The resulting influence on the signature can be calculated with this model and used to separate sample scattering from the instrument signature in post measurement analysis.

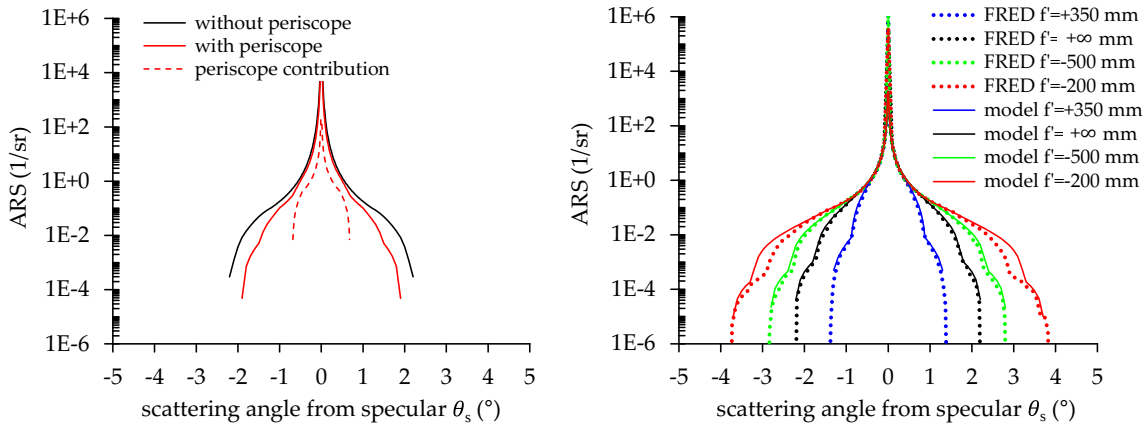

Figure 3.18: Left: effect of the periscope mirror and sample curvature on the near angle scattering. Right: the focal length of the sample is compensated by a prefocused illumination system. The model is compared to raytracing simualtions (FRED) for different focal lengths of the sample.

- Maximizing the optical distances is not a generally valid solution to optimize near angle scattering. Its effect on the signature scattering *level* can be comparably low or even worsen the performance. Moreover, because of a possible inconstant slope in the PSD, some surfaces are capable of featuring intermediate values of z_j for which near angle scattering can be minimized in a scattering angle regime or lateral region of interest.
- The roughening of optical surfaces by thin film coatings has no effect on the near angle signature as it increase light scattering only outside relevant scattering angles (see Fig. 3.16). This allows to use multilayer coatings optimized for high reflectance (or transmittance) and low depolarization.

3.6.2 Cross-talk

As pointed out in chapter 3.5, the cross-talk performance is critical for multiplexed high-end ARS measurements. To confirm the model described in chapter 3.5, two channels are used to characterize cross-talk between the individual channels of the instrument. Multi-wavelength ARS measurements (λ=405 nm, 532 nm, and 640 nm) are conducted at a polished nickel surface and compared to conventional sequentially performed measurements.

To characterization crosstalk as a function of modulation frequency, channel 1 is rectangularly modulated at f_1=999.8 Hz with the laser 1 blocked, while channel 2 is modulated from f_2=1 Hz to 1100 Hz with the corresponding laser opened. Only the signal of channel 1 is recorded which yields the crosstalk from channel 2 into channel 1. The measurement is compared to the model calculated by Eq. (3.9) and Eq. (3.14) for rectangular modulation. The LIA was set to τ=50 ms with the low pass filter set to 6 dB (equals N=1).

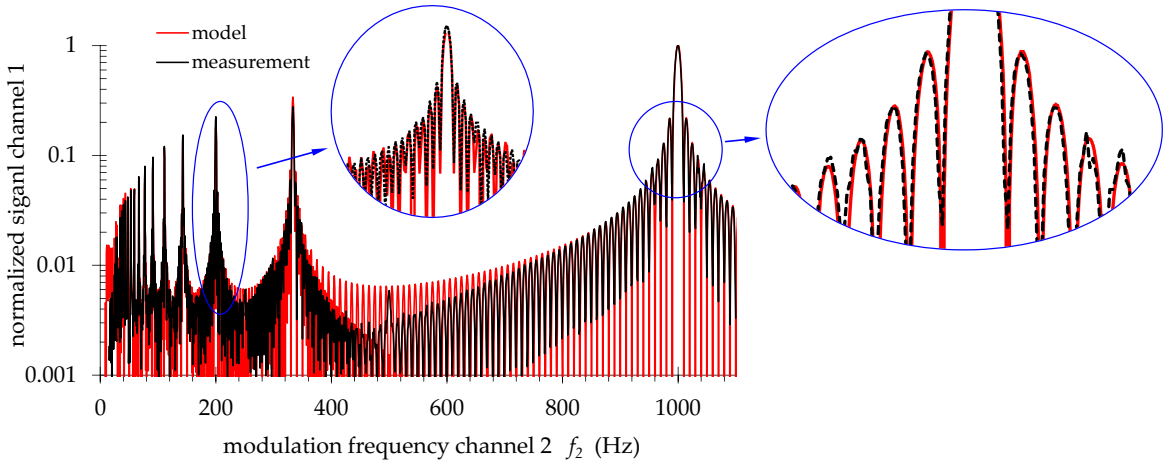

Figure 3.19: Crosstalk from channel 2 into channel 1 as a function of the modulation frequency of channel 2.

Model and measurements show a good resemblance. The zeros described in the model are clearly visible in the measurement and represent modulation frequencies for channel 2 with optimized crosstalk performance. Only between f_2=400 Hz and 700 Hz slight deviations in the crosstalk level are visible, however, the locations of the zeros still agree. An explanation for the difference in the crosstalk level in this range of f_2 are possible deviations of the assumed rectangular weighted window function from the unknown window function of the LIA. The pronounced peaks (at f_2=333 Hz, f_2=200 Hz, ...) result from the higher orders of the rectangular modulated signal and should be absolutely avoided to reduce crosstalk. The hook at f_2=500 Hz origins from the slightly asymmetric rectangularly shaped signal.

Fig. 3.20 shows crosstalk from channel 2 into channel 1 and signal noise as a function of the signal ratio. For this experiment, channel 1 was modulated at f_1=990.8 Hz, while the frequency of channel 2 was adapted so that either high crosstalk (f_2=945.8 Hz) or low crosstalk (f_2=940.8 Hz) was expected. Furthermore, two different LIA settings where used where with either a first order low pass filter (6 dB) or a second order lower pass filter (12 dB).
The experiment was conducted by configuring the power of laser 1 (532 nm, channel 1) to yield a constant signal of $V_{1,ideal}$=130 µV when laser 2 was blocked. Hence, the power of

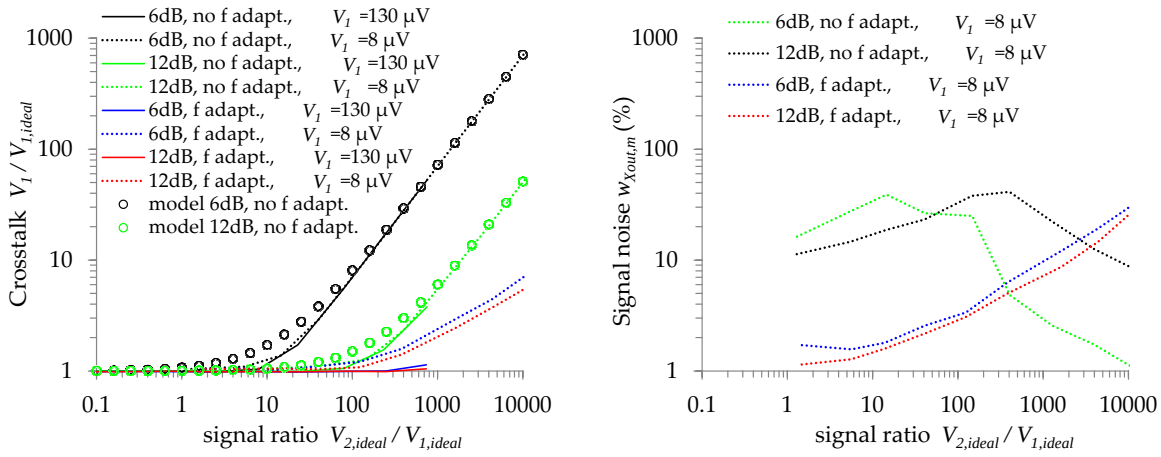

Figure 3.20: Crosstalk (left) and signal noise (right) as a function of the signal ratio $V_{2,ideal}/V_{1,ideal}$. The experiments were performed for different LIA low pass settings (6 dB and 12 dB), with (f adapt.) and without (no f adapt.) frequency adaption, and for different levels of the signal $V_{1,ideal}$.

laser 2 (405 nm, channel 2) was varied to yield signals between 10 µV $< V_{2,ideal} <$ 100 mV, while the signal level of channel 1 V_1 and its signal noise was determined for each data point, respectively. Therefore, for each data point, 100 signal values were recorded from which both the relative standard deviation $w_{Xout,1}$ and the average V_1 were determined. The experiment was repeated for $V_{1,ideal}$=8 µV; Also, crosstalk was calculated according to Eq. (3.11).

Model and measurement show a good agreement (see Fig. 3.20): Although the model differs more for low crosstalk values from the measurement, it is capable to generally predict the crosstalk performance, which is sufficient to configure the modulation frequencies. As predicted, crosstalk performance and signal noise visibly improve by adapting the modulation frequencies by means of Eq. (3.17), and with higher order low pass settings in the LIA. Obviously, non-adapted modulation frequencies impact, as predicted, especially signal noise that results in dominating measurement uncertainties for dynamics of higher than 1 OOM. However, by adapting the modulation frequencies a signal dynamic of about 2 OOM between the individual channels can be achieved.

Hence, this enables the measurement of samples where the dynamic between the channels is lower than 2 OOM, which is sufficient for smooth surface scattering samples for λ=405 nm and 640 nm. However, additional dynamic induced by the attenuation system to adapt the overall illumination power onto the detector has to be considered (even the attenuation of ND filters is a function of λ).

To achieve the aspired 8 OOM dynamic range for parallel ARS measurements, optical adaption is additionally necessary (see chapter 3.5.2). Therefore, the attenuation filters can be configured to optical density steps of 3 OOM[8]. This matches well to the optical density steps of the filters to adapt the total illumination (in the combined beam, see chapter 3.3.2), which are configured to 2.5 OOM.

Fig. 3.21 shows IP ARS measurements at three illumination wavelengths (405 nm, 532 nm,

[8] As (±) 2 OOM signal dynamic between the individual channels can be tolerated if the modulation frequencies are adapted, an attenuation of the highest signal by 4 OOM dynamic is possible.

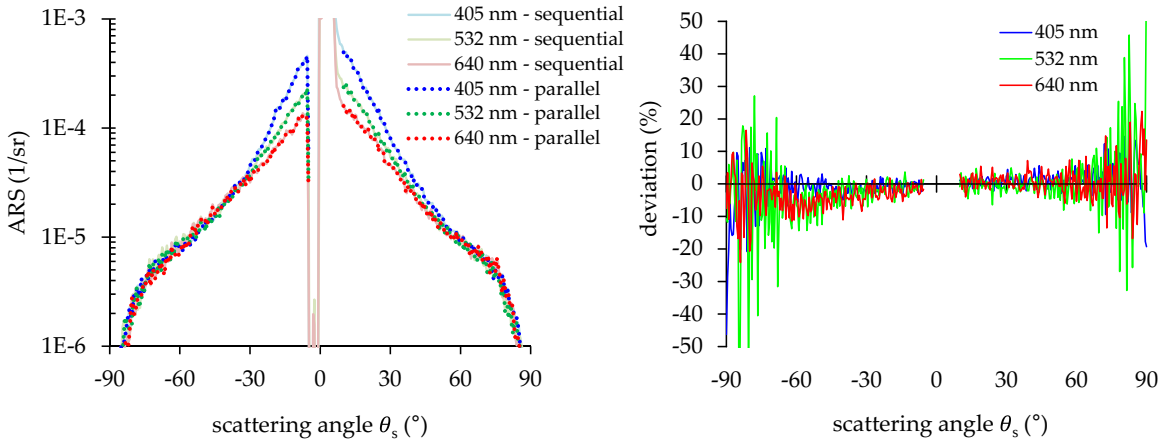

Figure 3.21: Left: Parallel ARS measurements of an aluminum substrate with a nickel top coating at three wavelengths (405 nm, 532 nm, and 640 nm) compared to conventional sequential ARS measurements of the same sample. Right: Relative deviations of the sequentially and parallel performed measurements.

and 640 nm) of a polished diamond turned aluminum substrate with a nickel top coating. The angle of incidence is θ_i=3°, illumination s-polarized, illumination spot diameter 1 mm, and the detector's solid angle was chosen to $\Delta\Omega_s = 2.4 \cdot 10^{-4}$ sr for $\Delta\theta_s$=0.5° steps. The ARS measurements were performed conventionally at first, with only one illumination wavelength while the others where blocked, sequentially for all three wavelengths, respectively. Afterwards, the measurements were repeated with the parallel measurement channels concept and all lasers illuminating the sample at once. All LIAs where set to τ=50 ms with the low pass filter set to 12 dB. Modulation frequencies where chosen to 7.005 kHz, 0.955 kHz, and 12.105 kHz with respect to Eq. (3.17), for channel 1 to 3, respectively. The parallel measurements fit the sequentially performed ARS measurements very well with rms deviations of 6.4%, 11.2%, and 5.0%, for 405 nm, 532 nm, and 640 nm illumination, respectively. The larger deviations at large scattering angles can be traced back to ordinary signal noise, as the NEARS for this measurement was slightly under 10^{-6} 1/sr because of the small illumination beam diameter.

To sum up, the experiments proved that a dynamic range of 2 OOM between the individual channels can be achieved by optimizing the demultiplexing parameters. This limits both noise and crosstalk below 8%, which enables multiplexed ARS measurements of low scattering samples. By introducing optical adaption, as proposed in chapter 3.5, the dynamic range can be further extended to e.g. 8 OOM. This allows even grating sample to be measured with multiplexed illumination wavelengths.

3.6.3 Measurement uncertainty

"At least two numbers are required if an experiment is to give a result and a measure of its reliability" - N. C. Barford [154][9].

Measurement uncertainty budgeting is an important tool to characterize the precision of a measurement instrument and the significance of its direct or derived measures. A comprehensive uncertainty analysis is mandatory to acquire an ISO17025 certificate for testing and calibration laboratories [37]. The GUM [156] (Guide to the expression of uncertainty in measurement) has been developed to provide an international consensus for the expression of uncertainty in measurements. Although comprehensive analysis of ARS/BSDF uncertainty were previously performed in [56, 157], these models are based on the "total power" calibration (see chapter 2.1.2), which lacks traceability to a national or international ARS standard (requested for ISO17025 certification for calibration laboratories [37]).

This chapter will provide an uncertainty analysis for the scatterometer described in this work based on the "relative normalization" calibration (see chapter 2.1.2) and orientated to GUM. The herein developed model includes a detailed analysis of system and sample misalignment effects, which were previously estimated[10]. After the mathematical description of the model, the individual uncertainties are derived from measurements. The combined measurement uncertainty as a function of scattering angle is exemplarily shown for a polished sample.

Model description

The ARS of the instrument is calculated by (see chapt. 3.4.2)

$$ARS(\theta_s) = \frac{V_{det}(\theta_s)}{V_{det,r}(\theta_{s,r})} \frac{\prod_{b=1}^{i_r(V_{det,r})} T_{att,r_{b,b-1}}}{\prod_{b=1}^{i(V_{det})} T_{att_{b,b-1}}} ARS_{cal}(\theta_s) \ , \tag{3.33}$$

which allows the separation of the individual uncertainties on the $ARS(\theta_s)$:

- Influences on $V_{det}(\theta_s)$:
  - Signal drifts: $u_{det,drift}(V_{det})$, Type B, PDF: rectangular

    Signal drift results from laser power drifts and pointing instabilities. It is negligible when calibration is refreshed on a regular base.
  - Non-linearity: $u_{det,NL}(V_{det})$, Type B, PDF: rectangular

    Non-linearity is low for PMTs [128] when the measurement chain is correctly designed. It is a function of the PMT's output current while being independent on the incident light wavelength.
  - Signal noise: $u_{det,noise}(V_{det})$, Type B, PDF: normal

    Is a function of the signal-to-noise ratio and thus a function of the signal voltage level. Noise in PMTs is commonly dominated by thermionic emission of electrons

[9] Quotation from Keith Birch [155].

[10] The BRDF uncertainty models developed by Cady and Schiff [56, 157] are using the $cos^{-1}\theta_s$ therm of the BRDF to introduce θ_s uncertainties resulting from misalignment. However, as the ARS has no θ_s therm, this would anticipate the lack of alignment uncertainties for ARS measurements.

at the photocathode, other sources are leakage current, shot noise, field emission, and noise originating from parts of the residual measurement chain [128].

  - Speckle:
    Regarded as a sample specific characteristic, speckle are consequently not related to measurement uncertainty.
  - Misalignment: $u_{det,align}(V_{det})$, Type B, PDF: normal
    System and sample misalignment leads to an assignment of recorded ARS values to wrong scattering angles. This can be traced to uncertainties in the signal value which increase with the slope of the ARS and are consequently higher in the near specular region. Furthermore, misalignment leads to a deviating angle of incidence which changes the light scattering characteristics of the sample. The usually long receiver arm length (>200 mm) also results in a negligibly low solid angle uncertainty resulting from sample misalignment (deviations of r_{sweep} are much smaller than 1 mm).
  - Aperture insertion repeatability:
    Negligible low.

- Influences on $V_{det,r}(\theta_s)$:
  - Reference sample inhomogeneity/anisotropy: $u_{det,r}(V_{det,r})$, Type B, PDF: normal
    Deviations in the measurement position and azimuthal orientation of the reference sample between the external calibration and the relative normalization measurement introduce uncertainties according to the homogeneity and isotropy characteristics of the sample. This uncertainty can be minimized by marks on the reference sample to ensure a repeated positioning.
  - Signal drifts:
    Negligible because of short calibration times.
  - Non-linearity:
    Non-linearity uncertainty is zero for the calibrated ARS level.
  - Signal noise:
    Signal noise is negligibly small versus inhomogeneity error because of the large number of measured values during calibration. However, the residual signal noise uncertainties are included in $u_{det,r}(V_{det,r})$, which is determined from multiple performed calibrations.
  - Speckle:
    Calibration uncertainty as a result of speckle effects increases with smaller detector apertures, larger illumination wavelengths, and smaller illumination spot size. The effect can be reduced by calibrating over a broader θ_s or ϕ_s range. It is included in $u_{det,r}(V_{det,r})$.
  - Misalignment:
    Negligible as Spectralon is a good Lambertian scatterer at low angles of incidence ($\theta_i \lessapprox 20°$) [158] that is insensitive to misalignment to a high degree. Residual uncertainties are included in $u_{det,r}(V_{det,r})$.

- Influences on $T_{att_{b,b-1}}$
  - Uncertainty of the attenuation level transmission measurement: $u_{att,TM}(T_{att_{b,b-1}})$, Type B, PDF: normal
    It results from signal noise and the limited attenuation repeatability. It represents the systematic attenuation calibration uncertainty with the same value and sign as $u_{att,r,TM}(T_{att,r_{b,b-1}})$. Signal noise effects can be reduced by averaging a high number of signal values.
  - Attenuation level uncertainty (resulting from limited repeatability) during measurement: $u_{att,rep}(T_{att_{b,b-1}})$, Type B, PDF: normal
- Influences on $T_{att,r_{b,b-1}}$
  - Uncertainty of the attenuation level transmission measurement during the relative calibration measurement: $u_{att,r,TM}(T_{att,r_{b,b-1}})$, Type B, PDF: normal
    It represents the systematic attenuation calibration uncertainty with the same value and sign as $u_{att,TM}(T_{att,r_{b,b-1}})$.
  - Attenuation level uncertainty (resulting from limited repeatability) during the relative calibration measurement: $u_{att,r,rep}(T_{att_{b,b-1}})$, Type B, PDF: normal
- Influences on ARS_{cal}
  - ARS uncertainty of calibration facility $u_{ARS,cal}(ARS_{cal})$, Type B, PDF: normal
    The uncertainty data is received from calibration facility.

With Eq. (3.33) this leads to:

$$\begin{aligned} \mathrm{ARS}(\theta_s) &= \frac{V_{det}(\theta_s)k_{det,noise}k_{det,drift}k_{det,NL}k_{det,align}}{V_{det,r}k_{det,r}} \\ &\cdot\frac{\prod_{b=1}^{i_r}T_{att,r_{b,b-1}}k_{att,r,TM,b}k_{att,r,rep,b}}{\prod_{b=1}^{i}T_{att_{b,b-1}}k_{att,TM,b}k_{att,rep,b}}\cdot ARS_{cal}(\theta_s)k_{ARS,cal}\ . \end{aligned} \tag{3.34}$$

where the individual uncertainties k are assumed as factors with a mean of 1. As the systematic errors of the measured filter transmission factors are identical in measurement and calibration $k_{att,TM} = k_{att,r,TM}$, they cancel each other if the attenuation level in the measurement is the same as it was in the calibration sample measurement. As in Eq. (3.34) the single quantities are considered as independent and are only products and quotients, the expression for $u(ARS(\theta_s))$ can be calculated by [156]:

$$\begin{aligned} \left(\frac{u(ARS(\theta_s))}{ARS(\theta_s)}\right)^2 &= \left(\frac{u_{det,noise}(V_{det})}{V_{det}}\right)^2+\left(\frac{u_{det,drift}(V_{det})}{V_{det}}\right)^2+\left(\frac{u_{det,NL}(V_{det})}{V_{det}}\right)^2 \\ &+\left(\frac{u_{det,align}(V_{det})}{V_{det}}\right)^2+\left(\frac{u_{det,r}(V_{det,r})}{V_{det}}\right)^2+\left(\frac{u_{ARS,cal}(ARS_{cal})}{ARS_{cal}}\right)^2 \\ &+\sum_{b=min(i,i_r)+1}^{max(i,i_r)}\left(\frac{u_{att,TM,b}(T_{att_{b,b-1}})}{T_{att_{b,b-1}}}\right)^2 \\ &+\sum_{b=1}^{i}\left(\frac{u_{att,rep,b}(T_{att_{b,b-1}})}{T_{att_{b,b-1}}}\right)^2+\sum_{b=1}^{i_r}\left(\frac{u_{att,r,rep,b}(T_{att,r_{b,b-1}})}{T_{att,r_{b,b-1}}}\right)^2 \end{aligned} \tag{3.35}$$

Apparently, the attenuators have a major contribution to the combined uncertainty, which suggests paying special effort on optimizing their repeatability, as well as reducing the number of different attenuation levels. If the calibration uncertainty $u_{det,r}(V_{det,r})$ is determined by repeatedly performed calibrations with filter level changes, it already includes the attenuation repeatability uncertainty and the last sum of Eq. (3.35) drops.

Determination of the individual uncertainties

To calculate the combined uncertainty of the instrument, almost all contributions can be determined from measurement. Only $u_{det,align}(V_{det})$ is analyzed by means of a Monte Carlo simulation.

- Signal noise $u_{det,noise}(V_{det})/V_{det}$
  Measurement uncertainty resulting from signal noise in the measurement chain is a function of V_{det} and measurement conditions (lock-in amplifier settings, background light). The uncertainty $u_{det,noise}(V_{det})/V_{det}$ is here determined for typical measurement conditions (closed housing, lock-in time constant 50 ms, filter slope 12 dB/octave). Therefore, a total number of 100 signal values was recorded for V_{det} ranging between 1 µV to 100 mV, respectively (see table 3.1). A constant signal noise uncertainty over the whole dynamic range can be realized by adapting the lock-in integration times or the number of averaged signal values to the signal level.

V_{det} range (in V)	$u_{det,noise}(V_{det})/V_{det}$
$10^{-2} < V_{det} \leq 10^{-1}$	<0.3%
$10^{-3} < V_{det} \leq 10^{-2}$	<0.6%
$10^{-4} < V_{det} \leq 10^{-3}$	<1.0%
$10^{-5} < V_{det} \leq 10^{-4}$	<3.7%
$10^{-6} \leq V_{det} \leq 10^{-5}$	<26%

Table 3.1: Measurement uncertainty resulting from signal noise.

- Non-linearity $u_{det,NL}(V_{det})/V_{det}$
  Uncertainties resulting from non-linearity in the measurement chain can have a dominant contribution to the overall uncertainty of light scattering measurements as a result of the large dynamic range of scattering characteristics. For PMTs, non-linearity is strongly related to changes in the so called divider current, which flows through the resistors in the voltage divider circuit [128]. The divider current is low compared to the anode current for low incident illumination and the usually applied high supply voltage levels. However, for high incident illumination the divider current can significantly affect the PMT's output current and thus degrade linearity.
  The different methods proposed to determine non-linearity are reported to achieve about the same uncertainty in the post measurement analysis [159, 160]. Here, the measurement is performed by using the attenuation method with an uncalibrated attenuator at different signal levels V_{det}. Attenuation can be performed using neutral density (ND) filters [157], different apertures [161], or a high frequency chopper [162].

Using a chopper as an attenuator was found to be capable of reducing measurement uncertainties resulting from the limited manual positioning repeatability compared to an ND filter. For an ideal linear system, the transmission T_{ND} by the chopper is identical at all measured signal level pairs a denoted as $V_{0,a}$ and $V_{ND,a}$, where the first is the unattenuated and the latter the chopper attenuated signal. Deviations from the ideal linear detector response V_{ideal} are relatable to non-linearity $\Delta_{NL} = (V_{det} - V_{ideal})/V_{ideal}$. Data point positions of the $V_{det}(ARS)$ transfer function can be calculated by:

$$ARS_{ND,a} = T_{ND} ARS_{0,a} \ , \tag{3.36}$$

$$ARS_{0,a} = V_{0,a} G(1 + k_{NL,a}) \ . \tag{3.37}$$

where G is a gain factor and $k_{NL,a}$ the deviation factor from linearity. The equations were solved by optimizing the variables $ARS_{0,a}$, $ARS_{ND,a}$ and $k_{NL,a}$ by means of the merit function MF :

$$\mathrm{MF} = \sum \left(1 - V_a/(V_a - V_{interpol})/G\right)^2 \ , \tag{3.38}$$

where $V_{interpol}$ is the interpolated value between two neighboring signal values. This approach is valid for small V steps and many measures so that the transfer function can be assumed to be linear between three data points. Moreover it is assumed that the average of $V_{ND,a}/V_{0,a}$ represents the chopper attenuation T_{ND}. This consequently only allows to detect changes in the detection (non-) linearity, however, deviations from linearity are only expected at the minimum and maximum ratings of the PMT [128]. An absolute quantification of the transfer function can be performed by using two attenuators [157]. G was determined by an ordinary system calibration, all signal values were dark noise corrected. The resulting transfer and non-linearity function are shown in Fig. 3.22. The measurement chain shows a very linear behavior up to V_{det} ≈200 mV with good agreement to the specified maximum ratings of the used PMT (corresponds to V_{det} =300 mV). Deviations from linearity for V_{det} ≤100 mV are within $u_{det,NL}(V_{det})/V_{det}$=1.0% for a rectangular distribution function. Though the deviations seem to arise rather from measurement errors (chopper attenuation repeatability, signal noise) than from non-linearity, a more accurate measurement is not needed as the non-linearity error is typically dominated by other uncertainties. Consequently, the PMT and the measurement chain cover more than 5 OOM dynamic range without the need to correct non-linearity.

- Signal drift $u_{det,drift}(V_{det})/V_{det}$
  Signal drift origins not soley from laser power deviations, but also from laser pointing instabilities which affect a varying vignetted power at the beam diameter defining aperture. Lower signal drift uncertainties can consequently be achieved by choosing a bigger sample illumination diameter or by simply refreshing calibration. The power drift is evaluated by performing a 15 h long term signal measurement with the receiver in the specular beam (see Fig. 3.23). The normalized standard deviation was found to be $s_{det,drift}(V_{det})/V_{det}$ =3.8% when the laser was modulated with a mechanical chopper

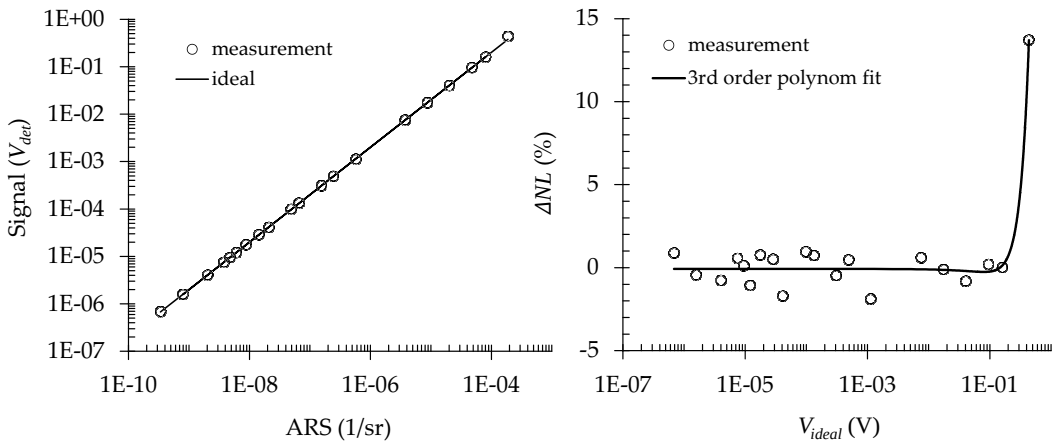

Figure 3.22: Non-linearity of the measurement chain.

at 1 kHz. The small visible outliers could be traced to irregularities in the chopping frequency. The probability of occurrence tends to increase with the lifetime of the chopper. They could be reduced by software filtering, though at the cost of increased measurement time. A recently available electronically modulated Nd:YAG laser was found to be a good replacement enabling an outstanding modulation frequency stability without the need of an external modulator. The signal drift could consequently be reduced down to $s_{det,drift}(V_{det})/V_{det}$ =2.4% without any occurring outliers.

- Attenuation
  Attenuation uncertainty arises from the limited mechanical repeatability of the filter positioners and filter inhomogeneity. Eq. (3.35) also shows that uncertainty grows with the number of attenuation levels. Still, the filters are required to cover seven OOM of beam attenuation additionally to the dynamic range of the PMT to yield a total of 12 OOM without changing the receiver's solid angle. As signal noise stays below 1% between voltage levels of 10^{-1} V and 10^{-4} V, the attenuator levels are configured to optical density steps of 2.5, respectively, which limits the amount of attenuation levels to three. Uncertainty for each filter level can be simply determined by repeatedly changing the filter level at the same ARS value and calculate the filter transmission according to Eq. 3.3. To reduce signal noise effects the signal at each filter level is averaged over N=40 values which yields a sufficiently small signal noise contribution of 0.17% (see signal uncertainties listed in table 3.1). Finally, uncertainty for all three filter transmission values yields $u_{att}(T_{att})/T_{att}$<1.0%. To reduce the uncertainty of the filter transmission measurement $u_{att,TM,b}(T_{att_{b,b-1}})/T_{att_{b,b-1}}$ for system calibration, the filter transmission is determined by averaging over N=10 filter level changes. This results in $u_{att,TM,b}(T_{att_{b,b-1}})/T_{att_{b,b-1}}$=0.3%.

- Relative normalization $u_{det,r}(V_{det})/V_{det}$
  The contribution $u_{det,r}(V_{det})/V_{det}$ is simply determined by repeatedly performed calibrations, where the sample is realigned between the calibrations. Signal noise contribu-

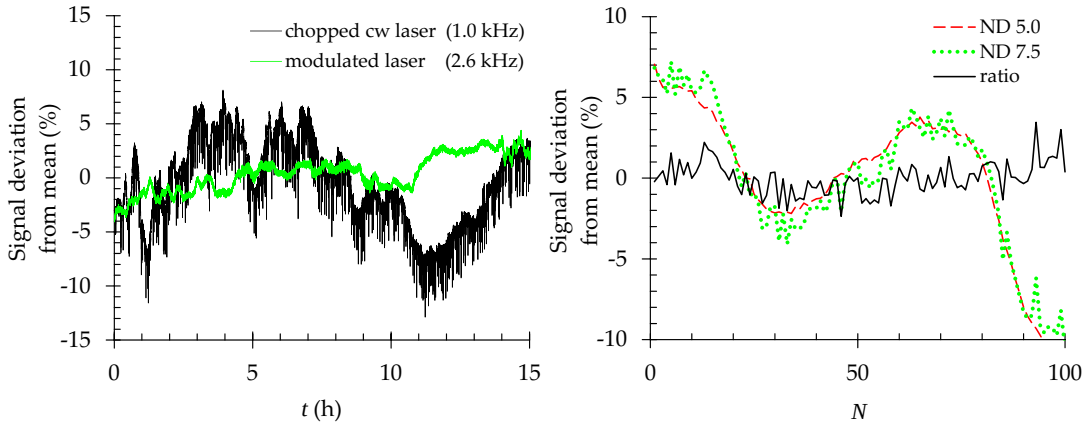

Figure 3.23: Signal drift (left) and attenuation (right) uncertainty.

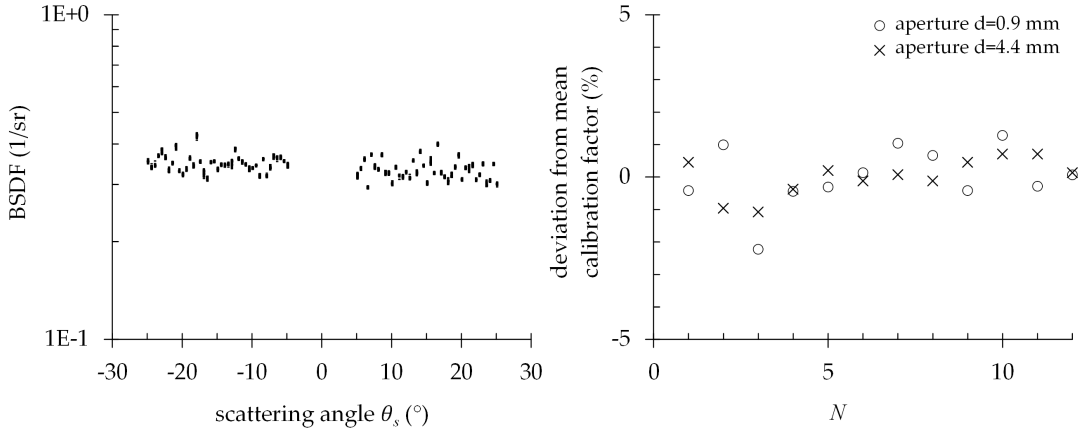

Figure 3.24: 40 repeated ARS measurements are superimposed to demonstrate the repeatability of the instrument (left). Relative normalization uncertainty (right).

tions are negligible, which was demonstrated by repeated calibrations of a Spectralon sample [132] without intermediate realignments (see Fig. 3.24, left). The derived uncertainty of signal noise on the calibration was found to be 0.09% (determined by 40 calibrations). As speckle effects increase for smaller apertures and smaller illumination wavelengths, $u_{det,r}(V_{det})/V_{det}$ grows with smaller apertures and smaller illumination wavelengths. The uncertainty was determined for 532 nm illumination, scattering angles between $5°<|\theta_s|<25°$ with 0.5° step sizes, 12 repetitions, and for two different apertures (see Fig. 3.24, right). The determined uncertainties are displayed in Table 3.2. Lower uncertainties are probably achievable by calibrating over a larger scattering angle regions or with a higher resolution.

Table 3.2: Determined uncertainties for the relative normalization.

aperture diameter	$u_{det,r}(V_{det})/V_{det}$
4.4 mm	0.58%
0.9 mm	0.96%

- External calibration $u_{ARS,cal}(ARS_{cal})/ARS_{cal}$

Uncertainty of the external calibration of the reference sample has to be obtained from the corresponding calibration laboratory. An external calibration laboratory specified $u_{ARS,cal}(ARS_{cal})/ARS_{cal}$=0.25% for a white Spectralon sample.

- System and sample misalignment $u_{det,align}(V_{det})/V_{det}$
  Misalignment of sample and system causes ARS uncertainty because (i) signal values are assigned to wrong scattering angles and (ii) the effective incident angle on the sample is changed which moreover changes the scattering distribution. This was previously not investigated by other authors. To be able to calculate these rather complex effects, a Monte Carlo simulation (MC) was performed[11]. Therefore, the shift-invariant character of the BRDF[12] [9] is exploited to calculate ARS changes caused by of misassigned V_{det} / θ_s values as well as deviations of θ_i.
  Monte Carlo simulation: The MC was realized using the commercial software Matlab [164]. System and user uncertainties can be entered in the input mask. The simulation is structured as follows:
  - Monte Carlo loop
    - Create random axes layout according to input uncertainties.
    - Align beam in axes layout according to system/user uncertainties.
    - Define $\theta_s \equiv 180°$ from beam coordinates.
    - Load ARS measurement data.
    - Generate random sample position / orientation near the instrument center.
    - If specular sample is aligned, simulate alignment procedure (see chapt. 3.4.2) according to user uncertainties.
    - Move positioners to the θ_s and θ_i coordinates according to the loaded ARS measurement with respect to positioner accuracies and current axes alignment.
      - Transform receiver aperture and incident beam positions into sample coordinates (polar and phi angles).
      - Calculate effective scattering geometry coordinates $\phi_{s,misaligned}$, $\theta_{s,misaligned}$ and $\theta_{i,misaligned}$ as a result of misalignment.
      - Calculate ARS changes for $\phi_{s,misaligned}$, $\theta_{s,misaligned}$ and $\theta_{i,misaligned}$ coordinates assuming shift invariant character .
    - If required show coordinate transformation, alignment procedure, or system setup plots.
  - Calculate standard deviations of the $ARS(\theta_s)$ from Monte Carlo simulations.

  The following instrument uncertainties and geometries were fed into the Monte-Carlo simulation:

[11] Monte-Carlo simulations are accepted as a GUM conform method [163].

[12] The validation of the shift invariance method to calculate OOP scattering behavior was recently conducted by measurements performed with the instrument developed in this work [107]. These investigations showed that although shift invariance is not applicable in a general term [107, 108], it works very well for small changes in θ_i - which is typically the case for misalignment effects. Moreover, it allows changes in the ARS to be calculated for a broad range of different samples (for small changes in θ_i), e.g. for surface scattering samples in different regimes of rms-roughness or for volume scattering samples.

- Detector sweep radius: 250 mm.
- θ_i/θ_s axes offset as a result of misalignment: $s_{\theta_i\theta_s xy}$=0.1 mm.
- θ_i/θ_s axes tilt as a result of misalignment: $s_{\theta_i\theta_s tilt}$= 0.05°.
- Incident beam alignment accuracy at detector positions of θ_s=0° and θ_s=180° (detector is used for beam alignment): 0.2 mm (lateral).
- Uncertainty of user to align the reflected beam of the sample into the detector aperture (used for sample alignment, see chapter 3.4.2): 0.2 mm (lateral).
- Scattering angles used for sample alignment: θ_{s1}=3°, θ_{s2}=60°.
- θ_i and θ_s positioner accuracy: s_θ= 0.01° ([13]).
- OOP angle: 0°.

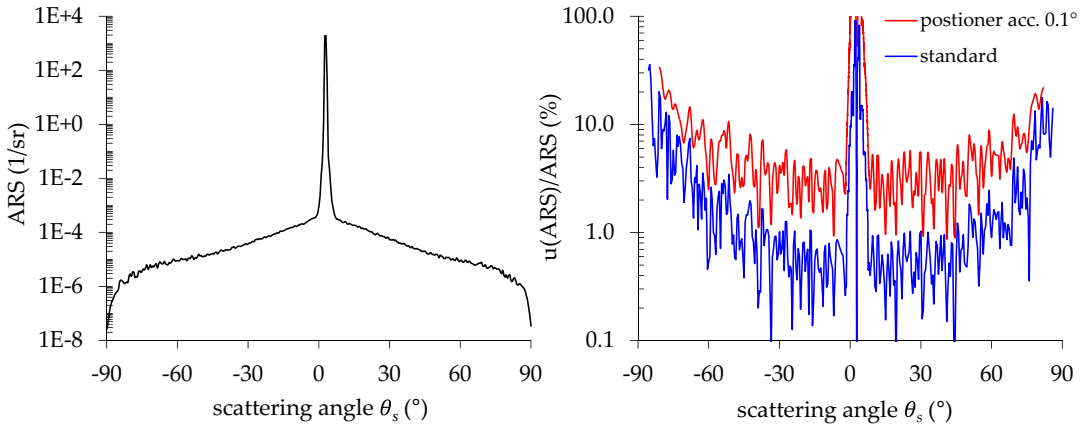

Figure 3.25: Measured ARS of a aluminum coated substrate (left) and the calculated uncertainty (right) for two different instrument set-ups.

The ARS uncertainty as a result of misalignment was simulated for a polished diamond turned Al substrate with a Ni top coating measured at θ_i=3° (see Fig. 3.25). The calculation is based on 1000 MC simulations. The obscuration resulting from the detector head at $\theta_s \approx$3° was cut out and interpolated.

The MC simulation showed that misalignment influences measurement uncertainty in particular in regions of θ_s where the slope of the ARS is very high. This is especially the case for the region around the specular beam (ARS uncertainties up to 100%) and the far scattering angles (ARS uncertainties up to 10%) while for scattering angles around 30° uncertainties of smaller than 1% can be expected. The fluctuations in the ARS uncertainty are caused by deviations of the slope in the ARS from speckle and signal noise.

Generally, the simulation showed that the front surface of a specular sample can be aligned into the center of the instrument (θ_s axis) with a standard deviation of 0.23 mm[14]. This is very accurate compared to the receiver arm length. As already

[13] The unidirectional positioning accuracies of the instrument described in this work (u(θ_s)<0.01° for k=2 and all axes) were determined by scanning the detector through the specular beam using a small aperture and small steps. The lateral deviations of the ARS where therefore assigned to deviations in θ_s.

[14] Schiff et al. [56] estimated a similar alignment uncertainty (0.2 mm) of the sample from the instrument center, though for other instrument geometries.

assumed, uncertainties of the solid angle can consequently be neglected. The standard deviation of θ_i was determined by the simulation with 0.11°.

Discussion: Although measurement uncertainty as a result of misalignment can be derived by the MC simulation, not much insight is gained into the contribution of individual parameters. This is in particular the case, as the misalignment uncertainty is a function of the ARS of the sample. To tackle this problem, the shift invariant approach used in the simulation is further analyzed in the following.
As a shift invariant sample scattering character is assumed, no ARS error is introduced by a misaligned system / sample as long as the spatial frequency (that corresponds to the ARS at a recorded scattering angle) is not affected. Hence, the deviation in the spatial frequency introduced by misalignment can be analyzed in the MC simulation to characterize misalignment uncertainty. This approach is especially interesting, as deviations in f are independent of the ARS of the sample. To moreover lose the function to λ, the deviation of the λ normalized spatial frequency is evaluated.

The normalized spatial frequencies γ that correspond to the misaligned system coordinates ($\theta_{s,misaligned}$, $\varphi_{s,misaligned}$, and $\theta_{i,misaligned}$) and the ideal (estimated) IP system coordinates (θ_s and θ_i) are calculated by

$$\begin{gathered}\gamma_{misaligned}(\theta_s) = \lambda \cdot f_{r,misaligned}(\theta_s) = \lambda \cdot g(\theta_{s,misaligned}, \varphi_{s,misaligned}, \theta_{i,misaligned}, \lambda) \ , \\ \gamma_{ideal}(\theta_s) = \lambda \cdot f(\theta_s) = \lambda \cdot g(\theta_s, \theta_i, \lambda) \ ,\end{gathered} \tag{3.39}$$

where g corresponds to the grating equation Eq. (2.14), where f_x and f_y are transformed to f_r by means of Eq. (2.11). In order to get a more descriptive expression than $\Delta\gamma(\theta_s)$ to characterize misalignment effects, misalignment is expressed as the deviation of the *relative* scattering angle from the ideal alignment:

$$\Delta\theta_s(\theta_s) = \arcsin(\gamma_{misaligned}) - \arcsin(\gamma_{ideal}) \ . \tag{3.40}$$

To characterize the effects of single parameters used in the MC, only single parameters are now varied to display changes in $\Delta\theta_s(\theta_s)$. The parameters of the MC that are based on the instruments specifications were defined as the standard setting.
Fig. 3.26 shows some results of the performed Monte Carlo simulations. Each calculation of the standard deviation of $\Delta\theta_s(\theta_s)$ is based on 1000 simulated systems, respectively. The calculations were performed up to about $|\theta_s|$<85°, as for some larger scattering angles the misalignment leads to not defined scattering angles in Eq. (3.40). Although some simulations did not lead to a relevant change in the overall misalignment uncertainty, their influence is possibly covered by effects of other parameters. However, MC simulations where only single parameters are assigned with uncertainties are not representative, because the parameters cannot be assumed as uncorrelated.
The upper left graph in Fig. 3.26 shows user related misalignment effects. Sample misalignment by a less experienced user was simulated by a lowered sample alignment accuracy of 0.4 mm. An increased incident beam misalignment was simulated by a reduced beam alignment accuracy of 0.5 mm. Increasing the misalignment of the θ_i/θ_s axes was simulated by a random offset and tilt of 2 mm ± 0.1 mm and 0° ± 0.8°, re-

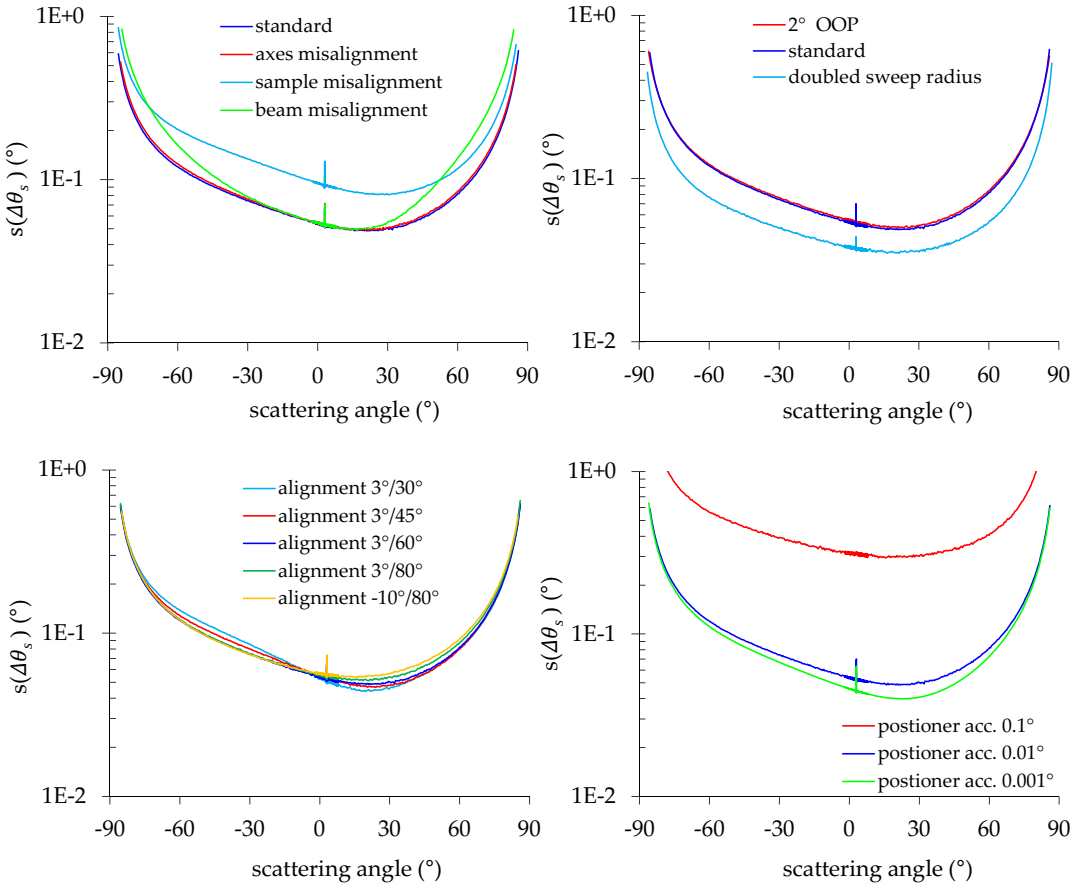

Figure 3.26: Calculated standard deviations of $\Delta\theta_s(\theta_s)$ to characterize misalignment effects: (from upper left to lower right) user related effects; system settings effects; sample alignment angles; positioner accuracy effects.

spectively. Unexpectedly, misaligned system axes only have a minor effect on the ARS uncertainty, as they are apparently well compensated by the standard sample alignment routine. A larger impact is observed for the users sample alignment accuracy, confirming the intuition of spending special effort on the sample alignment.
The upper right graph shows system settings effects. A 2° OOP angle has almost no effect on the ARS uncertainty, while a doubled detector arm length can significantly imporove sample alignment.

The lower left graph reveals only small uncertainty effects for the choice of the scattering angles used to align the sample. Alignment angles of θ_s=3°/60° seem to be a good compromise for a well aligned sample.

The lower right graph shows that improving the positioner accuracies beyond 0.01° will not result in much better performance. However, positioning accuracies for the θ_i and θ_s axes of 0.1°, which are sometimes found in the specifications of scatterometers, lead to high measurement uncertainties and are consequently not recommended (see Fig. 3.25, right).

Optimization: In particular the high slopes in the ARS close to the specular beam of polished samples cause small deviations in the spatial frequency (corresponds to $\Delta\theta_s \approx 0.05°$ at the specular beam) to affect relatively high ARS uncertainties. How-

ever, as only deviations in the spatial frequencies cause uncertainties, alignment offsets can be used to shift the "zero" spatial frequency of the instrument coordinates onto the specular beam.

For reflective samples, this can be done by moving the positioners to $\theta_i = \theta_s$ with the sample aligned in the sample holder. The coordinate offset is now introduced by either (i) readjusting the detector aperture position, (ii) readjusting the sample tilt, or (iii) readjusting the alignment of the incident beam - such that the beam enters the detector aperture at $\theta_i = \theta_s$. This can be e.g. done by using a small detector aperture and recording the signal while the readjustment is (automatically) performed. As the profile of the beam is known (e.g. Gaussian profile), very high accuracies can be achieved to calculate the position of the reflected beam. The detector aperture is accordingly moved to the center of the specular beam, and the coordinates are defined as $\theta_i = \theta_s$. This coordinate offset may causes an increase in $\Delta\theta_s(\theta_s)$ at large scattering angles, but should significantly reduce $\Delta\theta_s(\theta_s)$ in the near specular region.

A lateral (automated) readjustment of the detector aperture in two orthogonal directions can be realized by implementing only one additional vertical positioner (see Fig. 3.27, left). The necessary second degree of freedom is provided by the θ_s positioner.

The procedure was simulated in the MC simulation by readjusting the lateral position of the detector aperture after the sample was aligned. The positioning uncertainty of the readjustment was in both directions assumed to be equal to the θ_s positioner uncertainty. Fig. 3.27 (inset upper right) shows that the automated readjustment routine reduces $\Delta\theta_s(\theta_s)$ in particular near the specular beam. The simulation showed that a significant improvement of the relative ARS uncertainty down to about 20% (close to the specular beam) can be expected (see Fig. 3.27).

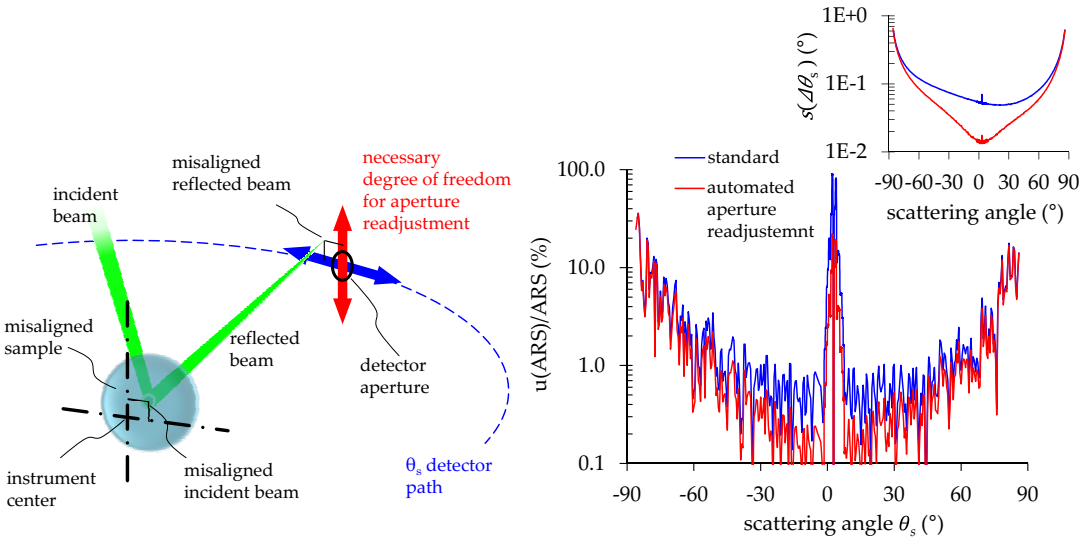

Figure 3.27: Left: Possible improvement of the measurement uncertainties caused by misalignment by means of an automated readjustment of the detector aperture in two lateral degrees of freedom. Right: Expected effect on the measurement uncertainty (center) and $\Delta\theta_s(\theta_s)$ (inset diagram).

Combined measurement uncertainty

The combined measurement uncertainty of the ARS of the aluminum coated substrate is calculated with Matlab [164] according to Eq. (3.35). As the measurement was performed shortly after calibration, signal drift uncertainty can be neglected. The relative uncertainties are summarized in Fig. 3.28 left, the individual contributions (Fig. 3.28, right) are calculated by normalizing to the total uncertainty.

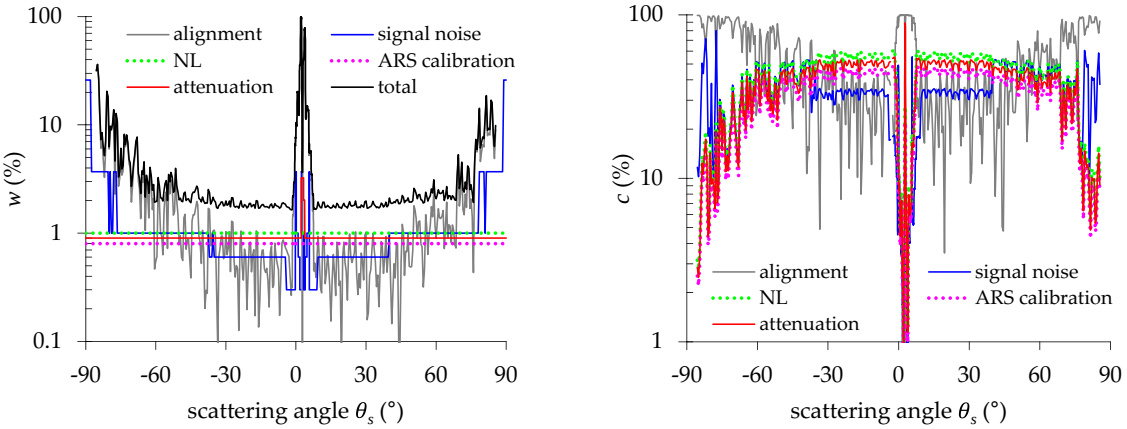

Figure 3.28: Left: the combined measurement uncertainty. Right: contributions.

For the largest region, the combined measurement uncertainty (k=2) is about 2% where attenuation, non-linearity, and calibration contribute about the same amount. This is a very good result, as experience shows that sample homogeneity deviations mostly have a much higher influence. At large scattering angles and around the specular beam the combined measurement uncertainty is dominated by alignment and rises up to 20% and almost 100%, respectively. However, as the specular beam in the ARS is for most samples dominated by the beam profile of the instrument's signature, uncertainty is here mostly irrelevant. At the peak of the specular beam, where the ARS slope is about zero, measurement uncertainty drops to about 4% which is dominated by attenuation uncertainties. However, this part of the ARS is only interesting for the calculation of reflectivity coefficients. A good practice to eliminate attenuation uncertainties for reflectivity coefficient measures is to leave the filters in a fixed position between the total power calibration and the actual measurement.

Discussion

What has to be considered as a reliable measurement uncertainty for a light scattering instrument?

The derived measurement uncertainty values in this chapter vary between 2% and even 20% in the non-specular regions and may seem high compared to other measurement techniques (e.g. a length measurement uncertainty of 20% may seems rather intolerable). Though, compared to the extremely large dynamic range of ARS distributions those uncertainty values can actually be considered as being very accurate, which is demonstrated in this section by a simple example.

Fig. 3.29 shows the ARS measurement of a commercially acquired high reflective (HR) coating designed for 620 nm to 0 nm on a fused silica substrate. The coating consist of a magnetron sputtered Ta_2O_5/SiO_2 quater-wave multilayer stack, and the ARS was measured in backward and forward scattering direction, with θ_i=0°, and a small OOP angle of 3° to capture the specular reflected beam.

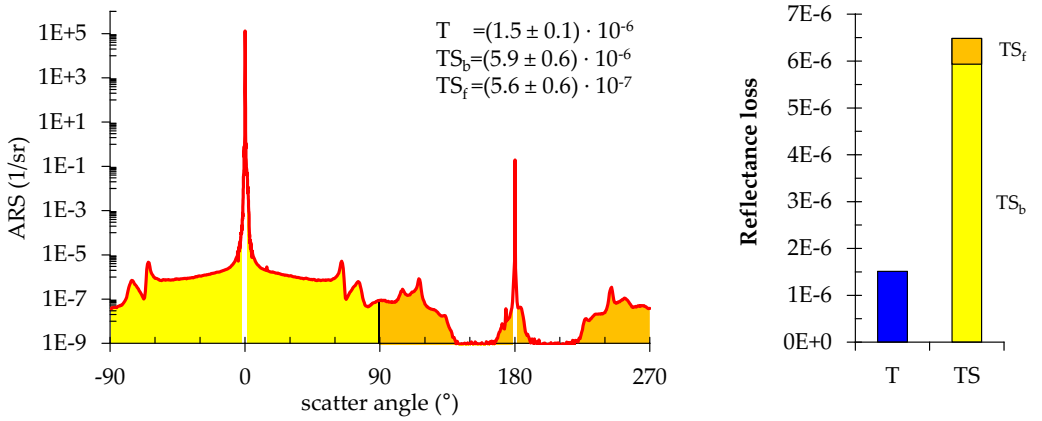

Figure 3.29: Left: ARS analysis of a high reflective Ta_2O_5/SiO_2 coating designed for 640 nm to 680 nm on a fused silica substrate. Right: the total scatter losses were determined by integration, the residual transmittance is measured by scanning the specular transmitted beam.

The ARS exhibits pronounced wings originating from interference effects of the scattered light in the multilayer coating. The reflectance of the coating was measured with the instrument to 99.6%±4%, which can be considered as a high *absolute* measurement uncertainty with respect to alternative reflectance measurement techniques (e.g. cavity ring-down).
Though, as the *relative* uncertainties of ARS measurements are in the same OOM, comparably low absolute uncertainties are achievable: The reflectance of the mirror can be alternatively calculated by

$$R + A = 1 - T - TS_b - TS_f\,. \tag{3.41}$$

TS_b and TS_f are calculated from the ARS measurement and are, for reasons of simplicity, assumed with uncertainties of 10% [15] which yields T=(1.5±0.1) · 10^{-6}, TS_b=(5.9±0.6) · 10^{-6}, and TS_f=(5.6±0.6) · 10^{-7}. $R+A$ calculates to (99.99920±0.00007)%, which represents a very accurate measurement[16].

Off-topic remarks: Compared to cavity ring-down reflectance measurements, the individual loss contributions can be separated, so that the total reflectance loss of 8.0 · 10^{-6} consists of 81% scatter losses and only 19% losses resulting from specularly transmitted power (see Fig. 3.29, right). Adding more layers would consequently not be a fruitful approach for optimization. Further investigation into the origin of the scatter losses (layer thickness deviations, roughness evolution, or volume scattering inside the layers) and an accordingly deducible

[15] All total scatter losses were calculated by integrating the ARS between 2° and 85° from specular according to ISO13696 [ISO13696]. The scatter loss in forward direction represents a worst case estimation, where the noise floor at 1 · 10^{-9}sr-1 was not subtracted. Also, the NEARS level between 15° and 40° around the specular transmitted beam was included in the integration. Subtracting noise floor and setting this region to zero results in a best case estimation resulting in only a marginal deviation with TS_f=(5.57±0.56) · 10^{-7}.

[16] The combined (absolute) sub ppm uncertainty is achievable as the single contributions are also tolerated with (absolute) sub ppm uncertainties.

optimization, is only possible by knowing the detailed multilayer design, which was not the case for this sample.

Summary

This chapter introduced a comprehensive uncertainty analysis for the light scatterometer described in this work. The ARS uncertainty analysis of this work is based on the relative normalization method and consequently allows traceability to a national or international standard (requested for ISO17025 [37]). Effects like sample and system misalignment were newly introduced and studied based on a Monte-Carlo simulation. The uncertainty analysis developed in this chapter allows to systematically optimize measurement uncertainty of the table top instrument, as it gives a lot of insight into single contributions.
Hence, next suggested optimization steps derived from the uncertainty analysis are the implementation of an automatic routine, which precisely locates the specular beam after alignment and introduces a corresponding coordinate offset (automated aperture readjustment onto the specular beam). As has been shown in this chapter, this would allow a significant improvement of misalignment effects. Furthermore, the overall measurement uncertainty can be dominated by signal drifts errors where the combined uncertainty is otherwise about 2% (k=2). Hence, a signal monitor to record laser drifts or a more stable laser can further improve the instruments uncertainty budget. A further improvement of the attenuation repeatability is helpful to reduce uncertainty for reflectivity measurements. However, it is not mandatory as an effective workaround exits.

3.6.4 Optimization

Based on the investigations made to characterize the instrument performance in this chapter, a further optimization was conducted. This applies particularly to the following specifications:

- Near angle signature improvement by optimizing individual optical elements (see chapter 3.6.1).
- Integration of two additional laser sources (405 nm and 640 nm laser diode).
- Far angle signature improvement by reduction of environmental cleanliness.
- Reduction of measurement uncertainty (see chapter 3.6.3) by direct light source modulation instead of using a miniature chopper.

Near angle signature

As already pointed out in chapter 3.6.1, an optimization of the light scattering from the system optics can, at first, only be performed by replacing M2 and M3 of the illumination system. To reduce aberrations, M1 could also be replaced by a state-of-the-art aspherical surface (see chapter 3.3.2). The PSDs of alternative optical elements are plotted in Fig. 3.30 along with the currently used mirrors [152].

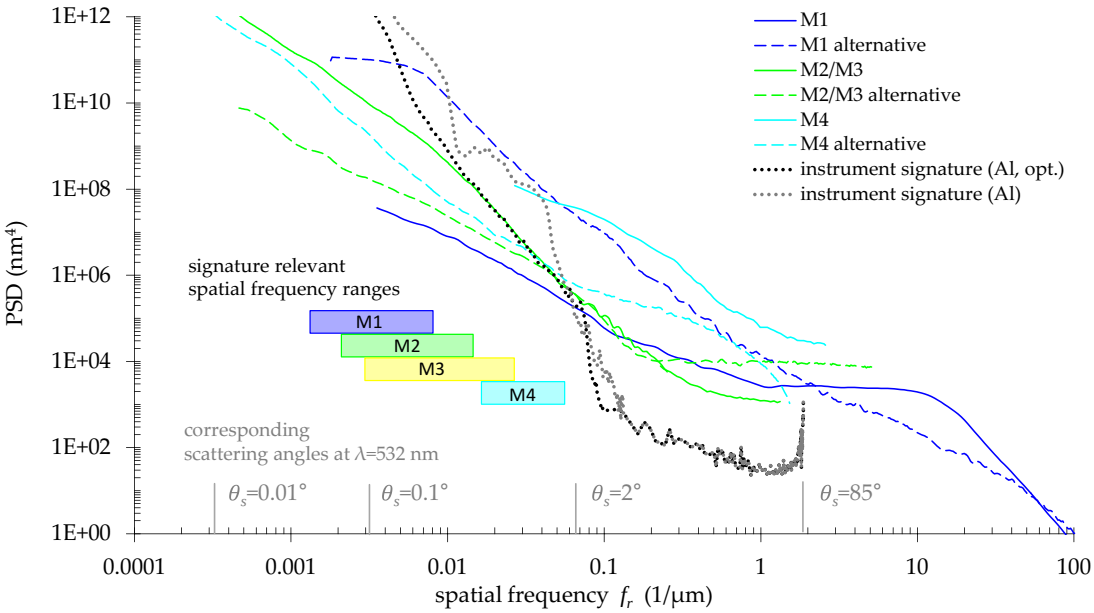

Figure 3.30: PSDs of the used optical elements along with alternative mirrors.

The aspherical surface (uncoated substrate, M1 alternative) exhibits a more than two OOMs higher PSD within the relevant spatial frequency band than the currently used spherical surface. Although the PSDs of the currently used mirrors M2 and M3 are higher at larger spatial frequencies (large scattering angles) than their alternative replacement, the PSD in the relevant spatial frequency range is more than one OOM lower. M4 could be optimized by more than one OOM, though the impact is rather marginal. Consequently, only M2 and M3 will be replaced by their alternative option. The achieved near angle signature optimization is shown in figure 3.31. The measurement fits the predicted near angle signature calculated from the PSD data very well.

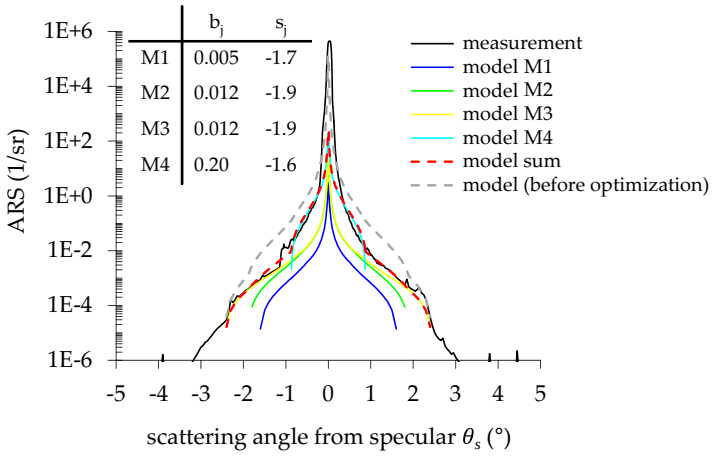

Figure 3.31: Optimized near angle signature.

The optimized signature is about one OOM lower than before (it is also broader because the illumination spot size was d_{ill}=4 mm instead of d_{ill}=1.5 mm as in chapter 3.6.1). The optimization gains about half an order of magnitude in spatial frequency in the PSD for standard quality mirrors (e.g. compare the PSD signatures for aluminum to the PSD of M4 in Fig. 3.30).

Now as all optics contribute about the same ARS level, a further optimization is consequently only possible if all components are improved.

Far angle signature

Fig. 3.32 shows the far angle signature of the instrument after the implementation of the two additional laser sources (see also chapt. 3.5). Obviously, they all show a Rayleigh limited performance with good agreement to theory (Eq. (3.19)). Moreover, the instrument is now operated inside a laminar flow box which visibly reduces fluctuations in the transmission hemisphere and clearly demonstrates the influence of the environment cleanliness.

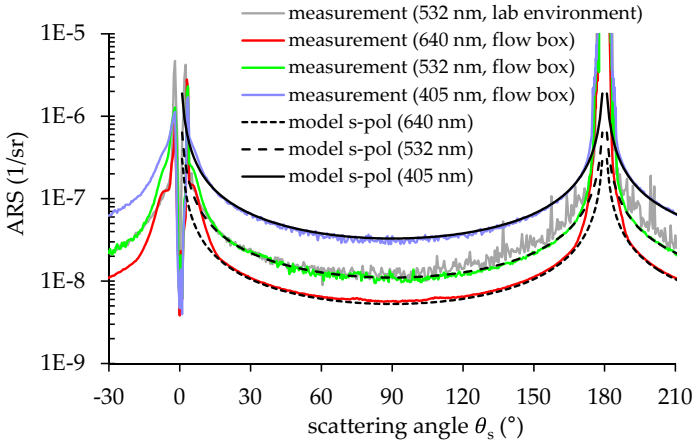

Figure 3.32: Optimized far angle signature with three implemented laser sources in a laminar flow box.

Measurement uncertainty

As 3D-ARS measurements can easily take 12 or more hours, the overall measurement uncertainty can be dominated by signal drifts. Therefore, only a better laser or a signal monitor can further improve the instruments uncertainty budget. Fig. 3.33 shows the long term stability measurement of an alternative Nd:Yag laser (532 nm, red line). Its power output can also be directly modulated like the currently used laser. The new laser shows a signiicant improved long term stability with a standard deviation of $s_{det,drift}(V_{det})/V_{det}$ =0.3%, while laser 1 (black line) and laser 2 (green line) performed with $s_{det,drift}(V_{det})/V_{det}$ =3.8% and 2.4%, respectively. This allows a further measurement uncertainty optimization without the need for an additional signal monitor.

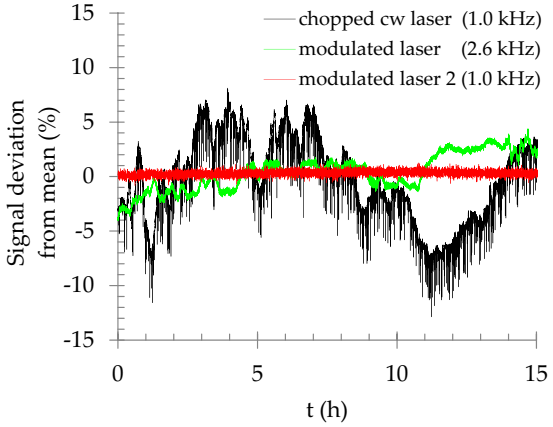

Figure 3.33: Long term stability optimization.

4 Examples of application

4.1 Anisotropy analysis of ultra-precision diamond turned surfaces

Compared to topographic metrology like WLI or AFM, light scattering analysis benefits from the much larger measuring field (several mm^2 vs. several μm^2) covering more samples per spatial frequency, and, accordingly yielding a lower PSD noise. While for topographically measured isotropic surfaces this noise can be effectively reduced by azimuthal averaging of the 2D-PSD [16, 39] (see Eq. 2.10), anisotropic surfaces demand averaging over multiple measurement positions - which is not necessary for light scattering techniques.
Hence, assessment of ultra-precision diamond turned (UP) surfaces by ARS analysis was already of special interest since the middle 70s [6, 8, 92, 165–168]. In these publications, four contributing roughness components were identified, yet those four components were not listed together completely in previous publications:

1. "turning marks" or "tool marks" [6, 8, 92, 165–168]
   (1D, perpendicular to turning marks, function of feed rate and tool tip shape [92])
2. "random roughness" of the turning marks[1] [8, 92, 165–167]
   (1D, perpendicular to turning marks, result of chip drag and tool jitter [8, 167])
3. "chatter marks" or "jitter" [168]
   (2D, along turning marks, result of tool jitter [168])
4. isotropic background [8, 92, 165–168]
   (2D-isotropic, result of material intrinsic grain boundaries [92])

The validity of theses assumptions will be discussed later in this chapter. Church et. al. proposed to separate the ARS of the individual roughness contributions by sequential subtraction and calculated PSDs and rms roughness values for the roughness types 1, 2, and 4 [92]. They observed that typically the random roughness of the turning marks dominates the other contributions. However, post measurement analysis was significantly restricted by the absence of 3D-ARS measurements, and only the contributions to the rms-roughness were analyzed. Later publications with 3D-ARS measurements analyzed also rms roughness contributions [169, 170].

Amra et. al. [18] introduced an isotropy factor based on a spatial frequency resolving azimuthal autocorrelation function of the ARS to characterize anisotropic surfaces in general. He showed, that the degree of anisotropy is a function of the spatial frequency, however, the introduced anisotropy factor is not intuitively related to optical performance or roughness

[1] The term was introduced by Church [92] and related to the "random" speckle-like fine structure it creates in light scattering analysis, though its coarse shape (the ensemble average) still bears information. These fine random fluctuations were consequently averaged by a detector aperture that was large compared to the speckle size - "to see the forest instead of the trees".

properties of the sample. Herffurth et. al. [77] calculated the directional rms roughness from ARS measurements and introduced an anisotropy factor based on the azimuthal rms deviation of the rms roughness.

In the following subchapters, all four roughness contributions of diamond-turned surfaces are analyzed on a small set of samples. Rather than analyzing the contributions by 1D and 2D-iso PSDs calculated from sectional ARS measurements [6, 8, 92, 167], the analysis is performed by means of 2D-PSDs derived from hemispherical 3D-ARS measurements. As surfaces can perform surprisingly different in different regions of spatial frequency (or scattering angle), the proposed contribution analysis to the rms roughness and TS will be a function of f. This grants access to more detailed information on the optical performance and allows a more directed surface optimization. It will be shown that this method is suitable to characterize anisotropy in general and also provides a new isotropy factor. The factor will be utilized to predict optical performance as a function of the application wavelength.

4.1.1 Description of the method

The method proposed in the following is interchangeably applicable to 2D-PSD and 3D-ARS data if the smooth surface approximation is valid (linear relationship between ARS and PSD). However, as the method is used to discriminate roughness components, it is exemplarily described to handle PSD data. In the following 2D-PSDs are denoted by the index "2D" (correspond to 3D-ARS), whereas 2D-isotropic PSDs are missing that index (correspond to IP-ARS for isotropic samples).

To separate the 2D-PSDs of the individual roughness components, the isotropic background $\mathrm{PS}D_{isoBG,2D}(f_r)$ has to be subtracted from the surfaces $\mathrm{PS}D_{2D}(f_r, \phi_r)$ [92]. The isotropic background can be extracted from the $\mathrm{PS}D_{2D}(f_r, \phi)$ by searching for minimum values in ϕ for constant values of f_r. This yields a more accurate $\mathrm{PS}D_{isoBG,2D}(f_r)$ than the published approaches where a PSD section at a fixed azimuth angle of ϕ=45° or ϕ=90° from the turning marks was defined as the isotropic background. Especially the PSD section at ϕ=90° may be superimposed by other roughness contributions (e.g. chatter or defects). To calculate the $\mathrm{PS}D_{isoBG,2D}(f_r)$ an iterative data reduction algorithm is used to achieve a higher insensitivity to noise, rather than simply picking minimum values. Therefore, the highest values from a data set with the spatial frequency f_r are removed until a given threshold in the standard deviation of the data set is reached. The data reduction algorithm is comparable to the one reviewed in ISO13696 [38][2].
Turning and chatter marks are proposed to be discriminated by a spatial frequency selection in the regions A_{tm} and A_{cm} of $\mathrm{PS}D_{2D}(f_r, \phi_r)$-$\mathrm{PS}D_{isoBG,2D}(f_r)$, where A_{tm} is accordingly chosen rectangular along the turning marks with a small width and A_{cm} covers the residual region of $\mathrm{PS}D_{2D}(f_r, \phi_r)$, respectively. Hence, the relative contributions of turning marks $a_{tm}(f_r)$, chatter marks $a_{cm}(f_r)$, and isotropic background $a_{iso}(f_r)$ to the 2D-isotropic PSD(f_r) can be calculated by relating their PSD functions to the surfaces PSD:

[2] In ISO13696 a single representative TS value is extracted from multiple TS values of different sample positions.

$$a_{tm}(f_r) = \frac{\oint_{A_{tm}} \left(PSD_{2D}(f_r,\phi) - PSD_{isoBG,2D}(f_r,\phi)\right) d\phi}{\int_{2\pi} PSD_{2D}(f_r,\phi) d\phi} \ , \tag{4.1}$$

$$a_{iso}(f_r) = \frac{\int_{2\pi} PSD_{isoBG,2D}(f_r,\phi) d\phi}{\int_{2\pi} PSD_{2D}(f_r,\phi) d\phi} \ , \tag{4.2}$$

where $a_{cm}(f_r)$ is calculated according to Eq. (4.1). It is obvious that the contribution factors are identical (for optically smooth surfaces) when calculated from ARS or PSD data, because of the linear relation of the PSD and the ARS. Please note that the integrals with the subtractions allow negative values to average out statistical fluctuations.

The absolute contributions that sum up to the surfaces 2D-isotropic representative PSD(f_r) are calculated by

$$PSD_{tm}(f_r) = a_{tm}(f_r) PSD(f_r) \ , \tag{4.3}$$

where $PSD_{cm}(f_r)$ is calculated accordingly.

The random roughness component in $PSD_{tm}(f_r)$ is extracted by a spatial frequency selective discrimination in f_r around the peaks, which is interpolated and subtracted from $PSD_{tm}(f_r)$ to yield the roughness of the profile. However, as the two components are visually easy to separate in the $PSD_{tm}(f_r)$ and in $a_{tm}(f_r)$, in the following chapter this is only performed to calculate the contribution to σ.

Different roughness components i with the rms roughness σ_i sum up to the overall roughness σ by adding their variances [92]:

$$\sigma^2 = \sum_i \sigma_i^2 \ . \tag{4.4}$$

Hence, the contributions $\bar{a_i}$ to the rms roughness have to be calculated by relating the variance values (instead of relating their rms roughness values)

$$\overline{a}_i = \sigma_i^2 / \sigma^2 \ . \tag{4.5}$$

Accordingly, the PSDs are integrated within f_{min} and f_{max} to yield variance; the contribution to the integrated scattering S_b within θ_{min} and θ_{max} are analogously calculated by normalizing to S_b:

$$\overline{a}_{tm} = \frac{\int_{f_{min}}^{f_{max}} a_{tm}(f_r) \cdot \mathrm{PSD}(f_r) \cdot f_r \cdot df_r}{\int_{f_{min}}^{f_{max}} \mathrm{PSD}(f_r) \cdot f_r \cdot df_r} \ , \tag{4.6}$$

$$\overline{a}_{tm} = \frac{\int_{\theta_{min}}^{\theta_{max}} a_{tm}(\theta_s) \cdot \mathrm{ARS}(\theta_s) \cdot \sin(\theta_s) \cdot d\theta_s}{\int_{\theta_{min}}^{\theta_{max}} \mathrm{ARS}(\theta_s) \cdot \sin(\theta_s) \cdot d\theta_s} \ . \tag{4.7}$$

The factors $\overline{a}_{cm}$ and $\overline{a}_{isoBG}$ are determined accordingly. Please note that the values of the contribution factors are identical for Eq. (4.6) and Eq. (4.7) (rather than a squared relationship as between σ and TS_b, see Eq. (2.16)), because the root in the calculation of the

rms roughness from the PSD (Eq. (2.12)) is canceled by Eq. (4.5).
The isotropic background does not necessarily represent a roughness component in all regions of f_r as it can be altered by other roughness components. Though, it is always a roughness representing factor describing the overall degree of isotropy: If the integration limits of $\overline{a}_{iso}$ are chosen to θ_{min}=2° and θ_{max}=85°, the factor describes the optically relevant degree of isotropy of the sample, where $(1\text{-}\overline{a}_{iso}) \cdot TS_b$ is a measure for the amount of light that is scattered anisotropically.
This allows one to calculate the degree of isotropy as a function of the illumination wavelength $\overline{a}_{iso}(\lambda)$ if the integration limits in Eq. (4.6) are chosen accordingly.

The advantage of these introduced contribution factors becomes evident as they have a simple connection to both the optically relevant roughness and the scattering relevant properties. In addition, the method can be used to discriminate between different roughness contributions according to their optical effect.

4.1.2 Application

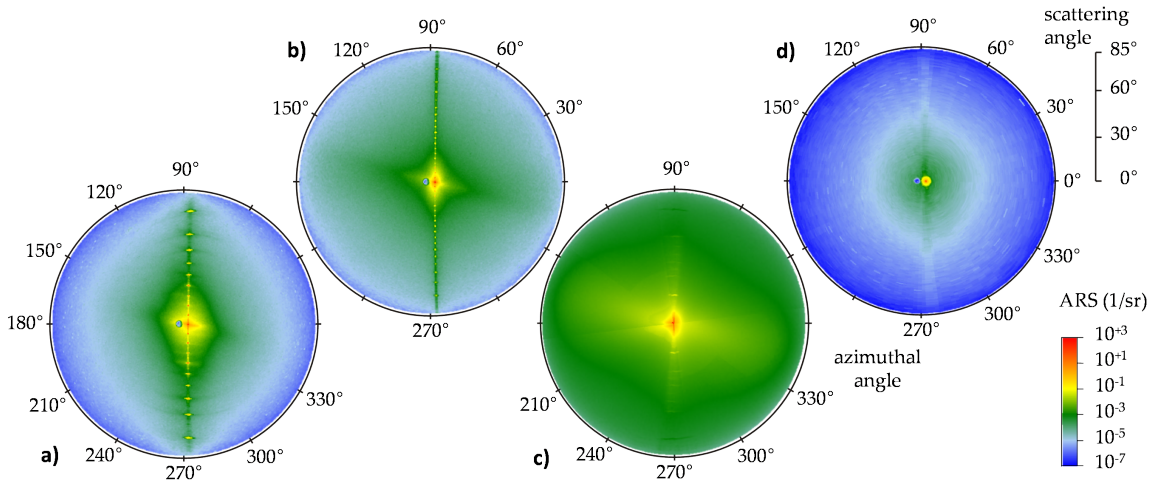

Figure 4.1: 3D-ARS measurements at λ=532 nm in the reflection hemisphere of four different UP diamond turned surfaces. Sample d) is polished after being diamond turned.

Figure 4.1 displays 3D-ARS measurements of four different UP diamond turned surfaces[3]. All measurements were performed in the reflection hemisphere at λ=532 nm and with circularly polarized illumination. Surfaces a), b) and d) were processed on aluminum with nickle top coating. Surface d) was subsequently polished [171] and surface c) was diamond turned on bare aluminum [172]. Surfaces a) and b) were fabricated on one single mirror substrate with different process parameters.
The ARS measurements were performed within the reflection hemisphere at an angle of incidence of θ_i=3° (instead of normal incidence), which shifts the detector obscuration to less interesting and redundant regions (instead of vignetting near angle scattering and the specular beam).

The 3D-ARS measurements of surfaces a) to c) reveal pronounced anisotropic light scattering

[3]The surfaces described in this chapter do not necessarily represent the state of the art in this fast developing field.

distributions which can be qualitatively subdivided into the four roughness components and a defect:

- The clearly visible peaks are a result from diffraction at the *turning marks profile* acting as a low efficiency grating.
- The increased ARS level between the peaks corresponds to the *random roughness* of the turning marks.
- At an azimuth angle of about 170°, light scattering from the *chatter marks* can be observed.
- Except for surface d), the remaining *isotropic background* is extensively covered by the previously described roughness components. For surface d), chatter and turning marks were completely removed by the polishing process. The residual roughness structures are isotropic.
- The small superimposed anisotropy on sample d) is probably related to a *defect*, as other sample positions either had no superimposed anisotropy, or its orientation was not perpendicular to the turning mark orientation.

Roughness analysis

Fig. 4.2 (top) displays 2D-isotropic PSDs and the directional rms roughness of sample a) that were calculated from topography and 3D-ARS measurements, respectively. Therefore, the originally calculated 2D-PSDs were azimuthally averaged and radially integrated. Both plots show a good agreement with the derived rms roughness values of 10.4 nm and 11.2 nm (within the spatial frequency range $0.022\,\mu m^{-1} < f_r < 1.94\,\mu m^{-1}$) for ARS and topography data, respectively. Hence, the 2D-PSDs of highly anisotropic diamond turned surfaces agree in both azimuthal and radial direction, which validates the analysis.

Fig. 4.2 (bottom) shows the corresponding 2D-PSDs for the topography ($PSD_{2D,topo}$) and ARS data ($PSD_{2D,ARS}$), which are fundamental to the previous calculations. Therefore, the 2D-PSD of a 94x95 µm² WLI and a 50x50 µm AFM scan were combined to a 2D-master PSD to cover the same spatial frequency range as the ARS measurement, which was also combined from a hemispherical scan and a near angle measurement with higher resolution and smaller aperture (shown in Fig. 4.8 right).

While the average of the logarithmic deviation $\log(PSD_{2D,ARS}) - \log(PSD_{2D,topo})$ equals 0.05 OOM, which represents a very good agreement, its standard deviation was calculated to comparably high 0.55 OOM. The highest deviations occur at the intersections of the topographic data between WLI and AFM data as well as at the artificial lines in the AFM measurement. The AFM artifacts can be explained by the line-by-line subtraction of a polynomial fit in the fast scan axis [173, 174], as the characteristic lines in the 2D-PSD were perpendicular to the fast scan axis. Interestingly, the 2D-PSDs agree between the lines, which supports the assumption that these lines are artificial and do not represent the microtopgraphy. Furthermore, statistical fluctuations are visible, especially in the PSD calculated from AFM and from the near angle 3D-ARS.

Overall, the 2D-PSD from the ARS is significantly less noisy (at f_r>0.1, resulting from the larger measurement field) and less artificially distorted. The procedure to analyze anisotropy,

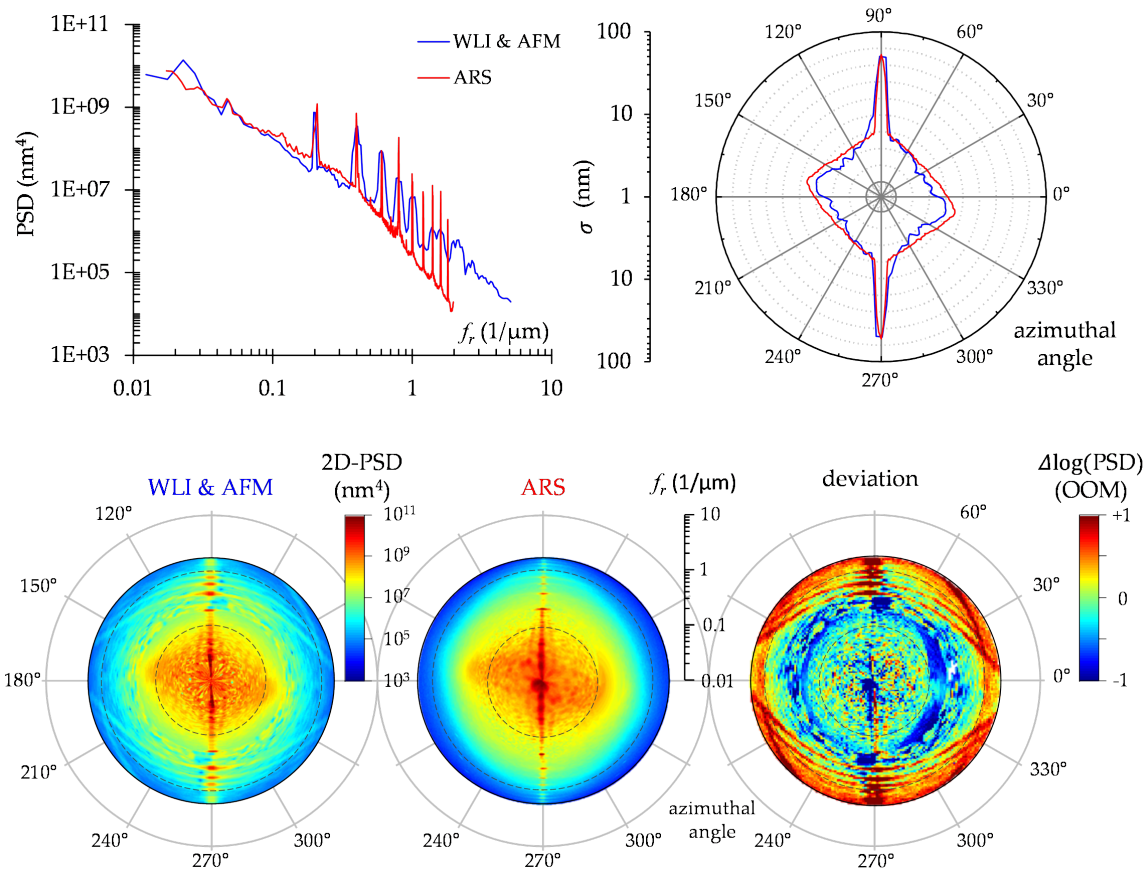

Figure 4.2: Roughness analysis of surface a): 2D-PSD functions calculated from ARS and topography data (bottom). Comparison of the azimuthally averaged (top left) and radially integrated (top right) 2D-PSD functions yields the 2D-iso-PSDs and the directional rms-roughness of the topography and the ARS data, respectively. 2D-PSD functions calculated from topography (bottom left), 3D-ARS (bottom center), and their deviation (bottom right).

which was introduced in the previous section, is consequently beneficially performed by ARS measurements.

In order to compare the anisotropy of the surfaces a) to d), the directional rms-roughness calculated from 3D-ARS were normalized by the isotropic rms roughness (Fig. 4.3). The azimuthal relative rms deviations were calculated to 0.74, 0.55, 0.24, and 0.07 for surface a) to d), with rms-roughness values of 8.8 nm, 6.0 nm, 10.5 nm, and 0.56 nm, respectively (within spatial frequency ranges from 0.06 µm^{-1} to 1.77 µm^{-1} for surface a) to c) and 0.10 µm^{-1} and 1.77 µm^{-1} for surface d).

In both the 2D-isotropic PSD and the directional rms roughness plots the information of the four roughness contributions is superimposed. A more detailed analysis based on the more general 2D-PSDs and the method described in chapter 4.1.1 is presented in the following.

Roughness contribution analysis

The contribution factors of the individual roughness components introduced in chapter 4.1.1 (Eq. (4.1) and (4.2)) are calculated. In Fig. 4.4, sectional views of the calculated 2D-PSD(f_r, ϕ)s from the different diamond turned samples a) to d) are plotted along with the

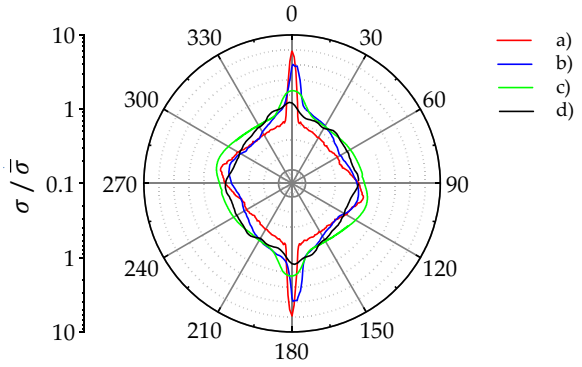

Figure 4.3: Comparison of the normalized directional rms-roughness values for surface a) to d).

contribution factors and WLI scans. As a summary, the absolute contributions to the squared rms-roughness (variance) are plotted in Fig. 4.5 along with the relative contributions (Eq. 4.6) denoted in percentiles. The following conclusions can be deduced:

General*:* Certainly, the overall isotropy changes with spatial frequency as previously conceived [18], or more general, the individual roughness components (2D-isotropic, 2D-anisotropic, and 1D) have a pronounced and characteristic dependency on the spatial frequency, which eventually affects the frequency dependent nature of the overall isotropy. This affects different roughness components to dominate in different regions of f_r or θ_s. Accordingly, an application oriented process optimization would aim at either shifting the individual roughness contributions to scattering angles of less interest, or at reducing the *dominating* roughness component in the application's range of f_r, rather than just reducing σ without respect to the application bandwidth.

Isotropy*:* As the 2D-isotropic PSD of the isotropic background visibly changes for surface a) and b) (fabricated on the same mirror), the calcultated isotropic background can - not surprisingly - be optimized by changing process parameters. It does consequently not represent a pure material intrinsic parameter. It will be shown in the next section that chatter - which should be potentially one-dimensional and only perpendicular to the turning marks - is spread to a 2D-PSD that is consequently able to completely superimpose the 2D-isotropic background.
This assumption is supported in the contribution plots for surface a) and b), where the isotropic background $a_{iso}(f_r)$ and the chatter marks $a_{cm}(f_r)$ seem to correlate in some regions of f_r - while in these regions of spatial frequency the chatter shows higher maximum values than the isotropic background (see sectional 2D-PSDs). Contrary, surface c) shows no correlation between the contribution of chatter and isotropic background, which imposes the assumption, that the isotropic background is influenced by isotropic structures rather than being superimposed by chatter. This is confirmed in the WLI scans, where sample c) shows small distinct bumps
The sole isotropic part in this highly anisotropic manufacturing process is the granular material structure, a possible post manufacturing cleaning process, or a coating. For UP surfaces, the isotropic background is consequently majorly influenced by chatter and should therefore

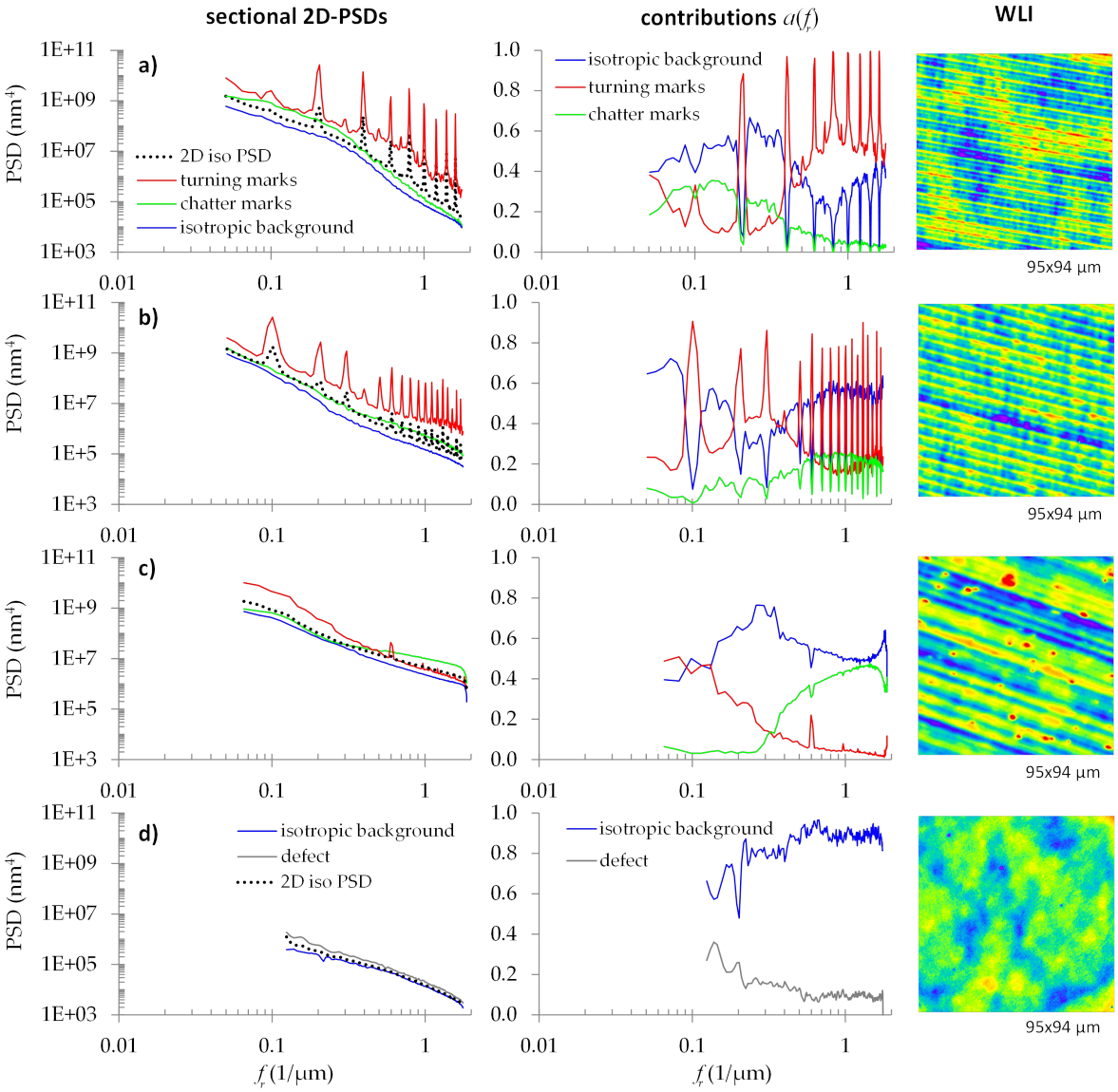

Figure 4.4: Discrimination of turning marks, chatter marks and isotropic underground. Left graphs: sectional views of the calculated PSD(f_r, ϕ)s from the different diamond turned samples a) to d). Center graphs: contributions to ARS or PSD as a function of spatial frequency. Right: WLI measurements.

be at least associated with the chatter contribution as long as it is not clearly separable.
The isotropic background represents the roughness equivalent degree of isotropy and has a major contribution to σ for all surfaces (see Fig. 4.5). As expected, the polished surface d) shows the highest degree of isotropy ($\overline{a}_{iso}(\lambda = 532\,\text{nm})$=85%), followed by surface c) ($\overline{a}_{iso}(\lambda = 532\,\text{nm})$=54%), while surface a) and b) perform about the same ($\overline{a}_{iso}(\lambda = 532\,\text{nm})$=34% and 37%, respectively).

Contributions: At the discrete spatial frequencies of the peaks, the profile of the turning marks is the dominating roughness contribution between about $a_{tm}(f_r)$ =80% and almost 100%, except for surface c) which mostly lacks singular diffraction peaks. The overall contribution to the rms roughness is for surface a) and b) only about a third.
Especially near angle scattering tends to be dominated by the random roughness of the turn-

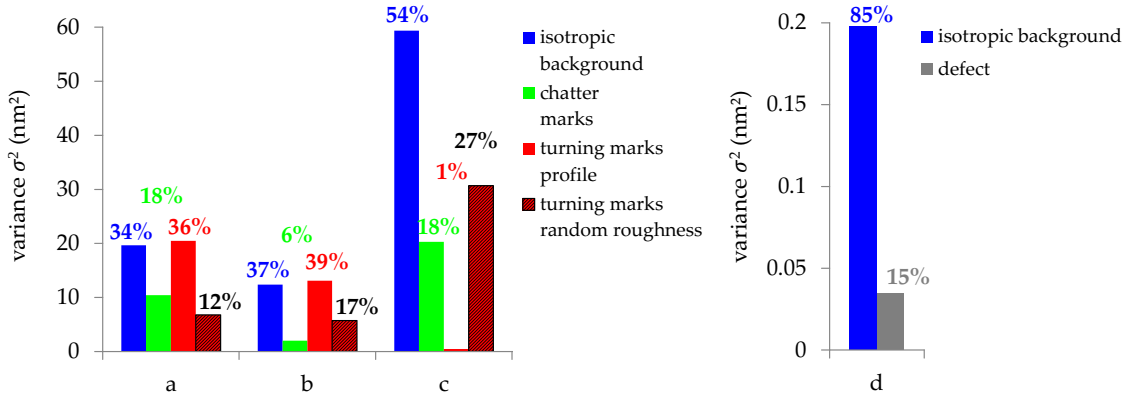

Figure 4.5: Total roughness contributions of all four surfaces. The percentiles above the bars are the contribution factors $\overline{a_{rm}}$, $\overline{a_{cm}}$, and $\overline{a_{isoBG}}$. For the polished sample, a contribution factor for the localized defect has been accordingly calculated.

ing marks, however, an according domination of σ observed earlier [92] was not confirmed. Interestingly, for surface a) and b) the surface with the broader turning mark pitch achieves a more isotropic near angle scattering. Furthermore, for both surfaces $a_{tm}(f_r)$ shows a bulge around the harmonics of the third and fourth order, where the random roughness of the turning marks grows to the major contributor.

A broad yet pronounced maximum in $a_{cm}(f_r)$ is observable, whose position in f_r is different for surface a) to c). The chatter marks on surface a) and surface b) are especially interesting as they where manufactured on the identical sample (material) with different process parameters. The peak was shifted by about a factor of 10 in f_r by changing the manufacturing parameters, chatter is accordingly not a pure material intrinsic parameter (which would be e.g. the chip drag of material intrinsic structures). Origins are discussed in the next section. Following the assumption made in the isotropy section that for sample a) and b) the isotropy contribution contains to a large extend chatter contribution, the roughness of surface a) and b) is in almost equal parts influenced by chatter and turning marks! Contrary, surface c) should be optimized regarding the isotropic roughness contributions, which is probably a material parameter. Also, the random roughness of the turning marks strongly dominates the profile contribution, which is relatable to marks misalignment as will be shown in the next section. The local defect on surface d) has a low influence on the rms roughness and accounts only at low spatial frequencies.

4.1.3 Discussion of possible origins

At the discrete spatial frequencies of the peaks, the profile of the turning marks is the dominating roughness contribution between about $a_{tm}(f_r)$ =80% and almost 100%, except for surface c) which mostly lacks singular diffraction peaks. The overall contribution to the rms roughness is for surface a) and b) only about a third.

Especially near angle scattering tends to be dominated by the random roughness of the turning marks, however, an according domination of σ observed earlier [92] was not confirmed. Interestingly, for surface a) and b) the surface with the broader turning mark pitch achieves

a more isotropic near angle scattering. Furthermore, for both surfaces $a_{tm}(f_r)$ shows a bulge around the harmonics of the fourth and third order, where the random roughness of the turning marks grows to the major contributor.
A broad yet pronounced maximum in $a_{cm}(f_r)$ is observable, whose position in f_r is different for surface a) to c). The chatter marks on surface a) and surface b) are especially interesting as they where manufactured on the identical sample (material) with different process parameters: the peak was shifted by a factor of 10 in f_r. The contribution of the chatter marks can be obviously affected by the manufacturing parameters, rather than being a material intrinsic parameter (e.g. chip drag of material intrinsic structures). Origins are discussed in the next section.
Following the assumption made in the isotropy section that for sample a) and b) the isotropy contribution contains to a large extend chatter contribution, the roughness of surface a) and b) is influenced to about an equal amount by chatter and turning marks! Contrary, surface c) should be optimized regarding the isotropic roughness contributions, which is probably a material parameter. Also, the random roughness of the turning marks strongly dominates the profile contribution, which can be related to mark misalignment as will be shown in the next section. The local defect on surface d) has a low influence on the rms roughness and accounts only for low spatial frequencies.

Up to now, the analysis of the effect of chatter on the ARS, including a link to its origins, has not been reported. Furthermore, the effect of machining accuracies on the random roughness of the turning marks will be discussed in this section. To provide a more profound understanding of diamond turned surfaces, surfaces comprising turning and chatter marks were generated in a MATLAB simulation to study the effect of process relevant parameters on the PSD and consequently ARS.

Turning marks, random roughness

To examine the effect of manufacturing accuracies, a cusp-shaped profile was generated in a MATLAB simulation [164]. Dimensions were defined to a pitch of 2.5 µm and cusp heights of 0.8 µm. Machining inaccuracies were simulated by introducing uncertainties for either the vertical or lateral position of the individual grooves. Also tip defects were simulated by replicating a small dent in each of the grooves.

Fig. 4.6 displays sections of the simulated height profiles comprising laterally and vertically misaligned grooves and their corresponding PSD functions. Each of the grooves was individually misaligned by adding a random offset to its lateral and vertical position with a normal distribution, respectively. This random offset was limited to a maximum value of twice the standard deviation. To reduce noise at the edges of the surface profiles, the simulated height profiles were multiplied by a Gaussian shaped function.

Standard uncertainties of 0.1 µm in vertical and lateral direction affect the random roughness component to increase in a specific manner that allows to distinguish both effects. The random roughness is present even far below the first order diffraction peak. From the simulation it can be seen that especially vertical groove misalignment is an unwanted issue for imaging optics as it is capable of significantly increasing near angle light scattering. For surface a) and

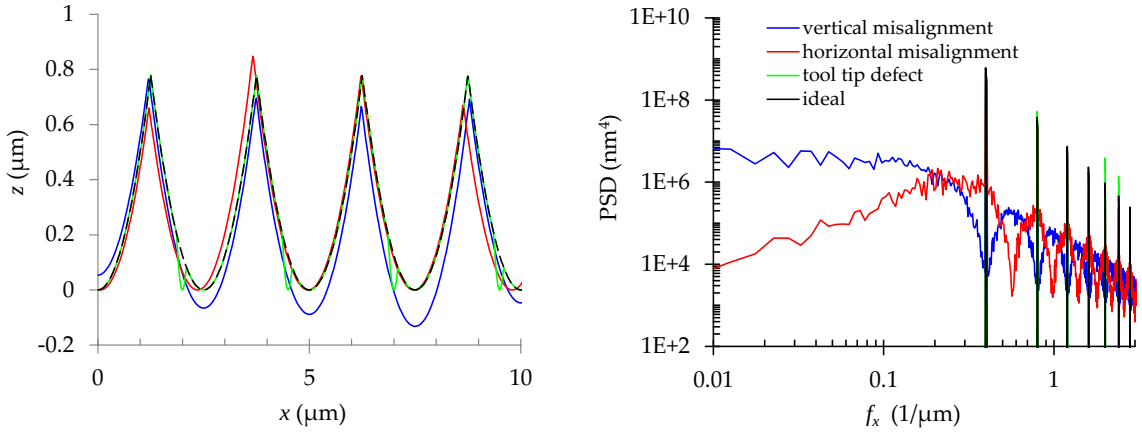

Figure 4.6: Simulation of turning mark profiles (left) with tool tip defects as well as lateral and vertical misalignment; and the corresponding effect on the PSD (right).

c) the PSD of the turning marks increases below the first harmonic order, which indicates a vertical misalignment of the turning marks.

Replicated scratches inside the turning marks, originating e.g. from a defect of the turning tool tip, only influence the amplitude of the discrete peaks and have no effect on the random roughness component (solid green line in Fig. 4.6). However, non-periodic scratches from dragged flakes or non-ideally reproduced grooves (e.g. caused by tool tip wear) increase the random roughness component.

As groove misalignment strongly depends on positioning accuracies of the tool tip and material intrinsic effects, the random roughness of the turning marks represents a process signature parameter. A kind of a "quality attribute" of the turning marks, which is potentially hard to optimize for the identical machine, material, and tool tip velocities. This assumption is supported by the fact that the variance of all roughness contributions from surface a) and surface b) was decreased by about the same amount (see Fig. 4.5: 7.3 nm²< $\Delta\sigma^2$ <8.5 nm²) - except for the turning mark random roughness which is about constant ($\Delta\sigma^2$=1.0 nm²).

Turning marks, profile

The profile of the turning marks influences the discrete peaks in the PSD in amplitude and spatial frequency. ARS data consequently enables to predict the average groove pitch (with uncertainties of about 1% [92]) by evaluating the spatial frequency vector of the peaks. If the according phase values are estimated by an educational guess, it is moreover possible to calculate the groove shape [167]. By averaging the pitch values calculated from the higher harmonics in the PSDs, a groove pitch of 4.99 µm and 9.97 µm was derived for sample a) and b), respectively. Interestingly, the total rms roughness value is lower for the surface with the larger turning mark pitch (8.8 nm for sample a) and 6.0 nm for sample b) within 0.06 µm^{-1} and 1.77 µm^{-1}). Perfectly symmetrical grooves inhibit only odd orders. Asymmetries in the groove profile lead to even order harmonics, which can be observed for surface a) and b). Surface a) shows a small peak at a spatial frequency of 0.1 µm^{-1} and moreover small peaks between the main lobes. All these peaks are located at spatial frequencies that correspond to the odd orders of a pitch of 9.94 µm. Possible even orders are superimposed by the bigger diffraction

peaks from the 4.99 µm grating. This superimposed pitch could be either a systematic vertical misalignment of the grooves, or can more probably be related to residual turning marks from a previous manufacturing step. In contrast, surface c) shows no clear periodicity. Although the position of the isolated peak corresponds to a pitch of 1.68 µm, the main pitch is probably covered in the dominating random roughness of the turning marks.

Chatter marks

Chatter marks are conceived to result from tool vibrations. These tool vibrations cause structures along the turning marks, hence, one would suppose a one-dimensional PSD that is perpendicular to the orientation of the turning marks. Contradictory, the 3D-ARS region that is affected by chatter exhibits apparently a clearly 3D nature. This can be explained by either chatter marks the exhibit a two-dimensional shape, but also by phase shift effects between 1D shaped chatter marks.

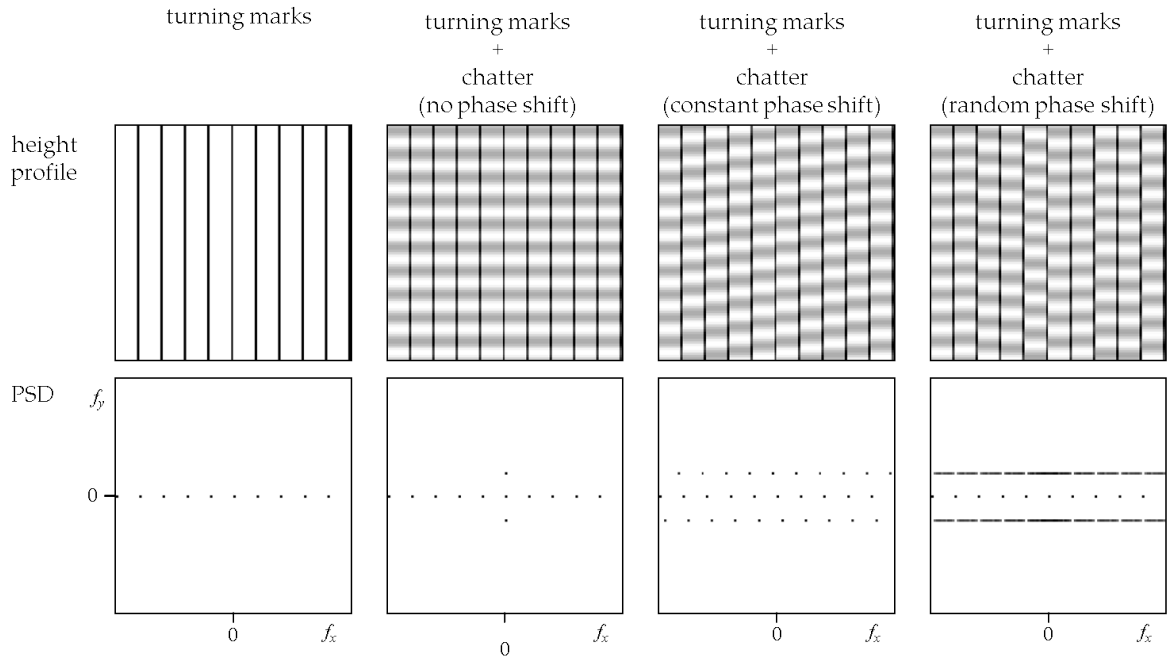

Figure 4.7: Effects of phase shift of the chatter marks on the 2D-PSD.

Fig. 4.7 shows Matlab simulated height profiles and their corresponding 2D-PSD (which corresponds for smooth surfaces to the 3D-ARS). The 2D-PSD of grooves with sine shaped one-dimensional chatter marks is also one-dimensional. However, phase shifts between the chatter marks result in a 2D extension in the PSD. For a constant phase shift between the chatter marks a characteristic azimuthal misplacement of the chatter mark peaks can be observed, where the side lobes are of lower power. For a random phase shift, the lobes broaden to a more line shaped distribution. This allows two conclusions:

- The characteristic azimuthal offset in the scattering characteristic that corresponds to the chatter marks can be explained by a constant phase shift between the individual grooves. This constant phase shift is probably moreover superimposed with a small random phase shift.

- The 3D-scattering characteristic of the chatter marks can be a result from a 1D-roughness component.

Moreover, the 3D-ARS contains information that allows one to separate different effects in chatter marks:

UP surfaces are typically machined with constant parameters: the sample is rotated with constant angular velocity ω_{tool} while the tool tip is moved with constant speed straight over the surface creating a spiral-like groove. Presumably, chatter is further dividable into (1) vibrations from the machining periphery with constant time frequency, (2) vibrations from the machining periphery with a time frequency proportional to ω_{tool}, (3) tool tip vibrations that are induced by interactions with the sample surface, as well as (4) vibrations that are correlated to the granular intrinsic material structure.

The manufacturing process affects in the track speed of the tool tip $\mathbf{v}_{tip}$ to be a function of the distance from the center of rotation r_{turn} such that $|\mathbf{v}_{tip}| = \omega_{tool} r_{turn}$. Tool tip vibrations with the time depended frequency $f_{tool,Hz}$ are consequently scribed into the surface to chatter marks with the spatial frequency f_{cm} - as a function of the sample position:

$$f_{cm}(r_{turn}) = f_{tool,Hz} / (\omega_{tool} \cdot r_{turn}) \ . \tag{4.8}$$

From an analytic point of view, this is a nice feature as one gets $\mathbf{v}_{tip}$ varied freely over the sample position while the other parameters are kept fixed. By performing measurements at different radial sample positions, more information about the possible origins of chatter can be obtained. Hence, if chatter is dominated by the granular material structure, its spatial frequency f_{cm} is constant at sample positions (r_{turn}). If chatter is dominated by machining vibrations, its time frequency is constant and the corresponding spatial frequency $f_{cm}(r_{turn})$ should be a function of the sample position. This causes the corresponding scattering distribution to be shifted towards the specular beam with increasing r_{turn}.

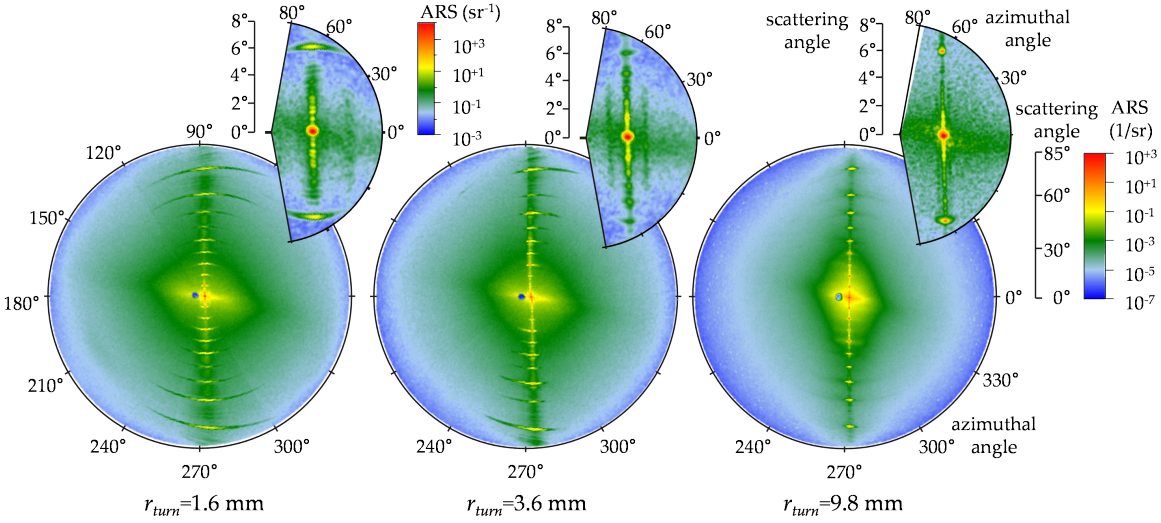

Figure 4.8: Chatter shift as a function of the tool distance from the center of rotation r_{turn}.

Fig. 4.8 shows 3D-ARS measurements of surface a) at different radial positions. The measurement parameters of the hemispherical scan were identical to the previously performed 3D

measurements on this sample. An additional highly resolved measurement of the near angle scattering section was performed with $\Delta\Omega = 7 \cdot 10^{-6}$ sr for each position. The radial positions were tracked by moving relatively to the sample center using manual micro positioners.
Two effects can be observered:

- The ARS level of the chatter marks at high scattering angles decreases with increasing r_{turn} (the shape shifts towards the specular beam).
- A pronounced structure in the near specular region, orientated parallelly to the diffraction peaks of the turning marks, shifts towards the specular beam with increasing r_{turn}. The structure resembles to the simulation with the random phase shift between the chatter marks and probably originates from a vibration source with high amplitude.

In Fig. 4.9, the spatial frequency of the observed pronounced chatter structure is plotted over r_{turn}. The spatial frequency was calculated from five near angle ARS measurements at different radial positions. A fit of Eq. (4.8) (dashed line) with $\omega_{tool,Hz}$=1000 rpm (from the manufacturing process) reveals a vibration source of constant time frequency with $f_{tool,Hz}$=14.7 kHz. It can be moreover observed that the 3D-ARS shifts towards the specular beam (for increasing r_{turn}) even for other scattering angles. This supports the assumptions made earlier in this section: (1) the isotropic background calculated in chapter 4.1.2 for sample a) and b) still contains contributions of chatter; moreover (2) the isotropic roughness component that corresponds to the granular material structure is superimposed and dominated by the chatter marks (a material intrinsic isotropic background would not shift).

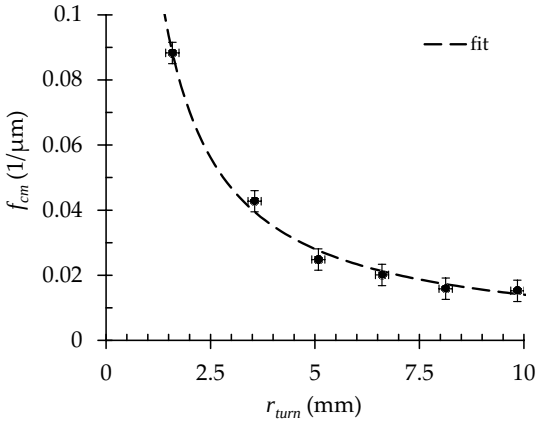

Figure 4.9: Chatter shift as a function of the tool distance from the center of rotation r_{turn}.

4.1.4 The role of the illumination wavelength

As pointed out in chapter 4.1.1, the introduced isotropic background can be generally used to characterize the optically relevant degree of isotropy for arbitrary samples as a function of the illumination wavelength. Therefore, the integration limits in Eq. (4.6) are chosen according to the application relevant scattering angles. The 2D-PSDs of an aluminum coated float glass substrate and the isotropy factor $a_{iso}(f_r)$ are calculated from various WLI, AFM, and ARS measurements to cover a spatial frequency range between 0.001 µm^{-1} and 100 µm^{-1}.

The degree of isotropy (see Fig. 4.10) calculated from topographic data is obviously much

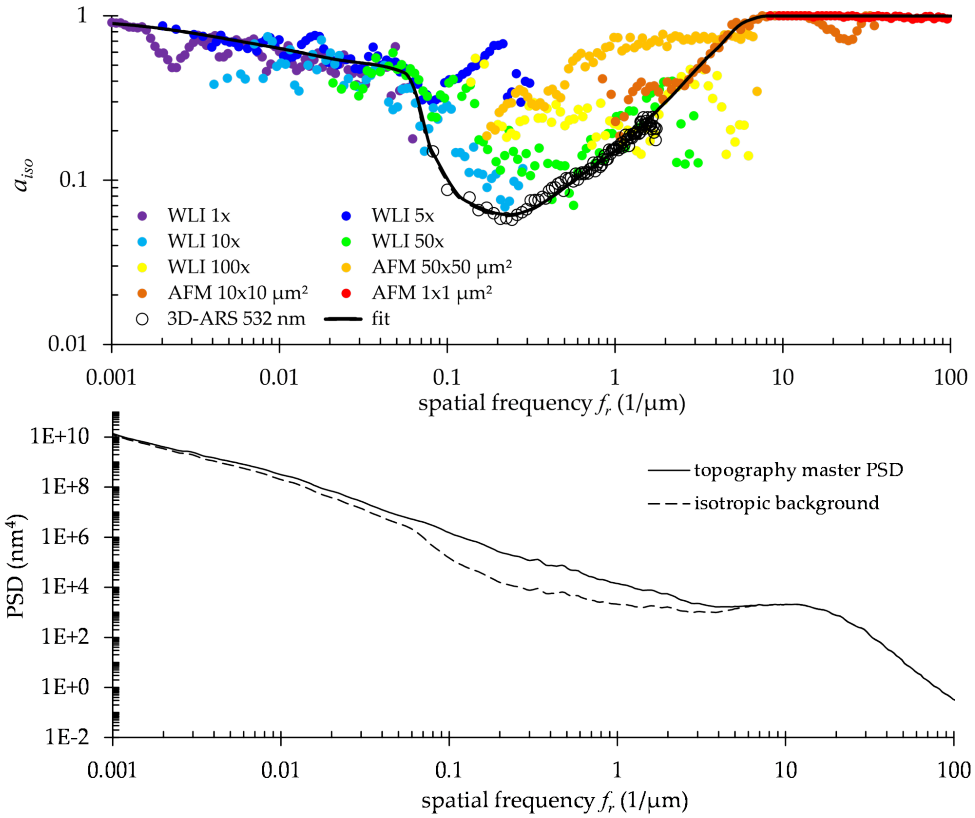

Figure 4.10: Degree of isotropy (top) and master PSD (bottom) of an aluminum coated B270 substrate with an SiO_2 top coating over a broad range of spatial frequency.

more affected by noise than the degree of isotropy calculated from the 3D-ARS (see also Fig. 4.1). Especially low power densities in the 2D-PSD with a high spatial frequency are covered by noise, which artificially increases $a_{iso}(f_r)$. Especially the 50x50 µm² AFM scan and the 100x WLI measurement show huge deviations, explainable by artifacts and the small measurement field that may not represent the ensemble average. A spline curve is fitted (black solid line) that is to a large extent orientated along the scattering measurement.
From the master PSD [152], the isotropic background is calculated using Eq. (4.3). Interestingly, isotropy has recovered at about the same spatial frequency (about 8 µm^{-1}) at which the "knee" of the coating can be observed in the 2D-iso PSD. Hence, the intrinsic roughness of the coatings increases the isotropic background and covers low power anisotropic features. Coatings can obviously be used to reduce anisotropy (see [175]).

The application wavelength specific degree of isotropy $a_{iso}(\lambda)$ is calculated (Eq. (4.6), Fig. 4.11 upper right) for illumination wavelengths ranging from λ=10 nm up to 20 µm. Moreover, the relevant rms roughness σ_{rel} and the total scattering loss are calculated from the 2D-iso PSD. Anisotropy maximizes at an illumination wavelength of 534 nm, contributing with $1 - \overline{a}_{iso}$ =65% to TS and σ_{rel}. Isotropic scattering is only achieved for illumination wavelengths <100 nm, however, surface roughness leads to impracticable scattering losses in the UV[4]. For FIR applications e.g. at λ = 10.6 µm, the $\overline{a}_{iso}$ =77% leads to residual 23% anisotropically scattered power. However, anisotropy also introduces wavefront errors that

[4]The drop of TS towards lower illumination wavelength can be related to absorption effects of aluminum.

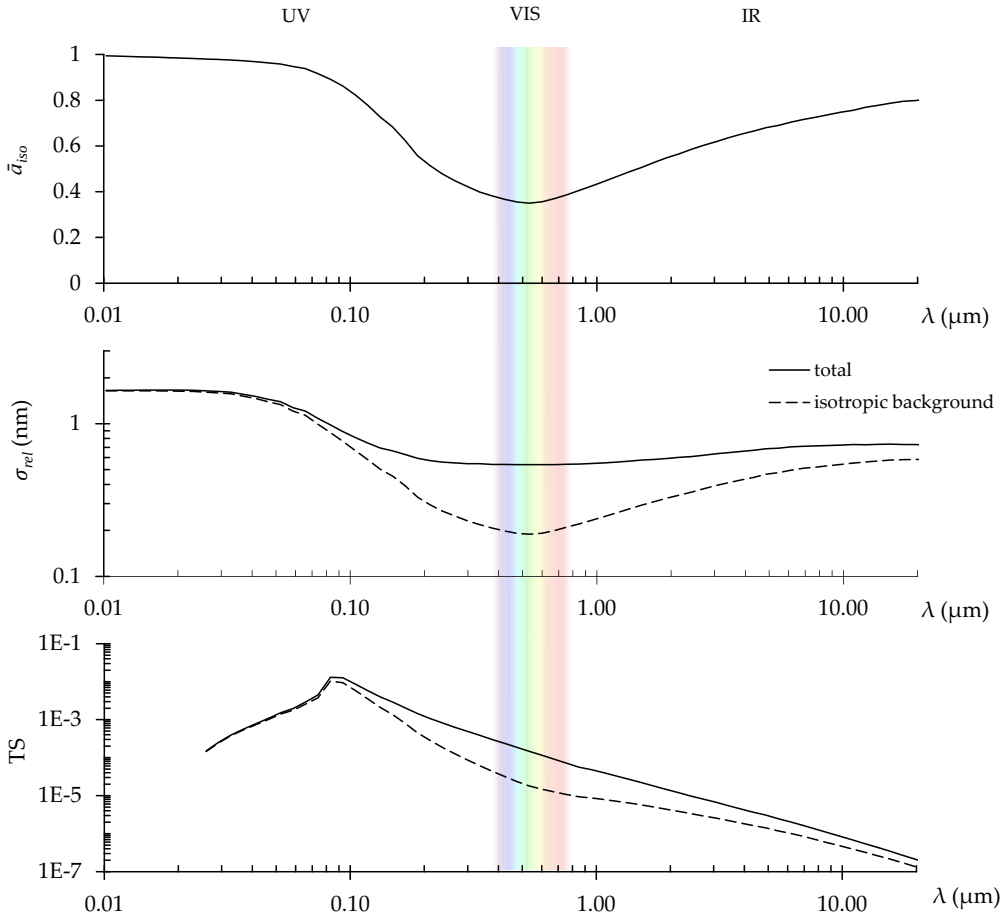

Figure 4.11: Effects of anisotropy (top) on the rms roughness (center) and TS (bottom) as a function of illumination wavelength (same sample as in Fig. 4.10).

could be critical for imaging applications. Nevertheless, aberrations, anisotropic scattering, and surface roughness are potentially tolerable for illumination optics from VIS to FIR.

4.1.5 Summary

For a comprehensive characterization of individual roughness components of UP surfaces, a new anisotropy analysis method was introduced. In contrast to previously published methods, it is spatial frequency resolving and directly linked to optical and roughness properties. Therefore, the components are separated in the 2D-PSD by a spatial frequency discrimination. It is also applicable to analyze the degree of isotropy in general and allows one to evaluate anisotropy as a function of illumination wavelength. This is especially useful to specify anisotropy and roughness with regard to application, which was demonstrated for a coated anisotropic glass substrate.

It could be shown that 2D-PSD functions of anisotropic samples are beneficially calculated from 3D-ARS measurement instead of WLI and AFM scans. This was demonstrated by a comparison of 2D master PSDs derived for a diamond turned surface. The directional rms roughness and the 2D-*iso* PSD showed a very good agreement. However, if the 2D master PSDs that were used for this calculation are directly compared, the light scattering 2D-PSD

exhibits visibly less artifacts and statistical fluctuations.

The individual roughness components of different UP diamond turned surfaces were analyzed and discussed using the proposed method. It was found that the spatial frequency dependence of different superimposed roughness components (1D, 2D-isotropic, 2D-anisotropic) are fundamental to the previously conceived spatial frequency dependent nature of anisotropy [18].

Simulations of surfaces with turning marks showed that machining accuracies have a significant impact on the random roughness component of the turning marks. Phase shifts between the individual chatter marks were identified to be a possible origin of the characteristic (non-perpendicular) azimuthal offset of chatter in the 3D-ARS. Moreover it could be demonstrated that the 3D-ARS of chatter shifts with the radial position on the sample. This was shown to allow the determination of the time frequency of a vibration source in the machining process.

It was concluded that chatter marks are capable of completely superimposing the isotropic background of diamond turned surfaces. Under this assumption chatter would contribute about 50% to the total rms-roughness of two analyzed samples. This is contrary to an earlier publication [92] where the random roughness was found to be the typical dominating component.

4.2 Characterization of coatings and their substrates

PSD analysis based on ARS measurements performed in the VIS spectrum cover comparable spatial frequency ranges (see tab. 4.1). A combination of PSDs calculated from VIS ARS measurements does consequently not lead to a significant extension of the accessible spatial bandwidth.

Table 4.1: Spatial frequency ranges of ARS measurements in the VIS spectrum for scattering angles of 2° and 85° and normal incidence.

λ(nm)	f_{min} (µm^{-1})	f_{max} (µm^{-1})
405	0.0862	2.46
532	0.06	1.87
640	0.0545	1.56

However, the redundant information can be very valuable: If the PSDs overlap, the smooth surface approximation can be assumed to be appropriate for the sample: Accordingly, the surface can be assumed as being clean and the derived PSD represents the sample surface [3].

Wavelength scaling methods were mainly used in the 80s and early 90s to (i) confirm light scattering models [176], (ii) check instrument accuracy [177], (iii) identify topographic scattering [18, 178, 179], and (iv) extend the spatial frequency range in the PSD [18].

The degree to which the measurements scale was sometimes quantified by relating the integrated rms roughness values $\sigma(\lambda)$ (in the same bandwidth of spatial frequencies).

Wavelength scaling experiments were expensive and time-consuming, because state-of-the-art scatterometers usually required a more or less elaborated refitting procedure between wavelength changes. Hence, measurements were sometimes taken at that day where both the sample was available and the instrument was set up for the right wavelength [177]. Possible resulting deviations in the measurement position are capable of causing uncertainties in post-measurement analysis. In particular for the interesting case where the PSDs do not overlap, it is not clear whether the deviations are uncertainty related or can be traced to correlatable light scattering effects of the same origin. Highly-correctable wavelength scaling experiments are especially crucial for samples with low homogeneity, which is the case for surfaces with contaminations or defects.

Experiments were usually performed over a wide range of wavelengths from UV to IR. However, using only VIS wavelengths maximizes the overlapping bandwidth; moreover, light scattering effects tend to become easier to correlate, regarding the smooth surface approximation, as well as deviations of the skin depth into the surface, or deviations in the refractive index for PSD calculations.

4.2.1 Description of the method

In this section, the multi-λ capability of the instrument will be used to study wavelength scaling of optical coatings and their substrates concerning predictions of surface roughness, roughness growth, as well as the characterization of optically relevant contamination.

The instrument developed in this work firstly provides identical illumination spots (position and size) for different illumination wavelengths without the need of intermediate calibrations

or any realignments (sample or beam preparation system). The scatterometer allows sample and illumination system to stay fixed during wavelength changes (or parallel wavelength measurements) which eliminates any correlation errors between multi-λ ARS measurements except of the sufficiently small measurement uncertainties of the instrument.
The study reported in this section is different from the previous publications because (i) the examples include uncoated substrates, metallic top coatings, multilayer coatings, and clean and contaminated single surfaces and interference coatings; (ii) the ARS measurements were performed at three VIS wavelengths and are highly correlatable; (iii) the overlap of the PSDs is evaluated as a function of spatial frequency; (iv) all results are verified by various topographic measurements.

4.2.2 Application

If not otherwise denoted, the measurement and analysis of the samples were performed under the following conditions: The samples were measured at all three illumination wavelengths currently implemented in the instrument (405 nm, 523 nm, and 640 nm) under s-polarized illumination and unpolarizing detection. A small OOP angle <2° was adjusted, which was shown to have only a negligibly low effect on the measurement uncertainty (see chapter 3.6.3) and allows sectional ARS measurements to be obtained without obscurations. For all samples θ_i=0° and $\Delta\theta_s$=0.5° were chosen. The solid angles were $\Delta\Omega$=9.7 · 10^{-4} sr for scattering angles larger or equal to 5° and 1.0 · 10^{-5} sr for scattering angles smaller than 5° from the specular beam. The master PSDs were derived from WLI and AFM measurements [180].

Roughness-induced scattering

Fig. 4.12 shows the ARS of a 200 nm thick magnetron sputtered titanium coating on a fused silica substrate [181].

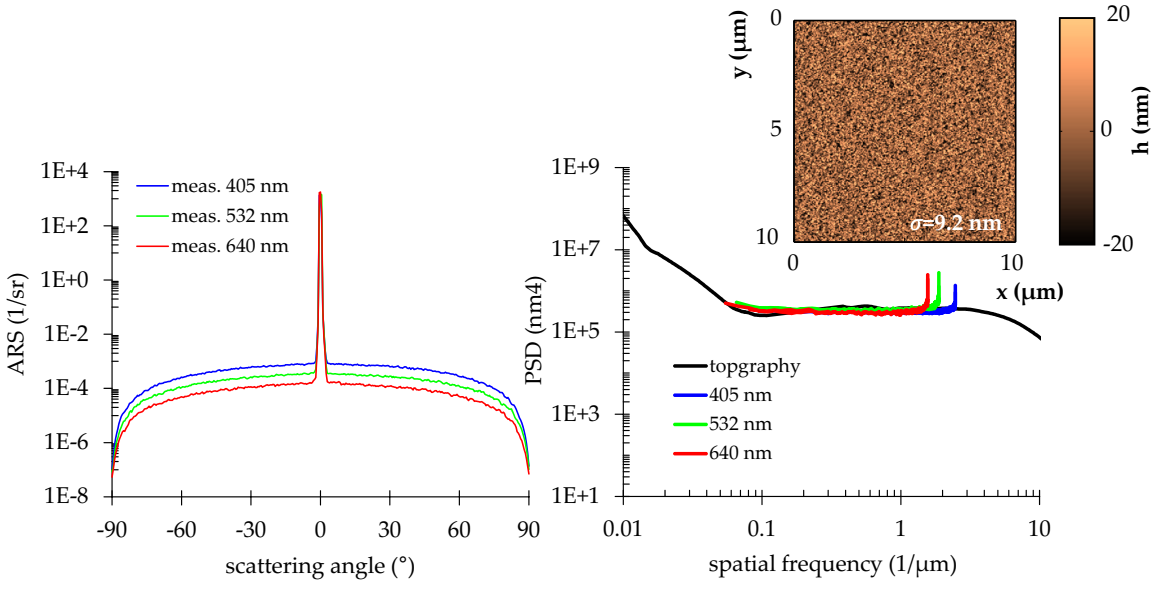

Figure 4.12: ARS and PSD analysis of a titan coated fused silica substrate.

The PSDs calculated from ARS measurement data for all illumination wavelengths show almost perfect agreement. It can be consequently concluded that the smooth surface approximation is valid for this sample, the surface exhibits no optically relevant contamination, and the PSDs represent the surface. Comparison to topography measurements proves the conclusions.

Scattering of interference coatings

Scattering from multilayer coatings is different from single surfaces, as interference effects may occur. However, if the layers are fully correlated the sample acts as a single opaque surface [104]. Overlapping PSDs derived from different λ consequently indicate fully correlated layers and represent the PSD of the individual interfaces.

In Fig. 4.13, the measured ARS of an aluminum coated B270 glass substrate with an SiO_2 top coating is displayed. The metal and the SiO_2 coating were evaporated to yield 50 nm and 40 nm thick layers [182], respectively.

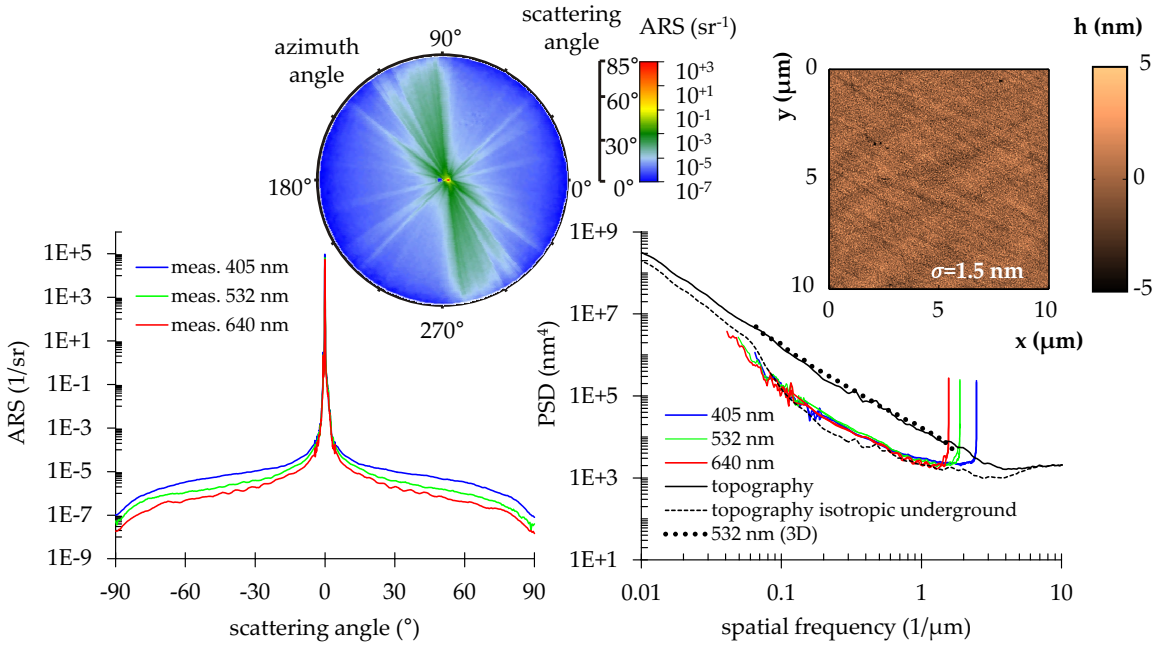

Figure 4.13: ARS and PSD analysis of an aluminum coated B270 substrate with a 40 nm SiO_2 top coating.

The PSDs calculated from ARS measurement data of all illumination wavelengths again show a remarkably good agreement. Hence, the single surface approximation is appropriate for this sample, and the surface is clean. Moreover, the overlapping PSD indicate no relevant roughness growth for the SiO_2 layer and the PSD represents the interfaces.

Though, comparison to the topographic master PSD shows deviations of about 1 OOM. An additional 3D-ARS scan performed at 532 nm revealed a pronounced anisotropy with $\overline{a}_{iso}(\lambda = 532\,\text{nm})$ =35% (within 0.06 µm^{-1}and 1.77 µm^{-1}) originating from the B270 glass substrate. Accordingly, the calculated representative isotropic 2D-PSD from the 3D-ARS shows a good agreement to the master PSD. The topographic isotropic underground PSD was calculated using the derived $a_{iso}(f_r)$ from chapter 4.1 (same sample) with good agreement

to the PSDs calculated from sectional ARS data. No remarkable contamination was detected in the AFM measurement.

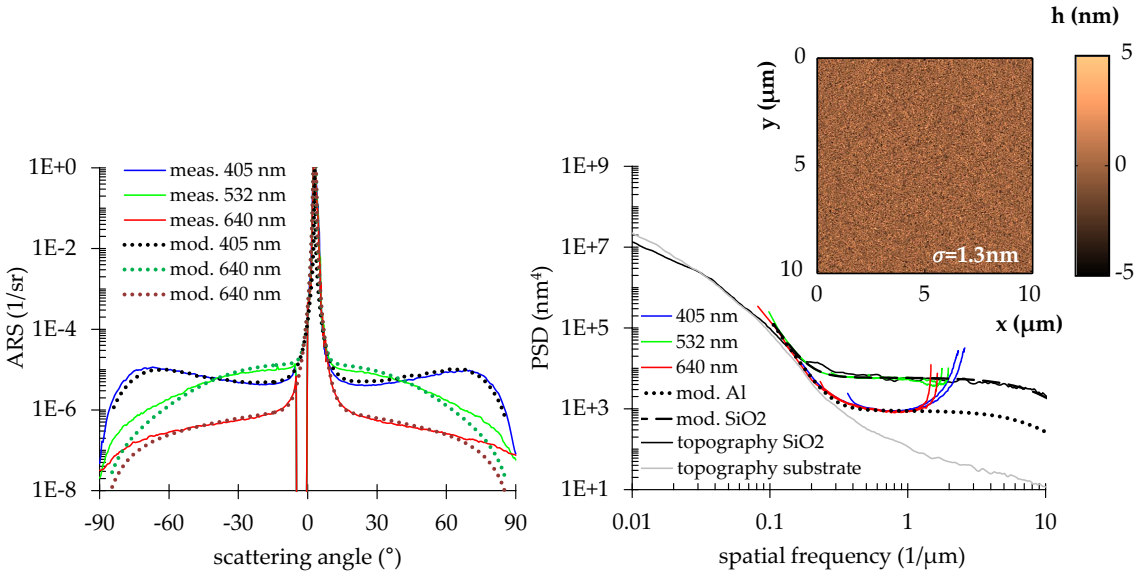

Figure 4.14: ARS and PSD analysis of an aluminum coated fused silica substrate with a 250 nm SiO_2 top coating.

The ARS of an aluminum coated fused silica substrate with an SiO_2 top coating was measured (Fig. 4.16) at θ_i=3°. Both the metal and the SiO_2 coating were evaporated, yielding layer thicknesses of 100 nm and 250 nm, respectively. The layer thickness of 250 nm compromises the single surface approximation, as it is not clear if fully correlated layers can be assumed. The ARS measured at 532 nm illumination is over 1 OOM higher than the ARS(λ=640 nm) and partially even exceeds the ARS(λ=405 nm) (see 4.14). The calculated PSDs following the single surface approximation overlap only at small spatial frequencies, which represents scattering from fully correlated layers with ideal substrate roughness replication. Interestingly, the PSD functions derived from the ARS measurements at λ=405 nm and 640 nm agree well. In order to derive the missing parts PSDs of the SiO_2 top layer and the Al intermediate layer interface, interference effects have to be considered.
Rönnow [183] showed that a direct calculation of the PSD functions of double layer coatings from ARS measurements performed at three illumination wavelengths (in an. attempt to solve the inverse scattering problem for coatings), results in impracticably large uncertainties as a function of the layer design and the chosen illumination wavelengths. Though, by the implementation of conventional model PSD functions the degrees of freedom can be tremendously reduced. The iteratively approach developed by Schroeder [50] allows (by a single ARS measurement) the PSD functions from intermediate layers and the deviation δ of the layer thickness H to be derived - if the top layer PSD function and the layer design are known. By implementing the information of three $ARS_{meas}(\theta_s, \lambda)$ in this approach, it will be shown that the top-layer PSD can also be derived with the following steps:

- Determination of appropriate start parameters for the model PSD functions (from single surface approximation and/or an educated guess) and the layer thickness (250 nm from the layer design).

- Calculation of the modeled $\mathrm{ARS}_{mod}(\theta_s, \lambda, A_1, A_2, \delta)$ according to the partial correlation model [100].
- Calculation of the merit function MF:
  $\mathrm{MF} = \sum_{\theta_s,\lambda} (log(\mathrm{ARS}_{meas}(\theta_s, \lambda)) - log(\mathrm{ARS}_{mod}(\theta_s, \lambda, A_1, A_2, \delta)))^2$.
- Minimization of the MF by refinement of A_1, A_2, and δ.

ARS_{meas} and ARS_{mod} are the experimental and the modeled ARS function, respectively. A_1 and A_2 are parameters of the model PSDs of the Al/SiO_2 and the SiO_2/air interface and correspond to the level of the PSD function, respectively. The PSD functions of the top layer and the intermediate layer were composed from a conventional ABC-PSD function (coating) and a fractal PSD (substrate), respectively (see e.g. [3]).

The modeled ARS functions finally fit well to the experimental light scattering data for a layer thickness of 230 nm (δ=-20 nm). The calculated PSD functions from topographic measurements[5] are in very good agreement [180] to those derived from the ARS analysis.

Contamination on single surfaces

In Fig. 4.15 the PSD calculated from AFM and 3λ-ARS measurements of a RG1000 glass substrate at two different measurement positions are shown. The substrate has experienced several cleaning procedures (in the order performed: acetone / ethanol wiping, polymer film drag-off, ultrasonic cleaning). The PSDs derived from the ARS measurements agree only at

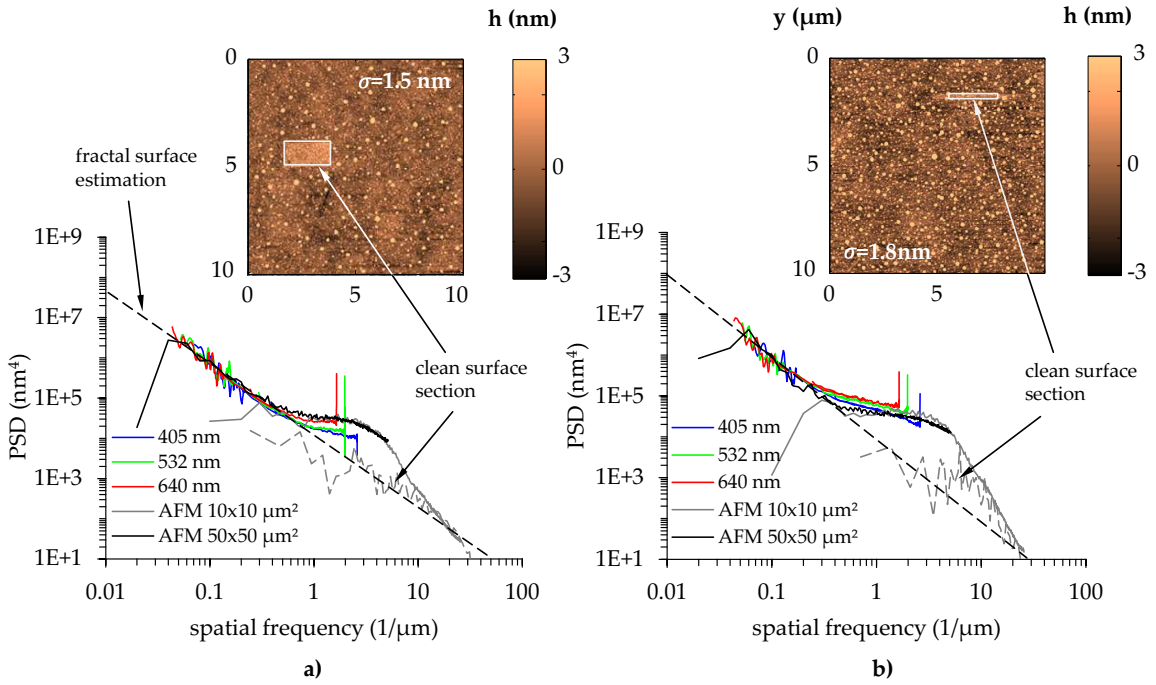

Figure 4.15: Calculated PSDs of a RG 1000 glass substrate at two different measurement positions with different degrees of contamination.

low spatial frequencies. These ranges in the PSD are consequently assumed to represent the topography of the surface. At higher spatial frequencies there is a substantial disagreement

[5]The substrate PSD was determined from the backside of the mirror.

between these PSD functions. This indicates the presence of non-topographic scattering, potentially arising from contamination in different degrees at the two measurement positions. In fact, the AFM scan reveals contamination on the surface at both measurement positions and in different degrees.

In order to determine the PSD of the clean surface from the topographic measurements, two approaches are pursued (see Fig. 4.15): (i) the fractal part of the PSD at low spatial frequencies is extrapolated towards higher spatial frequencies, as polished surfaces usually exhibit a fractal PSD; and (ii) the PSD of a sectional cut in the 10x10 µm² AFM scan where contamination was low was calculated. The fractal extrapolation and the PSDs in the sectional cut agree well, which supports the validity of the determined PSD of the clean surface.

It can be observed that at spatial frequencies where the SSA-derived PSDs overlap, they fit to the topographic PSD of the clean surface. Hence, although the smooth surface approximation seems to be inappropriate for contaminated samples, wavelengths scaling allows surface representative roughness information to be obtained.

Contaminations on interference coatings

Fig. 4.16 shows the ARS of an aluminum coated BK7 substrate with an SiO_2 top coating. The aluminum and the SiO_2 coating were deposited by vacuum evaporation, yielding layer thicknesses of 200 nm and 180 nm, respectively.

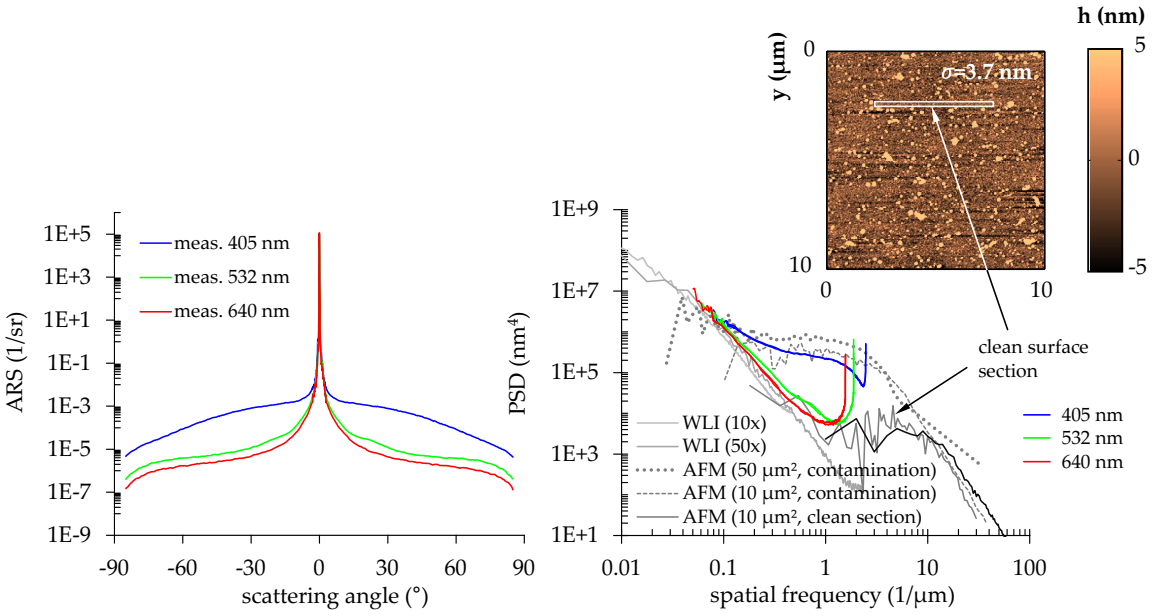

Figure 4.16: ARS and PSD analysis of an aluminum coated BK7 substrate with a 50 nm SiO_2 top coating.

Comparison of the SSA PSDs identifies topographic scattering and correlated interfaces for $f_r < 0.1$ µm^{-1}. For larger f_r the PSD(λ=532 nm), deviates marginally from PSD(λ=640 nm), while the PSD(λ=405 nm), deviates clearly by almost 2 OOM as a result of the interference coating and the contamination.

The AFM scans reveal the presence of particles or defects on the surface. To yield the PSD that corresponds to the clean topography, the PSD of a sectional cut in the 10x10 µm² AFM

scan with no particles (see Fig. 4.16) was calculated. Moreover, the 1x1 µm² AFM scan did not exhibit any particles.
Again, it can be observed that at spatial frequencies where the SSA PSDs derived from different λ overlap, they moreover fit to the topographically determined PSDs of the clean surface - despite the contamination and despite the interference coating.

4.2.3 Summary

In this chapter, the multi-wavelength capability of the instrument developed in this work, and its capability to provide identical illumination spots at different λ, was utilized to provide transparent and reliable PSD data from diverse optical coatings and an uncoated substrate.

It was demonstrated that a three-wavelength analysis of clean interference coatings is capable of determining the layer thickness as well as the PSD functions of the top and intermediate layer. Therefore, post-measurement analysis was performed by means of model PSD functions and by evaluating a merit function. The derived PSDs of the interfaces of an Al /SiO_2 coating showed good agreement with topographic measurements.

The previously postulated "wavelength scaling" assumption, that PSD functions derived from multi-λ ARS measurements overlap and represent the topography for smooth and clean surfaces, was confirmed. Beyond these findings, wavelength scaling analysis following the smooth / single surface approximation was found to yield surface representative PSD functions even for interference coatings and / or contaminated samples. Therefore, the overlap is analyzed as a function of spatial frequency. It was shown that the PSDs represent the interface roughness in regions of f_r where they overlap. This holds although they might significantly deviate in other regions of f_r. The analysis was verified by a comparison of light-scattering-derived PSDs to PSDs calculated from WLI and AFM measurements.

A contaminated interference coatings and a single surface were investigated using the wavelength scaling approach. In contrary to topographic measurements, only optically relevant contamination is detected without being dependent on assumption or the accuracy of models. This enables the identification of - related to the sample's surface roughness - optically relevant contamination problems or optimization potentials of the cleaning process of substrates, coatings, and polished surfaces.

The wavelength scaling method helps to simplify post-measurement analysis of light scattering measurements, because it becomes quickly evident if and which part of the calculated PSD represents the surface or not. Furthermore, it shows if the often made assumption of an optically smooth and clean surface is appropriate: If the PSDs fit, you know you are doing it right - at least very likely

Further investigations of the wavelength scaling properties of thin film coatings and their substrates are published by the author in [184].

4.3 Evaluation of diamond cuts

The optimization of the optical performance and appearance of diamond cuts is a well researched topic. In 1919 Marcel Tolkowsky published his book “Diamond Design” [185]. Though diamond cut proportions were studied and evaluated since the middle of the 18th century [186], Tolkowsky’s work is to our time the best known [187]. To this day, his proposed cut with “best proportions” has been used as a reference for diamond grading - although his research is considered as being incomplete [187–189]. By now, researchers at the GIA (Gemological Institute of America), the AGS (American Gem Society), the Moscow State University, and several other labs (see [188]) have dedicated themselves to the analysis, characterization, and grading of gemstone cuts. Their work resulted in metrics to evaluate a diamonds beauty by means of its geometrical cut parameters, as well as to the establishment of diamond grading services [190, 191].

This chapter will investigate the scope of light scattering techniques as a comprehensive characterization tool for gemstone cuts. After a brief review of the diamond grading classes as well as state-of-the-art grading instruments and methods, the suitability of light scattering analysis to assess the individual cut grading classes is studied.

4.3.1 Basics

Diamond grading

It has been established to grade diamonds by the so-called "4C rule" to evaluate Carat, Clarity, Color, and Cut. Thereof cut quality is moreover classified with respect to symmetry, polish, shape (e.g. round, oval), and proportions (facet alignment) and has a major impact on the optical performance of the gemstone. Furthermore, the performance and appearance of diamonds are graded by analyzing "brightness"[6], "fire", and "scintillation"[7].

1. *Brightness* is related to the amount of light that is redirected from the whole incident hemisphere back to the observer [191]. Hereby, the primary reflections from the crown facets (see Fig. 4.17) are denoted as “glare” and do not contribute to brightness[8].
2. *Scintillation* is referred to sparkling effects and changes in the dark/bright pattern when the brilliant is tilted and viewed into the crown [191].
3. *Fire* of brilliants finds its origin in the dispersion of rays in the gemstone, which appear to the observer as areas of extremely bright and distinct colors [191].

A diamond can be cut to yield either more brightness or more fire, though compromises are mostly aspired by modern cuts. For diamond grading, the “face-up” appearance is considered as being of most importance: the observer views with the unaided eye perpendicularly onto the table facet (see Fig. 4.17), while the gemstone is illuminated from light sources located in the upper hemisphere.

[6] Sometimes also referred to as “brilliance” [192].
[7] Sometimes also referred to as “sparkliness” [193].
[8] For e.g. θ_i=0°, assuming no light scattering and no absorption, a Tolkowski brilliant cut redistributes about 91% of the incident power specularly in the reflection hemisphere, including 17% of glare [194]. The residual power is lost because of light leakage through the pavillon facets.

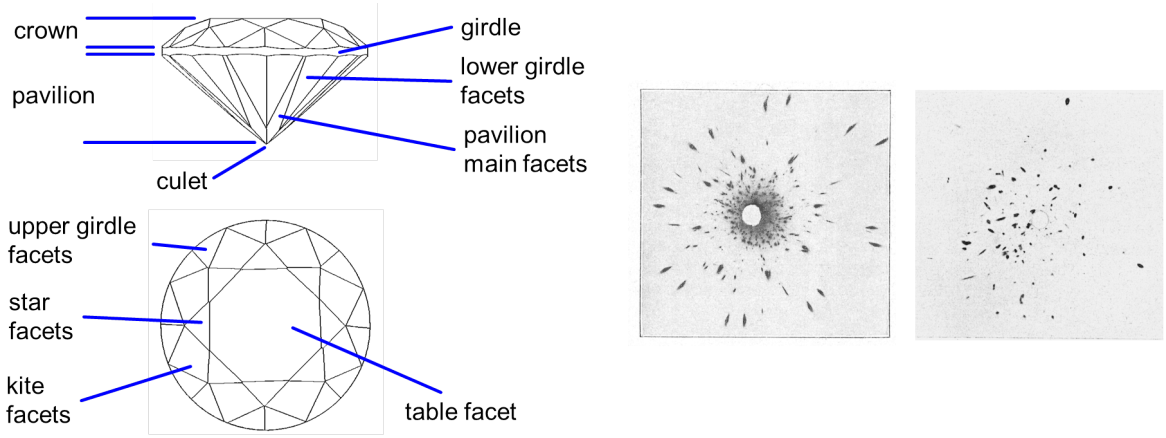

Figure 4.17: Facet geometry of a standard round brilliant cut (left). Photographic reflection spot images by Rösch (1927) of a well (center) and a poor round brilliant cut (right) [195].

Diamond grading instruments

Classically, cut grading is performed subjectively and visually by experts, although even small changes in the observing conditions can lead to a verifiable influence on the grading result (e.g. the color of the clothing of the grading expert [192]). State-of-the-art diamond grading instruments are mostly based on measurements of the gem geometry [196–199]. The optical performance is later on derived by means of proportion tables that were determined by the analysis of previously performed simulations [190, 200–202]. Also, optical viewing tools [203–205] were developed to allow the estimation of a gem's optical performance by the generation and analysis of characteristic patterns, where the diamond is observed in the face-up position and illuminated from different directions. To this day, symmetry, polish, and the appearance of girdle and culet are graded visually with a magnifying tool [190, 191, 206] - though under standardized conditions yet also subjectively.

Reflection spot analysis

Tolkowski (1919) suggested to view fire from a diamond by using a sheet of paper with a pinhole [207] through which the diamond is illuminated perpendicular onto the table. Rösch (1926) developed a technique to produce photographs of these reflection spot distributions to assess the optical performance [195] (see Fig. 4.17). The identical set-up geometry, though with a hemispherical screen, was later used in ray tracing simulations to evaluate fire, scintillations, and brightness of virtual diamond cuts (no defects, no inclusion, no light scattering, mostly perfectly symmetric). The resulting reflection patterns were analyzed using different algorithms and approaches [193, 207, 208].
Following the reverse ray tracing approach, this simulation geometry simply equals to the cuts face-up appearance: the gem is illuminated from the observer's eye position, and one yields a set of ray directions which correspond to illumination directions making virtual facets appear bright when the gem is viewed face-up [208]. If the gem is tilted, this set of ray directions is distorted and "scans" the hemisphere for light sources. Each time a ray strikes a source location, a virtual facet appears bright to the observer. However, the face-up position is regarded as being sufficient to describe a gems performance [193, 194, 207]. Derivation of

the optical performance from (simulated) reflection spot distributions was e.g. performed as follows:

1. *Brightness* is quantified by integration of the reflection patterns, previously performed with [207] or without a weighting factor [193, 208]. Plotting the integrand over the polar angle allows one to identify three important angular regions [194]: the angular region between 15° and 45° is considered as being the most important as it typically contributes the most power, while polar angles larger than 45° typically contribute a small fraction to the brightness of a cut. Angles smaller than 15° produce important contrast in the virtual facet pattern by obscuration of sources by the observers head.
2. *Scintillation* was found to improve with greater number and smaller average size of the reflection peaks, where a most even distribution is aspired [193].
3. *Fire* can be assessed by analyzing the difference of reflection distributions that were determined with different illumination wavelength [193, 207, 208]. It was pointed out that the bigger the dispersed flares are, the higher is the probability that a part of the spectrum is vignetted at the observer's pupil and a colored facet - fire - is perceived [194, 207].

The reflection spot analysis is today used in simulations to evaluate the cut performance of idealized virtual diamond cuts, with only specular effects being considered. The table derived from the simulations are accordingly used to predict and grade the optical performance of real, not perfect diamonds by their cut proportions.
It is a little bit astonishing, that the geometry used in the reflection spot simulations simply equals a 3D-ARS measurement in the reflection hemisphere at normal incidence. In the following, the reflection spot analysis is realized as a highly sensitive and comprehensive measurement concept that allows one to record the reflection distributions of a cut in the whole reflection hemisphere - including light scattering effects, which were previously not investigated. Besides brightness, fire, and scintillation, it will be shown that moreover shape, proportions, polish, and symmetry can be assessed.

4.3.2 ARS simulation of a brilliant cut

A standard round brilliant cut diamond with a girdle diameter of 4 mm and 0.25 carat weight was investigated using both the table top system described in this work and a computer tomography (CT) measurement system. The 3D-ARS measurement was performed with a collimated illumination beam illuminating the whole brilliant perpendicular onto the table facet at λ=532 nm. For faster measurement times and a more uniform resolution the reflection hemisphere was scanned with a variable azimuthal resolution as a function of scattering angle with 2.0°, 1.0°, and 0.5° steps in ϕ_s and constant 0.25° steps in θ_s direction, respectively. The same brilliant was measured using the CT measurement system at Fraunhofer IOF [209] with a voxel size of 3.1 µm^3 to obtain the gem geometry [210]. To be able to import the cut into the ray tracing software FRED [153], the single facets of the CT measurement had to be fitted with plane surfaces with a CAD software followed by several editing steps [211, 212]. The facets edge were rounded by a changeable radius parameter (see Fig. 4.18). The material was defined as crystalline carbon and for reasons of simplicity to all 57 facets the identical

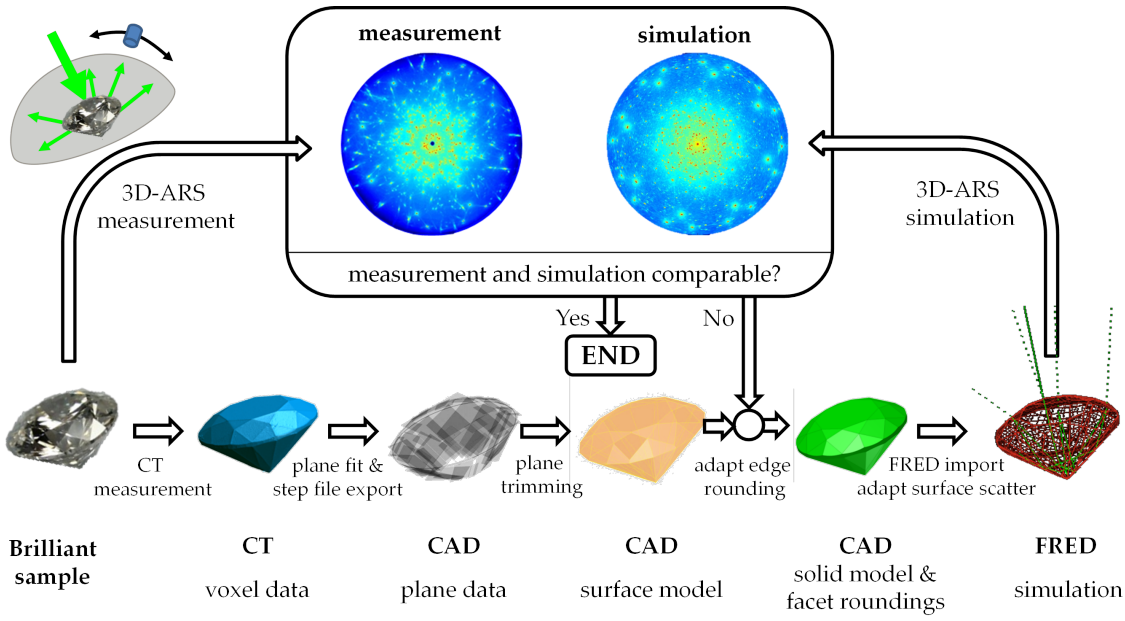

Figure 4.18: Flow chart for data processing.

surface scattering function (3 parameter Harvey model) was attributed. The simulation was performed using 500,000 starting rays, an ancestry depth of 30, and a single scatter event per ray with a maximum of 1000 surface intersections per ray. It was found that increasing those parameters had only a negligible effect, e.g.multiple scattering events per ray (scattered-scattered light [149]) do not have a relevant influence on the optical performance of this cut. This presumably holds for gemstone cuts in general. A directionally resolving detection element was used ("directional analysis entity") with a 0.5° and 1° resolution in polar and azimuthal direction, respectively. To yield ARS, the simulated intensity distribution was normalized to the simulation's incident power and solid angle. The simulation data was moreover convolved with the aperture function according to the experiment.

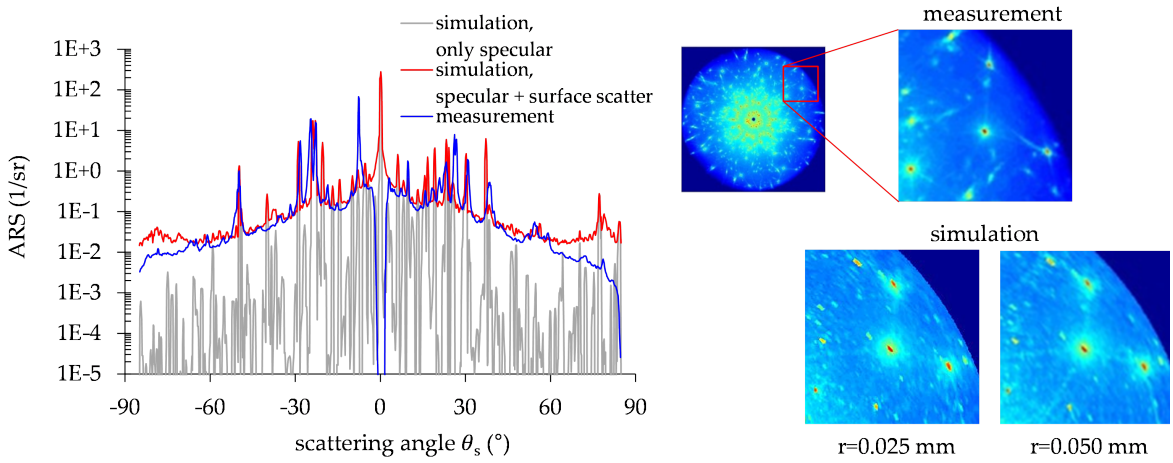

Figure 4.19: Left: adaption of the model ARS function used for the individual facets in the simulation. Right: adaption of the edge rounding radius r.

By comparison of the simulation to the ARS measurement the parameters of the surface scattering model were adapted and the simulation was repeated until a good agreement was

achieved (see Fig. 4.19, left). The same procedure was used to adapt the facets' edge radius, which was found to be a possible origin of the very characteristic lines between the reflections of neighboring facets (see Fig. 4.19, right). However, a later performed analysis showed that the diffraction effects at the facet edges probably dominate the geometrical effect of the facet roundings.

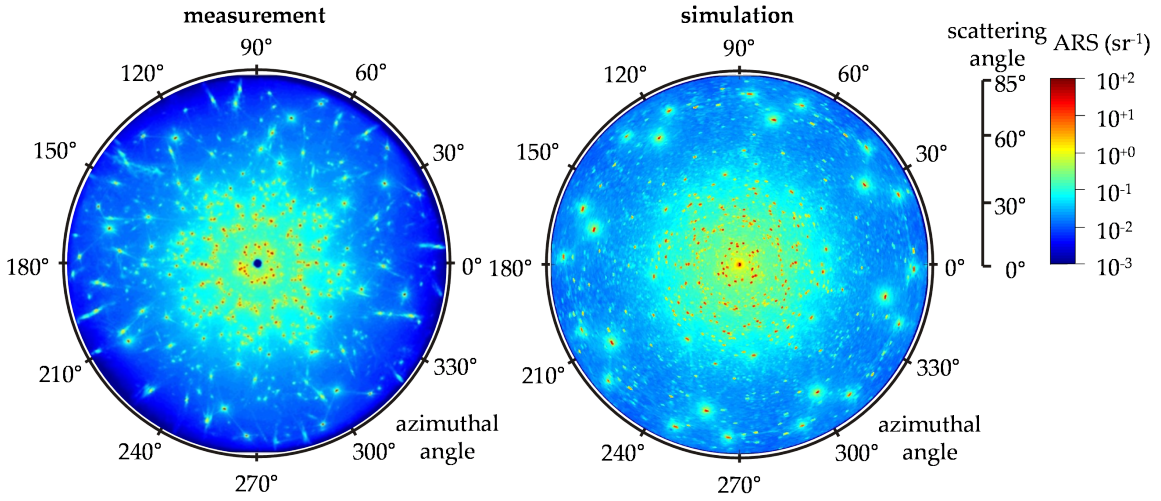

Figure 4.20: Comparison of the measured 3D-ARS to the final ray tracing simulation.

The final result of the ray tracing simulation is shown in Fig. 4.20 along with the 3D-ARS measurement. Although simplified assumptions have been made (same surface roughness at each facet, same rounding radius at all facets' edges, incoherent and unpolarized illumination, no volume scattering, no forward scattering for total internal reflection, no contaminations / inclusions / defects), a good agreement between simulation and measurement was achieved. It is interesting to note that there seems to be some kind of "specular background" in the backscattering hemisphere, which was about 2 to 3 OOM lower than the scattering level (see Fig. 4.19, left, gray solid line). It can be explained by the multiple internal reflections that tend to distribute the specular light. The positions of the specular peaks in simulation and ARS measurement deviate only slightly, mostly only visible at low scattering angles where the peaks result from multiple surface interactions and uncertainties consequently add up. Statistical noise observable in the simulation is a result of the limited number of traced rays, and the simulation seems to be a bit brighter than the measurement. The latter is in the section view (Fig. 4.19) only observable at large scattering angles. This can be attributed to FOV clipping effects, as the table facet was aligned in the center of the scatterometer so that at large scattering angles the back of the brilliant can be vignetted at the receiver's field stop. Also obscuration of the used three finger sample holder are visible in the measurement at large polar scattering angles and at azimuthal angles of 100°, 220°, and 340°. To sum up, a good agreement between simulation and measurement was achieved.

4.3.3 Cut grading by ARS analysis

The performed simulation of the previous subchapter enables to link specific ARS effects to cut grading properties of the different classes.

Shape and proportions

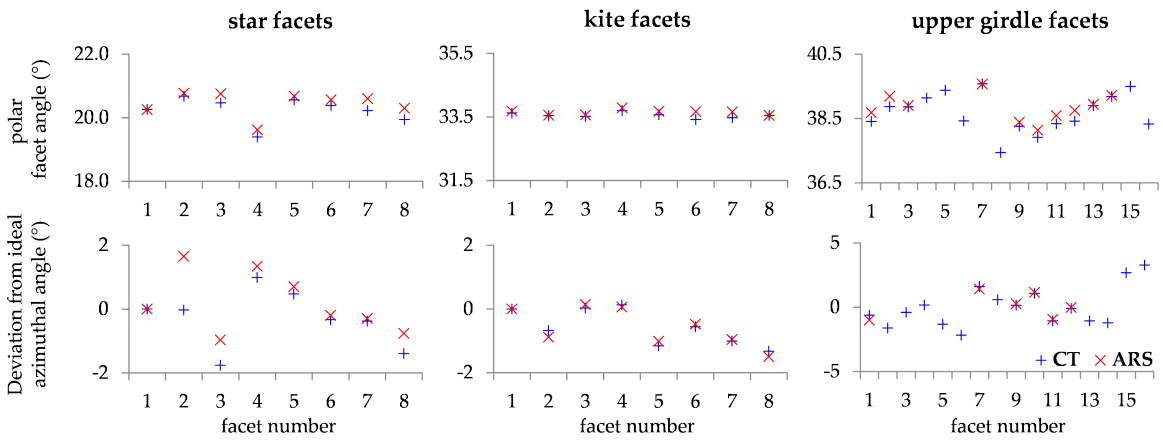

Figure 4.21: Facet angles readout from CT and 3D-ARS data comparison.

When standard round brilliant cuts are graded, the proportions are measured to evaluate design and durability, but in particular to predict the optical performance. Though the optical performance can be accessed directly by light scattering techniques, some proportion parameters can be derived directly from the 3D-ARS. By means of a ray path analysis in FRED the specular peaks in the ARS were linked to individual facets of the gemstone. This allows one to calculate the angular orientation of the facets from the position of the corresponding centroids which is here exemplarily done for the kite, star, and girdle facets of the crown[9]. The result is compared to the performed CT measurement [211] (see Fig. 4.21). Especially the bigger kite facets show a very good agreement between both measurements with rms deviations of 0.09° and 0.13° for the polar and azimuthal angle, respectively. The smaller star and girdle facets show good rms deviations of 0.13° and 0.55°, 0.20° and 0.13° for the polar and azimuth angles, respectively. If these deviations would be exceeded by uncertainties of the light scattering measurement, the reflection law would cause a higher accuracy for the polar facet angles by a factor of 2, which is not the case here. However, facet size plays an important role in the accuracy of fitting planes to the CT measurement. Bigger facets have more data points which increases fitting stability, also measurement artifacts and contamination on the surface have a lesser influence on the result. Facet size does not influence the centroids' locations in the ARS, it is consequently likely that the bigger differences for the smaller kite and girdle facets' angles are CT relatable. However, the achieved agreement is a very good result as comparable commercial cut proportion measurement instruments are specified with angular accuracies between ±0.1° and ±0.2° [196–199], while the required precision for diamond grading was previously estimated to 0.5° and 0.2° for crown and pavilion facets, respectively [201].

By knowledge of the crown facet orientation, it is possible to calculate the angular arrangement of the pavilion facets. As the facets' surface area is represented in the power of the individual reflected peaks, possibly even the complete gem proportions are derivable. Furthermore, angular uncertainties can be decreased by also analyzing the reflections with multiple surface interactions.

[9]The deviation from the ideal azimuth angle of the girdle facets was calculated from the azimuthal difference from one facet to the facet after the next.

Polish

Fig. 4.22 (left) shows simulations where roughness induced scattering of a single facet was either enabled or disabled, while other parameters were left unchanged. As only the near angle scattering around the corresponding reflection changes while the background scattering level is almost unchanged, the ARS functions of individual facets is extractable from 3D-ARS measurements. Hence, surface polish of individual facets could be assessed. Therefore, the background scattering level has to be subtracted from the 3D-ARS and the resulting ARS is scaled to compensate for differing facet sizes and possible illumination beam inhomogeneities:

$$\mathrm{ARS}_{facet}(\phi_{s,facet}, \theta_{s,facet}) = \frac{R(\theta_i)}{\Delta\Omega_s \, \mathrm{ARS}_{specular}} \left[\mathrm{ARS}\left(\phi_s, \theta_s\right) - \mathrm{ARS}_{background}\right] \ , \qquad (4.9)$$

where $\mathrm{ARS}_{specular}$is the ARS value of the specular reflected beam from a facet, $\mathrm{ARS}_{background}$ is the background scattering level, and R the material reflectance at the local angle of incidence. The local scattering angles of the facets ($\phi_{s,facet}$, $\theta_{s,facet}$) are derived by a spherical coordinate transformation. To validate the method, the PSD of a kite facet is calculating form the simulated 3D-ARS. Superposition with scattered light from the facet edges is avoided by extracting the ARS_{facet} data in radial and azimuthal direction only. The background scattering level was derived by averaging the scattering level surrounding the facet reflection with a radius between 6° and 8°. A good agreement of the calculated PSD data to the PSD model that was fed into the simulation was achieved (Fig. 4.22, right). The crossover point between background and near angle scattering of the facet was about $\theta_{s,facet}$=4°.

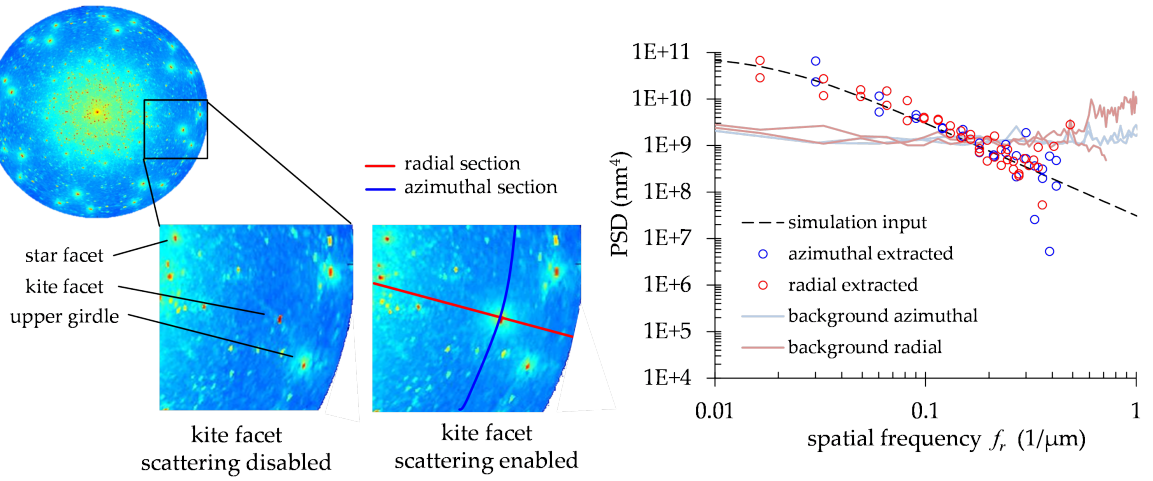

Figure 4.22: Left: simulations where surface scattering of a single facet was enabled and disabled. Right: from the simulated 3D scattering distribution extracted roughness PSD compared to the PSD that was fed into the simulation.

The same procedure was repeated for the experimental ARS, where four representatives of each crown facet group were analyzed (see 4.23 right). However, the PSDs calculated from WLI measurements [213] show only a partial agreement. Hence, a wavelength scaling experiment as described in chapter 4.2 was performed for a kite facet atλ=405 nm, 532 nm, and 640 nm. As the PSDs derived from the ARS experiments performed at different illumination wavelengths do not overlap, the presence of another light scattering source is identified, probably contamination. However, the simulation showed that the proposed approach can be used to derive surface roughness representing PSD functions of the individual facets.

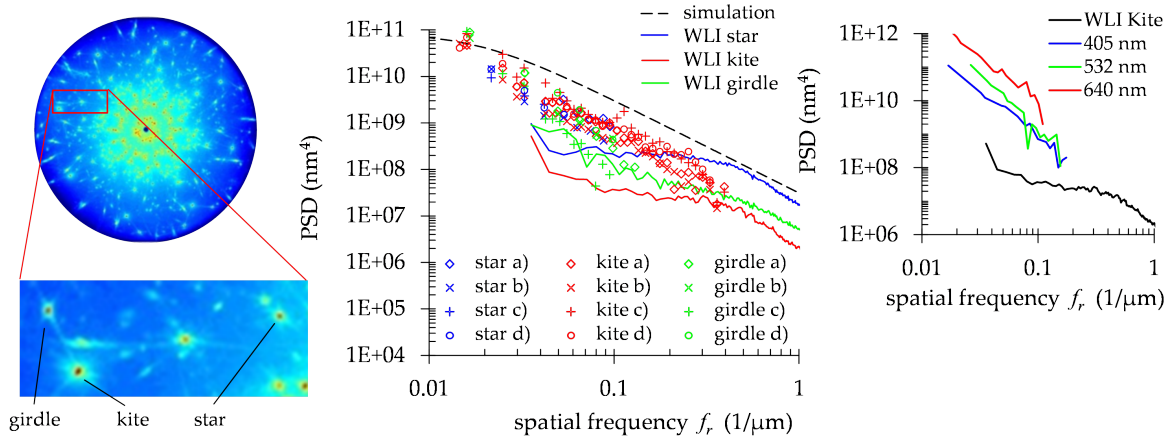

Figure 4.23: Left: near angle scattering around different facets in the measurement. Center: PSDs derived from the 3D-ARS compared to WLI [213] and the corresponding PSD used in the simulation for all facets. Right: PSDs of a kite facet calculated from ARS measurements performed at different λ.

Symmetry

As the facet geometry is precisely represented in the 3D-ARS, a cut symmetry analysis by light scattering measurements is possible. Fig. 4.24 shows an ARS measurement in the reflection hemisphere of two different diamond cuts. The left is the same brilliant already analyzed in this section, which was acquired from a jeweler [214]; the ARS on the right represents a high quality cut of a diamond provided by Swarovski KG [215] with 0.71 carat and a girdle diameter of about 5.7 mm.
The high quality cut has a visibly lower background ARS level compared to the standard cut, which indicates a smoother facet polish. Regarding cut symmetry, the first impression already indicates the much more symmetric ARS of the special cut. However, to get a more objective measure, an empirical algorithm based on the azimuthal autocorrelation of the 3D-ARS was developed in this work to evaluate cuts for specific rotational symmetries. The developed algorithm was tested on a small set of different gemstones by the author [170] and is described in the following.

Before the autocorrelation function $ACF(\phi_s, \theta_s)$ is calculated separately for each scattering angle, the ARS is smoothed to ARS_{filt} by means of a Gaussian filter to be more "forgiving" to small symmetry deviations:

$$ACF(\phi_s, \theta_s) = \frac{1}{2\pi} \int_0^{2\pi} ARS_{filt}\,(\phi_s, \theta_s)\, ARS_{filt}\,(\phi_s + \varphi, \theta_s)\, d\phi_s \ . \tag{4.10}$$

Practically, the lag φ is chosen as the azimuthal receiver step length. Afterwards, the ACF is normalized with $ACF_N(\phi_s, \theta_s) = ACF(\phi_s, \theta_s)/ACF(0, \theta_s)$ and averaged over θ_s between the minimum and maximum scattering angles θ_{min} and θ_{max}, respectively:

$$ACF_{N,mean}(\phi_s) = \frac{1}{\theta_{max} - \theta_{min}} \int_{\theta_{min}}^{\theta_{max}} ACF_N(\phi_s, \theta_s) d\theta_s \, . \tag{4.11}$$

The symmetry function $g_{sym}(N_{sym})$ over the symmetry orders[10] N_{sym} is calculated by averaging $ACF_{N,mean}(\phi_s)$ at the symmetry relevant locations of ϕ_s and normalizing to its mean value $\mu_{ACF_{N,mean}}$:

$$g_{sym}(N_{sym}) = \frac{1}{\mu_{ACF_{N,mean}}} \sum_{i=1}^{N_{sym}-1} \frac{1}{N_{sym}-1} ACF_{N,mean}(i\frac{2\pi}{N_{sym}}) \,. \tag{4.12}$$

It is plotted for the two brilliant cuts in Fig. 4.24 on the upper left. It clearly shows dominating symmetries of 2nd, 4th, 8th, and 16th order for both diamonds, while the high quality cut exhibits higher symmetries. To yield a simple symmetry factor for brilliant cuts, $g_{sym}(N_{sym})$ is averaged at the most important symmetries order N_{sym}=8 and 16. In Fig. 4.24 the brilliant on the left achieved a symmetry factor of $g_{sym,8/16}$=1.089, while the brilliant on the right yielded $g_{sym,8/16}$=1.592.

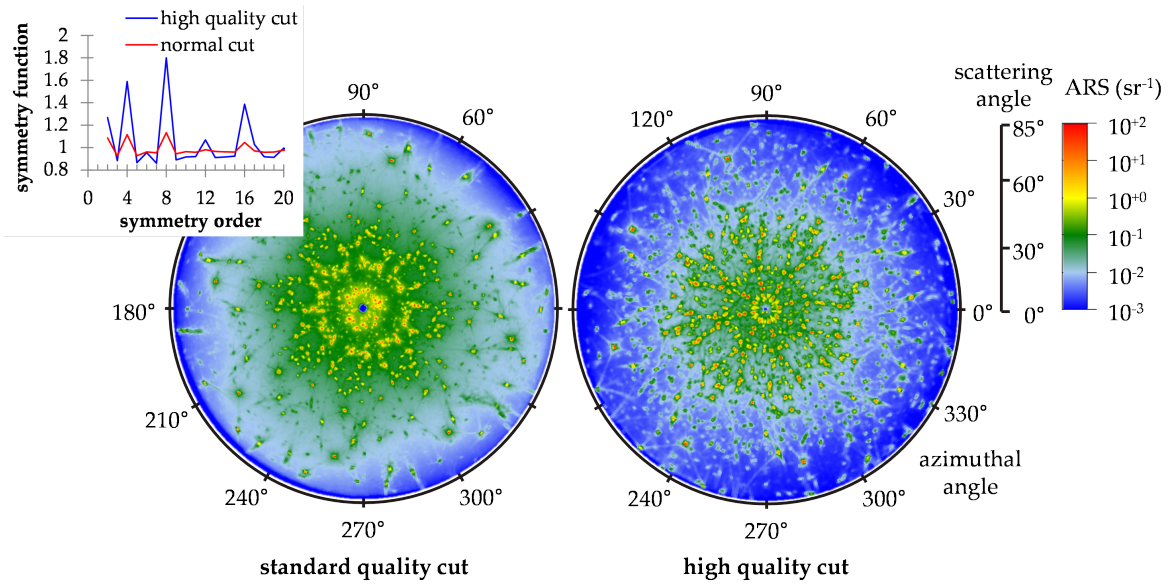

Figure 4.24: Symmetry analysis of two different brilliant cuts by means of a symmetry function (upper left graph).

Optical Performance

Different metrics to calculate grading factors for brightness, fire, and scintillation from specular reflection distributions are already published. The analysis presented in here is therefore focussed to study the effect of light scattering on the optical performance of gemstone cuts. The same brilliant described at the beginning of this section is compared to a zirconia with a diameter of about 5 mm. To be able to characterize also dispersion effects, ARS measurements covering the reflection hemisphere were performed at illumination wavelengths of 405 nm, 532 nm, and 640 nm on both gemstones. The scan resolution was 0.5° using the sampling mentioned earlier in chapter 4.3.2. Afterwards, the three ARS measurements were superimposed to yield an RGB image of the diamond's and the zircon's light scattering distribution, respectively (see Fig. 4.25).

[10] The symmetry order N_{sym} corresponds to an N_{sym} -fold symmetry. Hence, a symmetry order of 3 equals a rotational or cyclic eigensymmetry of 120° (e.g. equal-sided triangle).

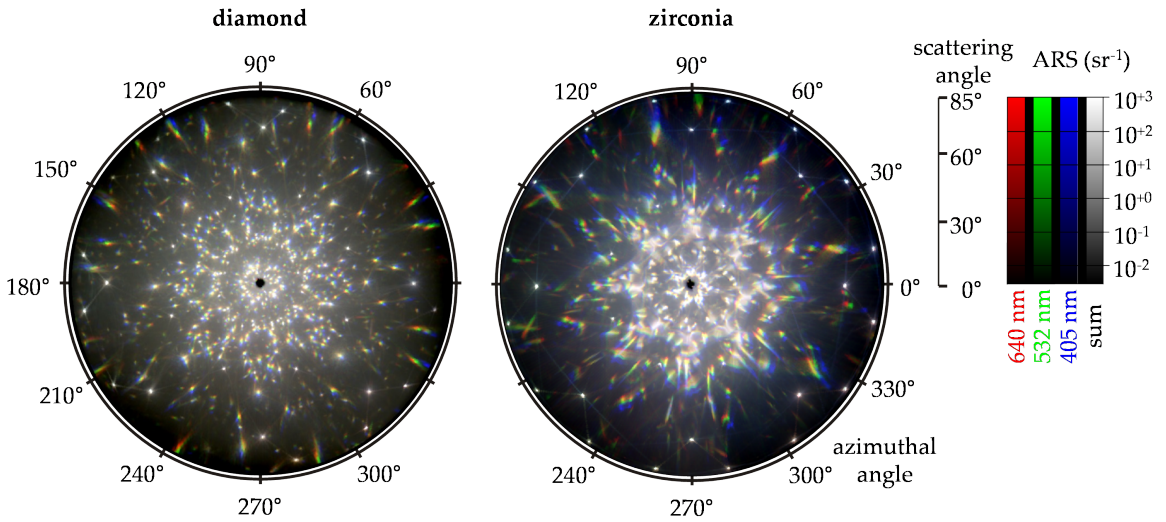

Figure 4.25: Measured 3D-ARS at three wavelengths of a diamond and a zirconia. The 3D-ARS were measured for each gemstone with the table top system at illumination wavelengths of 405 nm, 532 nm, and 640 nm. The 3D-ARS at the according wavelengths were afterwards combined to yield an RGB image where ARS levels of $3 \cdot 10^{-03}$ sr^{-1} to 10^{+02} sr^{-1} equal the minimum and maximum value of the corresponding colors.

The specular reflections at the crown facets can be easily identified by the bright white dots. Reflection from the pavilion facets in contrast have traveled one or multiple times through the gemstone and are consequently dispersed and identifiable by rainbow colors.

Brightness, fire, and scintillation can now be assessed in the 3D-ARS:

1. *Brightness* $\mathcal{B}$ can be evaluated (see chapter 4.3.1) by determining the backward redistributed power subtracted by glare. Following this definition, brightness can be derived from 3D-ARS measurements by calculating TS_b and subtracting the glare constant R_{glare}. Strictly speaking, the power that is actually lost by light scattering in the reflection hemisphere would consequently still contribute to $\mathcal{B}$. Yet, the background scattering loss $TS_{b,BG}$ is nevertheless subtracted from TS_b as it corresponds to power that is drawn from the specular reflections:

$$\mathcal{B} = TS_b - R_{glare} - TS_{b,BG}\,. \tag{4.13}$$

   The background scattering ARS is determined by calculating the minimum ARS value as a function of polar angle (see Fig. 4.26 left), its integrand yields $TS_{b,BG}$. Both cuts receive most of the redistributed power from scattering angles between 15° and 45° (see Fig. 4.26 center). All integrations were performed between θ_s=2° and 85° polar angle. As the specular reflection of the table facet was not detected in the ARS measurement, glare R_{glare} was determined accordingly without the table facet contribution from ray tracing simulations. The diamond and the zirconia cut yield, averaged over the three illumination wavelengths, a brightness of $\mathcal{B}$=53.7% and 50.9%, respectively. 22% and 24.9% of the incident power is lost in the transmission hemisphere by forward scattering and light leakage through the pavilion, respectively. Comparing this to an idealized Tolkowski cut (no light scattering losses) with 74% brightness and 9% specular transmitted power loss shows that both gemstones do not achieve a good brightness value.

Table 4.2: Power contributions to glare, scattering loss, and brightness of the diamond and zirconia cuts.

	diamond				zirconia			
λ(nm)	TS_b	R_{glare}	$TS_{b,BG}$	$\mathcal{B}$	TS_b	R_{glare}	$TS_{b,BG}$	$\mathcal{B}$
405	69.9%	12.7%	10.5%	46.7%	74.5%	10.3%	18.1%	46.1%
532	80.2%	12.4%	12.3%	55.5%	71.9%	9.8%	13.1%	49.0%
640	84.0%	12.2%	12.8%	59.0%	79.3%	9.6%	12.0%	57.7%

However, brightness is underestimated for the diamond cut, as some of the specular reflections were obscured by the sample holder.
Considering that brightness of quality brilliant cuts differs only within a few percents, light scattering can obviously lead to surprisingly high power losses in gemstones of over 10% and consequently has an up to now unnoticed impact on brightness! The high impact can be explained by the typically high number of surface interactions per traced ray, which causes the individual facets to contribute light scattering multiple times. This was also observed in the performed simulation, where the background scattering level is approximately 10 times higher than the ARS of the individual facets! Small optimizations of the contributing light scattering sources accordingly allow a remarkable optimization of brightness.

Table 4.3: Wavelength scaling of the normalized scattering loss values of the diamond and zirconia

	$TS_{b,BG}/TS_b$	
λ(nm)	diamond	zirconia
405	15.1%	24.3%
532	15.3%	18.2%
640	15.3%	15.2%

Regarding wavelength scaling properties (see table 4.2), the TIS corresponding property $TS_{b,BG}/TS_b$ is evaluated to compensate cut design effects for the different λ. It grows for the zirconia nearly perfectly linear with λ^{-1} , while the diamonds features an almost constant scattering contribution of about 15%. Topographic scattering loss would ideally scale with λ^{-2}. Hence, surface scattering of the brilliant is superimposed by a light scattering source with almost no wavelength scaling properties, which again hints to contamination. It also explains the overestimation of the ARS in the raytracing simulation. Interestingly, the TS_b value of the diamond drops for 405 nm illumination, which could indicate fluorescence losses.

2. *Scintillation* effects are recognizable in the 3D-ARS by the various, distinct, and separable reflection peaks which cause sparkling effects and changes in the virtual facet pattern, and are visually much more present in the diamond. In contrary, the reflections of the zirconia are, especially at scattering angles smaller than 45°, of larger size and tend to overlap. Hence, if the gemstones are tilted and viewed face-up, the pattern in the crown of the brilliant changes significantly faster. The contrast between background scattering level and the maximum ARS level (see Fig. 4.26 left) is approximately 2.5 to 3 OOM for the diamond. The lower contrast of the zirconia of 2 OOM is a result

of the larger size of the reflection peaks. For the diamond cut, the scintillations are very pronounced between θ_s=15° and 45° with the highest contribution to brightness. As the maximum observable contrast in a gemstone cuts (under typical lighting conditions) was determined to be 3.5 OOM [207][11], the contrast reduction of the scintillations caused by the background scattering level can be subjectively perceived.

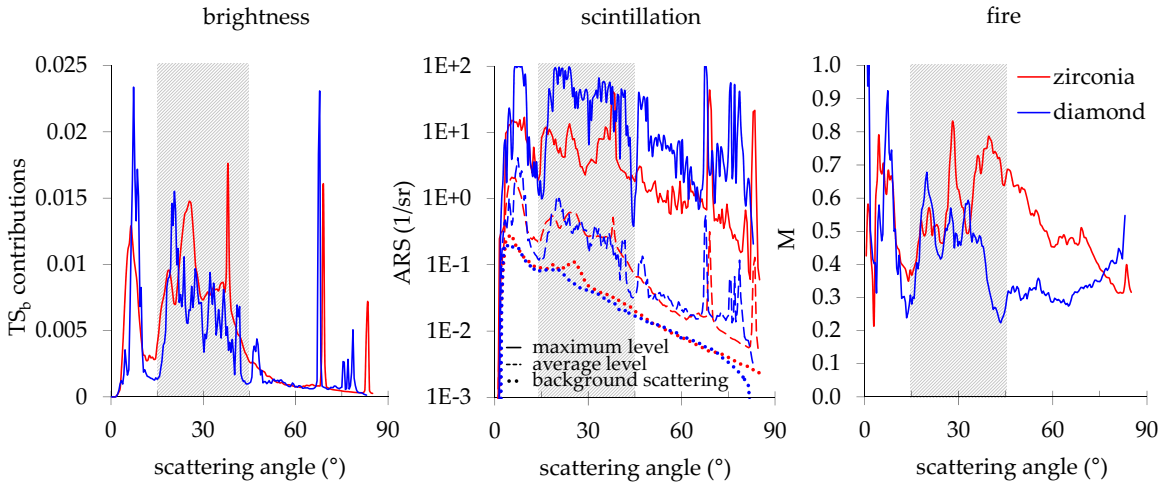

Figure 4.26: ARS analysis of the optical perfomance of the diamond and the zirconia cut: brightness is analyzed by the contribution to the redistributed power TS_b (left), scintillation by the dynamic range in the ARS (center), and fire by the contrast M between the ARS with 405 nm and 640 nm illumination (right).

3. As *fire* is related to dispersion effects, the higher dispersion of the zirconia results in wider spreaded colored flares. Fire is evaluated here by calculating the Michelson contrast $M = |ARS_{405\,nm} - ARS_{640\,nm}| \,/\, (ARS_{405\,nm} + ARS_{640\,nm})$ between the 3D-ARS at λ=405 nm and 640 nm (see Fig. 4.26 right). The contrast of the zirconia cut exceeds the contrast of diamond particularly at polar angles higher than 40°, where the contribution to brightness is decreased. Also, because of the more differently pronounced scintillations, the fire flashes change faster and brighter for the diamond. Though, the probability of perceiving a colored virtual facet is higher for the zirconia cut, as the colored flares are much more extended.

4.3.4 Summary

It was shown that light scattering techniques represent an alternative and comprehensive tool for characterizing gemstones regarding all cut grading relevant criteria of diamonds. The investigations were based on a ray tracing simulation that was compared to a 3D-ARS measurement of the same brilliant to give a more profound understanding of the light scattering mechanisms inside a diamond cut. It could be shown that the background scattering level is approximately 10 times higher than the ARS of the individual facets, which could be explained by an increase of the effective incident power per facet caused by the multiple surface interactions per traced ray. In contrary, it could be shown that multiple scattering

[11] The observable contrast was originally determined for chromatic flares [207]. The maximum observable contrast for white reflections peaks is probably even higher.

(scattered-scattered light) has no effect on the optical performance of diamond cuts and probably gemstones in general. From a ray path analysis it was possible to link particular specular peaks in the ARS to individual facets. This allowed to calculate the angular facet alignment from the ARS distribution, which was related to CT based results with good agreement.
It was shown that the polish of individual facets can be assessed by calculating PSD functions from the near angle scattering that surrounds the corresponding reflection peaks. However, according experiments revealed contamination on the facets.
Cut symmetry analysis was performed by means of the developed symmetry function based on the azimuthal autocovariance.
The optical performance relevant characteristics "brightness", "fire", and "scintillation" were firstly examined with respect to light scattering effects by 3D-ARS measurements performed at three wavelengths for a diamond and a zirconia cut, respectively. It could be shown that light scattering losses reduced brightness in the analyzed brilliant cut by a surprisingly high amount of more than 10%.

Future works are dedicated to a more detailed simulation considering the different surface scattering contributions of the individual facets, as well as including other sources of light scattering. A gemstone cut characterization at larger θ_i is also planned.

5 Summary

As a consequence of the drastically increased interest in high-end optical components that arose in the last decade, the need for sensitive, fast, and flexible measurement tools gained importance. Light scattering techniques were found to be a suitable, versatile, and valuable metrology method. The lack of compact, yet comprehensive tools motivated this thesis to develop a highly universal instrument for light scattering measurement.

The scatterometer described in this thesis exhibits high sensitivity with full 3D spherical detection yet with a compact table top layout. A concept was introduced to provide capability for wavelength and polarization multiplexed ARS measurements.

The illumination system is completely integrated into the instrument and based on three laser sources providing the wavelengths λ=405 nm, λ=532 nm, and λ=640 nm. The system achieves Rayleigh limited sensitivity, resulting from the scattering at the air molecules. The dynamic range surpasses 14 orders of magnitude. This provides capability for the characterization of even superpolished transparent substrates up to rough technical surfaces.

The size of the whole instrument (including housing) is smaller than 0.8 m x 0.8 m x 0.8 m with a total weight of about 75 kg (without top cover), enabling the operation close to fabrication processes. The compact layout was achieved by a specific arrangement of the axes where the optical path lengths are artificially increased by the implementation of beam folding mirrors in the illumination and the detection system.

A model was proposed to analytically predict the near angle signature of scatterometers caused by scattered light arising from the optical components. Verification was performed by comparing the measured instrument signature to the modeled signature (based on topographic measurements) and to ray tracing simulations with good agreement. This allows the identification of optical components that dominate the instrument signature. The according components were substituted by mirrors with better performance in the corresponding spatial frequency range.
Light scattering caused by roughness growth in optical coatings was found to have no effect on the near angle signature. It could be shown that an additional periscope mirror in front of the detector improves the near angle signature.
A specular near angle signature of θ_s=0.14° was achieved, which, through beam propagation simulations and experiments, was found to be limited by surface irregularities.

To derive the measurement uncertainty of the instrument, a model was developed by a combination of both error propagation and Monte-Carlo analysis. It was used to determine misalignment effects by simulating procedures used for sample and instrument alignment. Accordingly, the overall measurement uncertainty of the table top instrument for the ARS of a specular sample was determined to range between 2% and 20% for $\theta_s < 80°$, while for scattering angles of about 5° around the specular beam uncertainty can rise up to about 100%.

It was found that the high uncertainties at small and large scattering angles are typically dominated by misalignment effects. It was however shown that these misalignment effects of the system and sample can be compensated to a large extent by implementing an automated positioner for readjustments of the detector aperture. Furthermore, a small out-of-plane illumination angle (to avoid detector obscuration) has no relevant effect on the measurement uncertainty. Positioning uncertainties of θ_i and θ_s were found to be especially critical because the system and sample alignment procedures usually rely on the accuracy of these axes. A recommendation for the accuracies of the positioners of 0.01° was derived for θ_i and θ_s. Accuracies of 0.1° should be avoided as they cause misalignment to dominate the combined measurement uncertainty at all scattering angles.

A novel concept was introduced that firstly allows to perform polarization and / or wavelength multiplexed light scattering measurements over the complete dynamic range and with high sensitivity. Parallel ARS measurements pose a specific challenge to the required crosstalk specifications because of the possibly extreme dynamic range between the channels. This is especially the case for λ multiplexed grating samples. Hence, a concept based on frequency division multiplexing was developed. The required crosstalk was achieved by a combination of electronic prefiltering, demodulation optimization, and optical adaption.
The concept was verified by parallel ARS measurements performed at three illumination wavelengths (405 nm, 532 nm, and 640 nm) on a polished Nickel coated surface. Compared to sequentially performed measurements, small rms deviations with an average of only <8% for all channels were demonstrated.

To characterize the individual roughness components of UP surfaces, a new anisotropy analysis procedure was introduced that allows the separation of different roughness components by a spatial frequency discrimination in the 2D-PSD. In contrast to previously published methods, this analysis is spatial frequency resolving and directly linked to the optical and roughness properties. It also provides a general degree of isotropy $a_{iso}(f_r)$ and allows its evaluation as a function of illumination wavelength $\bar{a}_{iso}(\lambda)$, where the anisotropically scattered light contributes to TS with $1 - \bar{a}_{iso}(\lambda)$. The change of the anisotropy with λ was demonstrated by means of a coated anisotropic glass substrate. The proposed method is especially useful to generally characterize anisotropy and roughness with regard to application.

It was demonstrated that 2D-PSD functions of anisotropic surfaces are beneficially derived by 3D-ARS measurement instead of WLI and AFM measurements. Therefore, a direct comparison of calculated 2D-master PSDs from topographic and light scattering measurements was performed: The directional rms roughness and the 2D-*iso* PSD calculated from both 2D-master PSDs showed good agreement. However, the original 2D-master PSDs deviated averagely by half an order of magnitude. The deviations were to a large extend attributed to artifacts and statistical fluctuations in the topographic measurements.

The individual roughness components of different UP diamond turned surfaces were analyzed and discussed using the proposed method. It was found that the spatial frequency dependence of different superimposed roughness components (1D, 2D-isotropic, 2D-anisotropic) are of fundamental interest to the previously conceived [18] spatial frequency dependent nature of anisotropy. Chatter marks were observed to be capable of completely superimposing the isotropic background of diamond turned surfaces. Under this assumption, chatter would

contribute about 50% to the total rms-roughness. This is in contradiction to an earlier publication [92] where the random roughness was found to be the typical dominating component. However, the roughness introduced by chatter marks were not investigated by this author. It was demonstrated that the time frequency of a vibration source in the machining process can be determined by 3D-ARS measurements of chatter marks.

The instrument was utilized to analyze the wavelength scaling of optical coatings and substrates in order to identify surface roughness, roughness growth, and contamination. This analysis was based on the capability of the scatterometer to quickly provide highly correlated ARS measurements at different λ. Highly-correctable wavelength scaling experiments are especially crucial for samples with low homogeneity, which is the case for surfaces with contaminations or defects.
The "wavelength scaling" assumption for opaque topographic scattering samples made in [177] was confirmed: If PSD functions derived from ARS measurements with different λ overlap they represent the topography. Beyond these findings, wavelength scaling analysis following the smooth / single surface approximation was found to yield surface representative PSD functions even for interference coatings and / or contaminated samples. Therefore, the overlap is analyzed as a function of spatial frequency rather than analyzing the deviation of the integrand $\sigma(\lambda)$ [178]. It was shown that the PSDs represent the interface roughness in regions of f_r where they overlap. This holds although they might significantly deviate in other regions of f_r. WLI and AFM measurements were used to verify the analysis.
The described procedure allows conducting a very reliable post-measurement analysis, as possible user related measurement errors or sample related inappropriate smooth or single surface assumptions become quickly evident. Moreover, wavelength scaling is advantageously sensitive to only (optically) relevant roughness growth effects as well as only (optically) relevant contaminations.
It was demonstrated that a three wavelength analysis of a clean Al / SiO_2 coating allows to determine the layer thickness as well as the PSD functions of the top and intermediate layer. Post measurement analysis was performed by means of model PSD functions and by evaluating a merit function. The derived PSDs showed good agreement to topographic measurements.

The presented measurement system was also shown to offer an alternative and comprehensive tool for characterizing gemstones regarding all cut grading relevant criteria of diamonds. The investigations made were based on ray tracing simulations which were compared to a 3D-ARS measurement of the same brilliant. Light scattering was demonstrated to have a surprisingly large impact on the optical performance. This could be explained by TIR effects which result in a high number of surface (facet) interactions per ray. The scattering loss of a brilliant results to be approximately 10 times higher than the corresponding ARS level of the individual facets. In contrast, multiple scattering (scattered-scattered light) was shown to have no effect on the optical performance of diamond cuts and probably gemstones in general.

It was demonstrated that the polish of individual facets can be assessed by calculating PSD functions from the near angle scattering that surrounds the corresponding reflection peaks. ARS analysis consequently constitutes the first published measurement technique that allows

to effectively evaluate facet polish. However, comparing experimentally derived PSDs to WLI measurements showed deviations that were attributed to contamination.

Cut symmetry was analyzed by means of a developed symmetry function based on the azimuthal autocovariance. The angular facet alignment of a brilliant was determined from the 3D-ARS distribution by evaluating the position of the specular reflected beams, which was compared to CT based results with good agreement.

The optical performance relevant characteristics "brightness", "fire", and "scintillation" were firstly examined with respect to light scattering effects. Therefore, 3D-ARS measurements were performed at three wavelengths for a diamond and a zirconia cut, respectively. The brightness in the brilliant cut was found to be reduced by scattering losses by more than 10%. The presence of contamination on the facets or inclusions inside the diamond was detected by a wavelength scaling analysis.

It was shown that the specifications of the developed instrument enable a large variety of applications: from the analysis of low scattering optical coatings and their substrates, over the characterization of anisotropic roughness components of diamond turned surfaces, up to the assessment of gemstone cuts. By now, the instrument is being used successfully in different laboratories and for different applications at The Scatter Works, Inc. (Tucson, Arizona) [216], ESA ESTEC (Nordwijk, Netherlands) [217], Technische Universität Ilmenau (Ilmenau, Germany) [218], and Swarovski KG (Wattens, Austria) [219].

Future work will be dedicated to the implementation of an automatically switchable detector aperture, which is moreover aligned onto the specular beam by the software to reduce measurement uncertainties (as predicted in chapter. 3.6.3). Optics in the illumination system will be replaced by optics with lower surface irregularities to improve the beam profile. Furthermore, to extend the dynamic range of the multiplexing concept additional filters will be implemented to enable optical adaption (see chapt. 3.5.2). Additional experiments will be conducted to study the influence of different process parameters on chatter marks. A more detailed simulation (including volume scatter) and 3D-ARS analysis of different diamond cuts will be performed and compared to give a more profound understanding of the effect of light scattering on the optical performance.

Bibliography

[1] P. P. Debye, "A Photoelectric Instrument for Light Scattering Measurements and a Differential Refractometer," J. Appl. Phys. **17**, 392–398 (1946).

[2] B. H. Zimm, "Apparatus and Methods for Measurement and Interpretation of the Angular Variation of Light Scattering; Preliminary Results on Polystyrene Solutions," J. Chem. Phys. **16**, 1099–1116 (1948).

[3] J. C. Stover, *Optical scattering: Measurement and analysis*, 3rd ed. (SPIE Press, Bellingham, Wash., 2012).

[4] H. E. Bennett and J. O. Porteus, "Relation Between Surface Roughness and Specular Reflectance at Normal Incidence," J. Opt. Soc. Am. **51**, 123–129 (1961).

[5] P. Beckmann and A. Spizzichino, *The Scattering of Electromagnetic Waves from Rough Surfaces* (Pergamon, New York, 1963).

[6] E. L. Church and J. M. Zavada, "Residual surface roughness of diamond-turned optics," Appl. Opt. **14**, 1788–1795 (1975).

[7] J. C. Stover, "Scatterometers," in "Handbook of Optics," , vol. 2, M. Bass, ed. (McGraw-Hill New York, 1995), chap. 26, pp. 26.1–26.16, 2nd ed.

[8] J. C. Stover, "Roughness characterization of smooth machined surfaces by light scattering." Appl. Opt. **14**, 1796–1802 (1975).

[9] J. Harvey, "Light-scattering characteristics of optical surfaces," Ph.D. thesis, University of Arizona (1976).

[10] P. C. Archibald and H. E. Bennett, "Scattering from infrared missile domes," Proc. SPIE **0133**, 71–77 (1978).

[11] J. Elson, V. Rehn, J. Bennett, and V. Jones, "Measurement of angle resolved light scattering from optical surfaces in the 75 to 750 eV range," Proc. SPIE **315**, 193–201 (1981).

[12] D. Cheever, F. Cady, K. A. Klicker, and J. Stover, "Design review of a unique complete angle-scatter instrument (CASI)," Proc. SPIE **818**, 13–20 (1987).

[13] Lambda Research Corp., ed., *product information Complete Angle Scatter Instrument (CASI)*, http://www.lambdares.com, last visited: December 03, 2013.

[14] J. C. Stover, *Optical scattering: Measurement and analysis*, 1st ed. (McGraw-Hill, New York, 1990).

[15] R. D. Jacobson, S. R. Wilson, G. A. Al-Jumaily, J. R. McNeil, J. M. Bennett, and L. Mattsson, "Microstructure characterization by angle-resolved scatter and comparison to measurements made by other techniques," Appl. Opt. **31**, 1426–1435 (1992).

[16] A. Duparré, J. Ferre-Borrull, S. Gliech, G. Notni, J. Steinert, and J. M. Bennett, "Surface characterization techniques for determining the root-mean-square roughness and power spectral densities of optical components." Appl. Opt. **41**, 154–71 (2002).

[17] A. Duparré, "Light scattering techniques for the inspection of microcomponents and microstructures," in "Optical Methods for the Inspection of Microsystems," , W. Osten, ed. (Taylor & Francis, 2006), chap. 3, pp. 103–119.

[18] C. Amra, D. Torricini, and P. Roche, "Multiwavelength (0.45-10.6 μm) angle-resolved scatterometer or how to extend the optical window," Appl. Opt. **32**, 5462–5474 (1993).

[19] T. A. Germer and C. Asmail, "Goniometric optical scatter instrument for out-of-plane ellipsometry measurements," Rev. Sci. Instrum. **70**, 3688–3695 (1999).

[20] P. Kadkhoda, H. Madebach, and D. Ristau, "Angle resolved scatter measurements on optical components," Proc. SPIE **5965**, 59651A (2005).

[21] J. D. Paumi, "Laser vs. camera inspection in the paper industry," Tappi J. **71**, 129–135 (1988).

[22] G. J. Ward, "Measuring and modeling of anisotropic reflection," SIGGRAPH Comput. Graph. **26**, 265–272 (1992).

[23] G. Mulholland, T. Germer, and J. Stover, "Modeling, Measurement, and Standards for Wafer Inspection," in "Proc. of the Government Microcircuits Application and Critical Technologies Conference (GOMAC) 2003 Tampa, Florida," (2003).

[24] J. C. Stover, "A review of emerging SEMI standards for particle scanners," Proc. SPIE **5188**, 162–168 (2003).

[25] F. M. Cady, J. C. Stover, D. R. Bjork, M. L. Bernt, M. W. Knighton, D. J. Wilson, and D. R. Cheever, "A design review of a multiwavelength, three-dimensional scatterometer," Proc. SPIE **1331**, 201–208 (1990).

[26] C. Asmail, C. L. Cromer, J. E. Proctor, J. J. Hsia, and R. P. Division, "Instrumentation at the National Institute of Standards and Technology for bidirectional reflectance distribution function (BRDF) measurements," Proc. SPIE **2260**, 52–61 (1994).

[27] S. Schröder, T. Herffurth, H. Blaschke, and A. Duparré, "Angle-resolved scattering: an effective method for characterizing thin-film coatings," Appl. Opt. **50**, C164–C171 (2011).

[28] D. R. White, P. Saunders, S. J. Bonsey, J. V. D. Ven, and H. Edgar, "Reflectometer for measuring the bidirectional reflectance of rough surfaces," Appl. Opt. **37**, 3450–3454 (1998).

[29] Light Tec Espace, ed., *product information Reflet*, http://www.lighttec.fr, last visited: December 03, 2013.

[30] ASTM E2387-05, "Standard practice for goniometric optical scatter measurements," (2011).

[31] J. Elson and J. Bennett, "Vector scattering theory," Opt. Eng. **18**, 116–124 (1979).

[32] F. E. Nicodemus, J. C. Richmond, J. Hsia, I. W. Ginsberg, and T. Limperis, "Geometrical Considerations and Nomenclature for Reflectance," NBS Monograph **160**, 1–8 (1977).

[33] ASTM E1392-1990, "Standard practice for angle resolved optical scatter measuremts on specular or diffuse surfaces," (1990).

[34] T. A. Leonhard and P. Rudolph, "BRDF round robin test of ASTM E 1392," Proc. SPIE **1995**, 285–293 (1993).

[35] SEMI ME1392-1109, "Guide for angle resolved optical scatter measurements on specular or diffuse surfaces," (2009).

[36] S. Schröder and A. Duparré, "Measurement of light scattering, transmittance, and reflectance," in "Laser-induced damage in optical materials," , D. Ristau, ed. (Taylor & Francis, Boca Raton, 2014, to be published).

[37] ISO/IEC 17025:2005, "General requirements for the competence of testing and calibration laboratories," (2005).

[38] ISO 13696:2002, "Optics and optical instruments - test methods for radiation scattered by optical components," (2002).

[39] J. M. Bennett and L. Mattsson, *Introduction to Surface Roughness and Scattering*, 2nd ed. (Optical Society of America, Washington, D.C., 1991).

[40] H. E. Bennett, "Scattering characteristics of optical materials," Opt. Eng. **17**, 480–488 (1978).

[41] L. Mattsson, "Characterization of supersmooth surfaces by light scattering techniques," Proc. SPIE **1009**, 165–171 (1989).

[42] D. Rönnow and E. Veszelei, "Design review of an instrument for spectroscopic total integrated light scattering measurements in the visible wavelength region," Rev. Sci. Instrum. **65**, 327–334 (1994).

[43] P. Kadkhoda, D. Ristau, and F. von Alvensleben, "Total scatter measurements in the DUV/VUV," Proc. SPIE **3578**, 544–554 (1999).

[44] P. Kadkhoda, A. Müller, and D. Ristau, "International Round-Robin Experiment to Test the International Organization for Standardization Total-Scattering Draft Standard," Appl. Opt. **39**, 3321–3332 (2000).

[45] S. Gliech, J. Steinert, and A. Duparré, "Light-scattering measurements of optical thin-film components at 157 and 193 nm," Appl. Opt. **41**, 3224–35 (2002).

[46] S. Gliech, "Entwicklung und Anwendung eines Messsystems zur Bestimmung des totalen Streulichts von optischen und technisch rauhen Oberflächen und Schichten," Ph.D. thesis, Technische Universität Ilmenau (2003).

[47] D. Rönnow and A. Roos, "Correction factors for reflectance and transmittance measurements of scattering samples in focusing coblentz spheres and integrating spheres," Rev. Sci. Instrum. **66**, 2411–2422 (1995).

[48] T. Schiff, "Method and system for segmented scatter measurement," Patent US 6,078,391 (2000).

[49] B. A. Brice, M. Halwer, and R. Speiser, "Photoelectric Light-Scattering Photometer for Determining High Molecular Weights," J. Opt. Soc. Am. **18**, 768–778 (1950).

[50] S. Schröder, "Light scattering of optical components at 193 nm and 13.5 nm," Ph.D. thesis, Friedrich-Schiller Universität Jena (2008).

[51] M. Wurm, F. Pilarski, and B. Bodermann, "A new flexible scatterometer for critical dimension metrology," Rev. Sci. Instrum. **81**, 023701 (2010).

[52] T. M. Bloomstein, D. E. Hardy, L. Gomez, and M. Rothschild, "Angle Resolved Scattering Measurements of Polished Surfaces and Optical Coatings at 157 nm," Proc. SPIE **5040**, 742–752 (2003).

[53] S. Schröder, S. Gliech, and A. Duparré, "Measurement system to determine the total and angle-resolved light scattering of optical components in the deep-ultraviolet and vacuum-ultraviolet spectral regions," Appl. Opt. **44**, 6093–6107 (2005).

[54] T. F. Schiff, J. C. Stover, D. J. Wilson, B. D. Swimley, M. E. Southwood, and D. R. Bjork, "Design review of a unique out-of-plane polarimetric scatterometer," Proc. SPIE **1753**, 262–268 (1992).

[55] F. M. Cady, M. W. Knighton, D. R. Cheever, B. D. Swimley, T. L. Huntdoff, T. F. Schiff, and M. E. Southwood, "A design review of a broadband, three-dimensional scatterometer," Proc. SPIE **1753**, 148–157 (1992).

[56] T. F. Schiff, M. W. Knighton, D. J. Wilson, F. M. Cady, J. C. Stover, and J. J. Butler, "Design review of a high accuracy UV to near IR scatterometer," Proc. SPIE **1995** (1993).

[57] T. A. Germer and C. Asmail, "A goniometric optical scatter instrument for bidirectional reflectance distribution function measurements with out-of-plane and polarimetry capabilities," Proc. SPIE **3141**, 220–231 (1997).

[58] G. Obein, R. Bousquet, and M. E. Nadal, "New NIST Reference Goniospectrometer," Proc. SPIE **5880**, 58800T (2005).

[59] V. B. Podobedov, C. C. Miller, and M. E. Nadal, "Performance of the NIST goniocolorimeter with a broad-band source and multichannel charged coupled device based spectrometer," Rev. Sci. Instrum. **83**, 093108 (2012).

[60] A. Le Lay and Y. Cornil, "REFLET scatterometer for 3D scattered light measurements to improve design and simulations in the automotive industry," Proc. SPIE **6198**, 619802 (2006).

[61] Opsira GmbH, ed., *product information gonio'2pi*, http://www.opsira.de, last visited: December 03, 2013.

[62] M. Zerrad, M. Lequime, C. Deumié, and C. Amra, "Development of a goniometric light scatter instrument with sample imaging ability," Proc. SPIE **7102**, 710207 (2008).

[63] O. Gilbert, C. Deumié, and C. Amra, "Angle-resolved ellipsometry of scattering patterns from arbitrary surfaces and bulks," Opt. Express **13**, 2403–18 (2005).

[64] M. Zerrad, M. Lequime, and C. Amra, "Multimodal scattering facilities and modelization tools for a comprehensive investigation of optical coatings," Proc. SPIE **8169**, 81690K (2011).

[65] D. Hünerhoff, U. Grusemann, and A. Höpe, "New robot-based gonioreflectometer for measuring spectral diffuse reflection," Metro. **43**, S11–S16 (2006).

[66] OPTIS, ed., *product information OMS4*, http://www.optis-world.com, last visited: December 03, 2013.

[67] K. Jäger, O. Isabella, R. a. C. M. M. van Swaaij, and M. Zeman, "Angular resolved scattering measurements of nano-textured substrates in a broad wavelength range," Meas. Sci. Technol. **22**, 105601 (2011).

[68] P. D. Fuqua, T. Mooney, J. D. Barrie, D. Rock, and H. I. Kim, "Angle resolved scattering from optical filters for space applications incident beam filter array," in "Optical Interference Coatings 2010, Topical Meeting and Tabletop Exhibit," (2010).

[69] P. Apian-Bennewitz, "New scanning gonio-photometer for extended BRTF measurements," Proc. SPIE **7792**, 77920O (2010).

[70] S. Schröder, A. Duparré, and T. Herffurth, "Device and method for angularly resolved scattered light measurement," Patent WO 2,010,127,872 (2010).

[71] J. Stover and E. Hegstrom, "Scatter metrology of photovoltaic textured surfaces," Proc. SPIE **7771**, 777109 (2010).

[72] T. Rinder and H. Rothe, "Performance limits of ARS sensors based on CMOS photodiode array," Proc. SPIE **4779**, 72–82 (2002).

[73] T. Rinder, H. Rothe, and A. Kasper, "Design problems of a calibrated BRDF sensor with respect to dynamic range, speed, and large angle of view," Proc. SPIE **4100**, 136–147 (2000).

[74] O. Apel, C. Goerling, U. Leinhos, K. R. Mann, and B. Schaefer, "Charisma: a new way for angular-resolved scattering measurements," Proc. SPIE **4347**, 569–578 (2001).

[75] Radiant Zemax LLC, ed., *product information IS-SA*, http://www.radiantzemax.com, last visited: December 03, 2013.

[76] A. Kasper and H. Rothe, "Evaluation of in-situ ars sensors for characterizing smooth and rough surfaces," Proc **3426**, 252–261 (1998).

[77] T. Herffurth, S. Schröder, M. Trost, A. Duparré, and A. Tünnermann, "Comprehensive nanostructure and defect analysis using a simple 3d light-scatter sensor," Appl. Opt. **52**, 3279–3287 (2013).

[78] Lambda Research Corp., ed., *product information ScatterScope3D*, http://www.lambdares.com, last visited: December 03, 2013.

[79] T. Rinder and H. Rothe, "Development review of an angle resolved light scatter (ARS) sensor LARISSA," Proc. SPIE **5189**, 116–127 (2003).

[80] C. Hahlweg and H. Rothe, "Vorrichtung zur winkelaufgelösten Streulichtmessung mit einem teilhemisphärischen elliptischen Hohlspiegel," Patent DE 102,008,036,928 (2010).

[81] OptoSurf GmbH, ed., *product information OptoSurf*, http://www.optosurf.de, last visited: December 03, 2013.

[82] M. Zerrad, M. Lequime, S. Liukaityte, and C. Amra, "Spatially-resolved surface topography retrieved from far-field intensity scattering measurements," in "Optical Interference Coatings 2013, Topical Meeting and Tabletop Exhibit," (2013).

[83] U. Binder, G. Sauter, W. Steudtner, G. Trebbin, and N. Wagner, "Goniophotometer," Patent EP 1,621,871 (2006).

[84] J. C. Stover, J. A. Bender, M. Bernt, D. R. Bjork, P. Chausse, D. R. Cheever, Kirchner Kelly, T. F. Schiff, and V. C. Skurdal, "Modular scatterometer with interchangeable scanning heads," Patent US 5,196,906 (1993).

[85] R. J. Castonguay, "Omniscatr: a high-speed, high-resolution three-dimensional scatterometer measures complex scatter interference and diffraction patterns," Proc. SPIE **2260**, 212–224 (1994).

[86] H. Rothe, A. Kasper, P. Riedel, O. Specht, and W. Mueller, "Bidirectional reflectance distribution function (BRDF) sensing with fiber optics, programmable laser diodes, and high-resolution CCD arrays," Proc. SPIE **2260**, 83–92 (1994).

[87] T. A. Germer, "Multidetector hemispherical polarized optical scattering instrument," Proc. SPIE **3784**, 304–313 (1999).

[88] M. Trost, S. Schröder, T. Feigl, A. Duparré, and A. Tünnermann, "Influence of the substrate finish and thin film roughness on the optical performance of Mo/Si multilayers," Appl. Opt. **50**, C148–C153 (2011).

[89] Brookhaven Instruments Corporation, ed., *product information BI-200SM*, http://www.brookhaveninstruments.com, last visited: December 03, 2013.

[90] LS Instruments AG, ed., *product information LS Spectrometer*, http://www.lsinstruments.ch, last visited: December 03, 2013.

[91] S. O. Rice, "Reflection of electromagnetic waves from slightly rough surfaces," Commun. Pure. Appl. Math. **4**, 351–378 (1951).

[92] E. L. Church, H. A. Jenkinson, and J. M. Zavada, "Measurement of the finish of diamond-turned metal surfaces by differential light scattering," Opt. Eng. **16**, 360–374 (1977).

[93] E. L. Church, H. A. Jenkinson, and J. M. Zavada, "Relationship between surface scattering and microtopographic features," Opt. Eng. **18**, 125–136 (1979).

[94] J. M. Elson and J. M. Bennett, "Relation between the angular dependence of scattering and the statistical properties of optical surfaces," J. Opt. Soc. Am. **69**, 31–47 (1979).

[95] C. Ruppe and A. Duparré, "Roughness analysis of optical films and substrates by atomic force microscopy," Thin Solid Films **288**, 8–13 (1996).

[96] E. L. Church and P. Takacs, "Surface Scattering," in "Handbook of Optics," , vol. 1, M. Bass, ed. (McGraw-Hill New York, 1995), chap. 7, pp. 7.1–7.16.

[97] J. E. Harvey, A. Krywonos, and C. L. Vernold, "Modified beckmann-kirchhoff scattering model for rough surfaces with large incident and scattering angles," Opt. Eng. **46**, 078002 (2007).

[98] S. Schröder, A. Duparré, L. Coriand, A. Tünnermann, D. H. Penalver, and J. E. Harvey, "Modeling of light scattering in different regimes of surface roughness." Opt. Express **19**, 9820–9835 (2011).

[99] J. M. Elson, J. P. Rahn, and J. M. Bennett, "Light scattering from multilayer optics: comparison of theory and experiment," Appl. Opt. **19**, 669–679 (1980).

[100] P. Bousquet, F. Flory, and P. Roche, "Scattering from multilayer thin films: theory and experiment," J. Opt. Soc. Am. **71**, 1115–1123 (1981).

[101] A. Duparré and S. Kassam, "Relation between light scattering and the microstructure of optical thin films," Appl. Opt. **32**, 5475–5480 (1993).

[102] C. Amra, "Light scattering from multilayer optics. I. Tools of investigation," J. Opt. Soc. Am. A **11**, 197–210 (1994).

[103] D. G. Stearns, D. P. Gaines, D. W. Sweeney, and E. M. Gullikson, "Nonspecular x-ray scattering in a multilayer-coated imaging system," J. Appl. Phys. **84**, 1003–1028 (1998).

[104] J. M. Elson, J. P. Rahn, and J. M. Bennett, "Relationship of the total integrated scattering from multilayer-coated optics to angle of incidence, polarization, correlation length, and roughness cross-correlation properties," Appl. Opt. **22**, 3207–3219 (1983).

[105] A. Duparré and H. Walther, "Surface smoothing and roughening by dielectric thin film deposition," Appl. Opt. **27**, 1393–1395 (1988).

[106] D. Rönnow, "Elastic light scattering by thin films, spectroscopic measurements and analysis," Ph.D. thesis, Uppsala University (1996).

[107] J. C. Stover, S. Schröder, A. von Finck, and A. Duparré, "Estimating hemispherical scatter from incident plane measurements of isotropic samples," Proc. SPIE **8495**, 84950F (2012).

[108] J. C. Stover, S. Schröder, A. von Finck, D. Unglaub, and A. Duparré, "Estimating hemispherical scatter from incident plane measurements of isotropic samples scattering from both bulk and surface irregularities," Proc. SPIE **8838**, 883803 (2013).

[109] DIN 5030-5:1987-12, "Spektrale Strahlungsmessung; Physikalische Empfänger für spektrale Strahlungsmessungen; Begriffe, Kenngrößen, Auswahlkriterien," (1987).

[110] P. R. Norton, "Photodetectors," in "Handbook of Optics," , vol. 1, M. Bass, ed. (McGraw-Hill New York, 1995), chap. 15, pp. 15.1–15.100.

[111] D. K. Zhao, X. Lu, P. R. Gu, and J. F. Tang, "Bidirectional reflectance distribution function (BRDF) measurements on the Whole Space Scatterometer (WSS)," Proc. SPIE **2260**, 168–177 (1994).

[112] C. C. Asmail, J. Hsia, a. Parr, and J. Hoeft, "Rayleigh scattering limits for low-level bidirectional reflectance distribution function measurements," Appl. Opt. **33**, 6084–6091 (1994).

[113] C. C. Asmail, A. C. Parr, and J. J. Hsia, "Rayleigh scattering limits for low-level bidirectional reflectance distribution function measurements: corrigendum," Appl. Opt. **38**, 6027–6028 (1999).

[114] S. Schröder, T. Herffurth, M. Trost, and A. Duparré, "Angle-resolved scattering and reflectance of extreme-ultraviolet multilayer coatings: measurement and analysis," Appl. Opt. **49**, 1503–1512 (2010).

[115] F. B. Leloup, S. Forment, P. Dutré, M. R. Pointer, and P. Hanselaer, "Design of an instrument for measuring the spectral bidirectional scatter distribution function," Appl. Opt. **47**, 5454–5467 (2008).

[116] M. Flemming, "Experimentelle Untersuchungen zur Strahlformung und Signaldetektion im tiefen ultravioletten Spektralbreich," Diplomarbeit, Hochschule Zwickau (2000).

[117] J. E. Proctor and P. Barnes, "NIST high accuracy reference reflectometer-spectrophotometer," J. Res. Natl. Inst. Stand. Technol. **101**, 619–627 (1996).

[118] H. J. Patrick, C. J. Zarobila, T. A. Germer, V. a. Ying, C. a. Cooksey, and B. K. Tsai, "Tunable supercontinuum fiber laser source for BRDF measurements in the STARR II gonioreflectometer," Proc. SPIE **8495**, 84950K (2012).

[119] S. Schröder, D. Unglaub, M. Trost, and A. Duparré, "Spectral angle resolved scattering of thin film coatings," in "Optical Interference Coatings 2013, Topical Meeting and Tabletop Exhibit," (2013).

[120] W. Zhang, F. Wang, Z. Wang, and H. Wang, "Measuring of spectral BRDF using fiber optic spectrometer," Proc. SPIE **7658**, 76582P (2010).

[121] S. J. Wein, "Small-angle scattering measurement," Ph.D. thesis, University of Arizona (1989).

[122] T. Weigel, "Konzeption, Aufbau und Steuerung eines zweidimensionalen Scatterometers," Ph.D. thesis, Friedrich-Schiller-Universität Jena (1991).

[123] DIN 5032-1:1999-04, "Lichtmessung - Teil 1: Photometrische Verfahren," (1999).

[124] F. M. Cady, J. C. Stover, T. F. Schiff, K. A. Klicker, and D. R. Bjork, "Measurement of very near specular scatter," Proc. SPIE **967**, 264–271 (1988).

[125] J. C. Stover and M. Bernt, "Very near specular measurement via incident angle scaling," Proc. SPIE **1753**, 115–120 (1992).

[126] D. Malacara and Z. Malacara, *Handbook of Optical Design* (Marcel Dekker Inc, New York, 2004), 2nd ed.

[127] Radiant Zemax LLC, ed., *Zemax Manual*, http://www.radiantzemax.com, last visited: December 03, 2013.

[128] Hamamatsu, ed., *Photomultiplier Tubes - Basics and Application*, http://www.hamamatsu.com, last visited: December 03, 2013, 3rd ed. (2006).

[129] Hamamatsu Photonics Deutschland GmbH, ed., *product information Hamamatsu R1463*, http://www.hamamatsu.com, last visited: December 03, 2013.

[130] *Software written by S. Gliech and M. Hauptvogel, Fraunhofer IOF, Jena.*

[131] D. Unglaub, "Weiterentwicklung und Optimierung eines bestehenden Table-Top Streulichtmesssystems," bachelor thesis, Ernst-Abbe Fachhochschule Jena (2011).

[132] Labsphere Inc., ed., *product information Spectralon*, http://www.labsphere.com, last visited: December 03, 2013.

[133] M. Zerrad and M. Lequime, "Instantaneous spatially resolved acquisition of polarimetric and angular scattering properties in optical coatings," Appl. Opt. **50**, C217–C221 (2011).

[134] J. E. Flood, "Transmission Principles," in "Telecommuniation Networks," , J. E. Flood, ed. (The Institution of Electrical Engineers, London, 1997), chap. 3, 2nd ed.

[135] H. Sari, G. Karam, and I. Jeanclaude, "Transmission techniques for digital terrestrial tv broadcasting," IEEE Commun. Mag. **33**, 100–109 (1995).

[136] A. von Finck, M. Trost, A. Duparré, and G. Notni, "Verfahren und Anordnung zur Streulichtmessung," Patent Application Publication DE 102,011,118,607 (2011).

[137] M. L. Meade, *Lock-in amplifiers: principles and applications* (Peregrinus, on behalf of the IEE, London, 1983).

[138] E. Marin and R. Ivanov, "LIA in a nut shell: How can trigonometry help to understand lock-in amplifier operation?" Lat. Am. J. Phys. Educ. **3**, 544–546 (2009).

[139] K. G. Libbrecht, E. D. Black, and C. M. Hirata, "A basic lock-in amplifier experiment for the undergraduate laboratory," Am. J. Phys. **71**, 1208–1213 (2003).

[140] M. L. Meade, "Advances in lock-in amplifiers," J. Phys. E: Sci. Instrum. **15**, 395–493 (1982).

[141] A. Antoniou, *Digital Filters: Analysis, Design, and Applications* (McGraw-Hill, New York, 2001).

[142] Y. Wu and W. Zou, "Orthogonal frequency division multiplexing: a multi-carrier modulation scheme," IEEE Trans. Consumer Electron. **41**, 392–399 (1995).

[143] S. Weinstein, "The history of orthogonal frequency division multiplexing," IEEE Commun. Mag. **47**, 26–35 (2009).

[144] A. von Finck, M. Hauptvogel, and A. Duparré, "Instrument for close-to-process light scatter measurements of thin film coatings and substrates," Appl. Opt. **50**, C321–C328 (2011).

[145] Radiant Zemax LLC, *Zemax*, http://www.radiantzemax.com, last visited: December 03, 2013.

[146] E. C. Fest, "Data reduction of BSDF measurements from curved surfaces," Proc. SPIE **7069**, 70690K (2008).

[147] M. Born and E. Wolf, *Principles of Optics (7th ed.)* (Cambridge University Press, Cambridge, 1999), chap. 14.5.

[148] G. Peterson, "Analytic expression for in-field scattered light distribution," Proc. SPIE **5178**, 184–193 (2004).

[149] J. E. Harvey, N. Choi, A. Krywonos, G. Peterson, and M. Bruner, "Image degradation due to scattering effects in two-mirror telescopes," Opt. Eng. **49**, 063202 (2010).

[150] N. Choi and J. E. Harvey, "Image degradation due to surface scatter in the presence of aberrations," Appl. Opt. **51**, 535–46 (2012).

[151] K. Klicker, J. C. Stover, and D. J. Wilson, "Near specular scatter measurement techniques for curved samples," Proc. SPIE **967**, 255–263 (1988).

[152] *AFM / WLI measurements and PSD calculations performed by Dr. Luisa Coriand and Christian Wiede, Fraunhofer IOF, Jena.*

[153] Phonton Engineering, L.L.C., *FRED*, http://www.photonengr.com/software, last visited: December 03, 2013.

[154] N. C. Barford, *Experimental measurements: precision, error and truth*, vol. 2 (Addison Wesley Pub. Co., 1967).

[155] K. Birch, *Measurement Good Practice Guide No. 36 - Estimating Uncertainties in Testing*, vol. 2 (British Measurement and Testing Association, 2003).

[156] JCGM 100:2008, "Evaluation of measurement data - Guide to the expression of uncertainty in measurement (GUM)," (2008).

[157] F. M. Cady, D. R. Bjork, J. Rifkin, and J. C. Stover, "BRDF Error Analysis," Proc. SPIE **1165**, 154–164 (1990).

[158] A. Höpe and K.-O. Hauer, "Three-dimensional appearance characterization of diffuse standard reflection materials," Metro. **47**, 295–304 (2010).

[159] S. Yang, I. Vayshenker, X. Li, and T. R. Scott, "Optical detector nonlinearity: A comparision of five methods," in "Proc. Conf. Precision Electromagnetic Measurement," (1994), pp. 455–456.

[160] S. Yang, I. Vayshenker, X. Li, and T. Scott, "Accurate measurement of optical detector nonlinearity," in "Proc. National Conference Standards Laboratories Workshop & Symposium," (1994), pp. 353–362.

[161] K. D. Mielenz and K. L. Eckerle, "Spectrophotometer linearity testing using the double-aperture method," Appl. Opt. **11**, 2294–303 (1972).

[162] X. Li, T. Scott, S. Yang, C. Cromer, and M. Dowell, "Nonlinearity measurements of high-power laser detectors at NIST," J. Res. Natl. Inst. Stand. Technol. **109**, 429–434 (2004).

[163] B. R. L. Siebert and K.-D. Sommer, "Weiterentwicklung des GUM und Monte-Carlo-Techniken (New developments of the GUM and Monte Carlo techniques)," Technisches Messen **71**, 67–80 (2004).

[164] The MathWorks, Inc., *Matlab*, http://www.mathworks.com, last visited: December 03, 2013.

[165] J. Ohtsubo, "Measurement of diamond-turned metal surface by light scattering," Proc. Soc. Photo-Opt. Instrum. Eng **558**, 80–84 (1985).

[166] J. Ohtsubo, "Measurement of roughness properties of diamond-turned metal surfaces using light-scattering method," J. Opt. Soc. Am. A **3**, 982–987 (1986).

[167] J. C. Stover, "Light Scatter Metrology of Diamond Turned Optics," Proc. SPIE **5878**, 58780R (2005).

[168] S. Gliech, R. Wendt, and A. Duparré, "Uv-vis-nir scatter measurement methods for ultra precision surfaces and coatings," in "Optical Interference Coatings 2007, Topical Meeting and Tabletop Exhibit," (2007).

[169] S. Schröder and A. Duparré, "Finish assessment of complex surfaces by advanced light scattering techniques," Proc. SPIE **7102**, 71020F (2008).

[170] A. von Finck, T. Herffurth, M. Hauptvogel, and A. Duparré, "Symmetry and anisotropy ars analysis of optical components," in "OSD - Optical Systems Design - Optical Fabrication, Testing, and Metrology IV," (2011).

[171] *Sample fabricated by M. Rohde, Fraunhofer IOF Jena.*

[172] *Sample fabricated by A. Gebhardt, Fraunhofer IOF Jena.*

[173] M. Flemming, "Methoden der Simulation und Charakterisierung von nanostrukturierten ultrahydrophoben Oberflächen für optische Anwendungen," Ph.D. thesis, Technische Universität Ilmenau (2006).

[174] F. Kienberger, V. Pastushenko, G. Kada, T. Puntheeranurak, L. Chtcheglova, C. Riethmueller, C. Rankl, A. Ebner, and P. Hinterdorfer, "Improving the contrast of topographical AFM images by a simple averaging filter," Ultramicroscopy **106**, 822 – 828 (2006).

[175] T. Herffurth, "Light scatter and roughness analysis of optical surfaces and multilayer systems," Ph.D. thesis, Friedrich-Schiller Universität Jena (to be published 2014).

[176] Y. Wang and W. Wolfe, "Scattering from microrough surfaces: comparison of theory and experiment," J. Opt. Soc. Am. **73**, 1596–1602 (1983).

[177] J. C. Stover, J. Rifkin, D. R. Cheever, K. H. Kirchner, and T. F. Schiff, "Comparison of wavelength scaling data to experiment," Proc. SPIE **967**, 44–49 (1988).

[178] J. Stover, M. Bernt, D. E. McGary, and J. Rifkin, "An investigation of anomalous scatter from beryllium mirrors," Proc. SPIE **1165**, 100–109 (1989). R.

[179] J. Elson, J. M. Bennett, and J. C. Stover, "Wavelength and angular dependence of light scattering from beryllium: comparison of theory and experiment." Appl. Opt. **32**, 3362–3376 (1993).

[180] *AFM / WLI measurements and PSD calculations performed by Christian Wiede and Nadja Felde, Fraunhofer IOF, Jena.*

[181] *Sample fabricated by T. Müller, Fraunhofer IOF Jena.*

[182] *Sample fabricated by M. Schürmann, Fraunhofer IOF Jena.*

[183] D. Rönnow, "Interface roughness statistics of thin films from angle-resolved light scattering at three wavelengths," Opt. Eng. **37**, 696–704 (1998).

[184] A. von Finck, T. Herffurth, S. Schröder, and A. Duparré, "Characterization of optical coatings using a multisource table-top scatterometer," Appl. Opt. **53**, A259–A269 (2014).

[185] M. Tolkowsky, *Diamond Design: A Study of the Reflection and Refraction of Light in a Diamond*, 3rd ed. (Spon & Chamberlain, New York, Bellingham, Wash., 1919).

[186] D. Jeffries, *A Treatise on Diamonds and Pearls* (C. and J. Ackers, London, 1751).

[187] B. D. Green, A. Gilbertson, I. Reinitz, M. L. Johnson, and J. E. Shigley, "What did Marcel Tolkowsky really say," GIA on Diamonds (2001).

[188] T. H. Scott, I. M. Reinitz, M. L. Johnson, and J. E. Shigley, "Modeling the appearance of the round brilliant cut diamond: An analysis of brilliance," Gems Gemol. **34**, 158–183 (1998).

[189] A. Vasiliev and B. Harding, "Optimizing faceting for beauty," J. Gemol. **29**, 24–35 (2004). Translated by Bruce L. Harding from the Russian Gemological Bulletin, 2002, 5(2), 33-41.

[190] B. P. Yantzer, J. Caudill, and J. Sasián, *Foundation, Research Results and Application of the New AGS Cut Grading System*, available online at www.agslab.com, last visited: December 03, 2013 (2005).

[191] GIA (ed.), "Estimating a cut grade using the gia diamond cut grading system," available online at https://www.diamondcut.gia.edu (2009).

[192] T. Moses, M. Johnson, B. Green, T. Blodgett, K. Cino, R. H. Geurts, A. M. Gilbertson, T. H. Scott, J. M. King, L. Kornyla, I. M. Reinitz, and J. E. Shigley, "A foundation for grading the overall cut quality of round brilliant cut diamonds," Gems Gemol. **40**, 202–228 (2004).

[193] J. S. Dodson, "A statistical assessment of brilliance and fire for the round brilliant cut diamond," Opt. Acta. **25**, 681–692 (1978).

[194] J. Sasián, J. Quick, J. Caudill, and P. Yantzer, "Evaluation of brilliance, fire, and scintillation in round brilliant gemstones," Opt. Eng. **46**, 093604 (2007).

[195] Original picture taken from: S. Rösch, "IV. Beitrag zum Brillanzproblem," Zeitschrift für Kristallographie **65**, 46–68 (1927).

[196] Sarin Technologies Ltd., ed., *product information DiaScan S+*, http://www.sarin.com, last visited: December 03, 2013.

[197] Sarin Technologies Ltd., ed., *product information DiaMension*, http://www.sarin.com, last visited: December 03, 2013.

[198] OGI Systems Ltd., ed., *product information MegaScope*, http://ogisystems.com, last visited: December 03, 2013.

[199] OGI Systems Ltd., ed., *product information Scanox Proportion HD*, http://ogisystems.com, last visited: December 03, 2013.

[200] I. M. Reinitz, M. L. Johnson, J. E. Shigley, and T. S. Hemphill, "Systems and methods for evaluating the appearance of a gemstone," Patent US 7,834,987 (2010).

[201] I. Reinitz, K. Yantzer, M. Johnson, T. Blodgett, R. H. Geurts, and A. M. Gilbertson, "Proportion measurement: Tolerances for the GIA Diamond Cut Grading System," Rapaport Diamond Report **8**, 34–39 (2005).

[202] T. Blodgett, R. Geurts, and A. Gilbertson, "System and method for gemstone cut grading," Patent US 7,571,060 (2009).

[203] T. Shigetomi and K. Inoue, "Device for judging brilliancy of precious stones such as diamonds or the like," Patent US 4,647,194 (1987).

[204] A. Gilbertson, "Device for judging symmetry, brightness, and efficiency of light return in precious stones," Patent US 6,665,058 (2003).

[205] J. Sasián, J. Caudill, and P. Yantzer, "Methods, apparatus, and systems for evaluating gemstones," Patent US 7,336,347 (2008).

[206] T. Blodgett, R. Geurts, A. Gilbertson, A. Lucas, D. Pay, I. Reinitz, J. Shigley, K. Yantzer, and C. Zink, *Finish, culet size, and girdle thickness: Categories of the GIA diamond cut grading system*, available online at http://www.diamondcut.gia.edu, last visited: December 03, 2013 (2009).

[207] I. Reinitz, M. Johnson, T. S. Hemphill, A. M. Gilbertson, R. H. Geurts, B. D. Green, and J. E. Shigley, "Modeling the appearance of the round brilliant cut diamond: An analysis of fire, and more about brilliance," Gems Gemol. **37**, 174–197 (2001).

[208] J. Sasián, P. Yantzer, and T. Tivol, "The optical design of gemstones," Opt. Photonics News **14**, 25–29 (2003).

[209] G. Notni, P. Kühmstedt, I. Schmidt, and C. Großmann, "Dual-beam CT for measurements of precision mechanical components and optical systems," in "High-resolution X-ray CT Symposium," (2010).

[210] *CT measurements by Ingo Schmidt, Fraunhofer IOF, Jena.*

[211] *Plane fitting by Franz Mueller, Fraunhofer IOF, Jena.*

[212] Autodesc Inc., *Autodesc Inventor*, http://www.autodesk.de, last visited: December 03, 2013.

[213] *WLI measurements and PSD calculations performed by Erik Forwerk, Fraunhofer IOF, Jena.*

[214] *Brilliant provided by W. Mann, Goldschmied Mann, Jena.*

[215] *Sample provided by Dr. M. Sauer, Swarovski KG.*

[216] *Contact: Dr. John Stover, The Scatter Works.*

[217] *Contact: Dominic Doyle, European Space Agency ESTEC, Optics Section (TEC-MMO).*

[218] *Contact: Prof. Dr. Stefan Sinzinger, TU-Ilmenau, Fachgebiet Technische Optik.*

[219] *Contact: Dr. Marcus Sauer, D. Swarovski KG, Applied Research.*

Nomenclature

ACF	autocorrelation function
AFM	atomic force microscope
ARS	angle resolved scattering
CCD	charge-coupled device
CMOS	complementary metal–oxide–semiconductor
CT	computer tomography
DC	direct current
DR	dynamic range
EUV	extreme ultraviolet
FDM	frequency division multiplexing
FIR	far infrared
FOV	field of view
GUM	guide to the expression of uncertainty in measurement
IP	in-plane
LIA	lock-in-amplifier
MC	Monte Carlo (simulation)
NA	numerical aperture
ND	neutral density (filter)
NEARS	noise equivalent ARS
NIR	near infrared
OOM	orders of magnitude
OOP	out-of-plane
PDF	propability distribution function
PH	pinhole
PMT	photo multiplier tubes

POP	physical optics propagation
PSD	power spectral density function
PSF	point spread function
SNR	signal-to-noise ratio
SSA	single surface approximation
TIS	total integrated scattering
TS	total scattering
UP	ultra-precision (diamond turned)
UV	ultraviolet
VIS	visible spectrum
WLI	white light interferometer

Acknowledgments

I want to thank a number of people without whom this work would not have been possible.

I address my special gratitude to my supervisor, Prof. Dr. Stefan Sinzinger (Technische Universität Ilmenau), whose constructive directions in an encouraging atmosphere from the initial conception stage up to the end were a precondition for this thesis.

I would particularly like to thank Dr. Angela Duparré (Fraunhofer Institute for Applied Optics and Precision Engineering (IOF), Jena), for her support, guidance, and constructive criticism throughout my work at Fraunhofer IOF. Her counseling as well as her readiness for professional discussions had a significant impact on this thesis.

I also am deeply indebted to all my colleagues at the IOF Optical Systems Department headed by Dr. Gunther Notni. Especially I want to thank the other "scatter guys" Dr. Sven Schröder, Tobias Herffurth, Markus Trost, Matthias Hauptvogel, and David Unglaub for very helpful and numerous discussions. Special thanks go to Matthias Hauptvogel for providing a reliable and comprehensive control software that enabled even the most complicated measurement tasks. Also I want to thank Dr. Luisa Coriand, Christian Wiede, and Nadja Felde for the AFM and WLI measurements and according discussions. Furthermore I also address special gratitude to Uwe Lippman for the enlightening discussions regarding optical simulations. Another special thanks go to Ingo Schmidt and Franz Müller for the delicate CT measurement and the CAD export of the diamond cut.

My gratitude extends to all those who provided me with the required samples, in particular Dr. Mark Schürmann, Dr. Peter Munzert, Friedrich Rickelt, and Thomas Müller for diverse optical coatings. I also want to thank Andreas Gebhardt and Matthias Rohde for the manufacturing of the diamond turned and polished surfaces. I would like to thank Dr. Markus Sauer and Karl-Heinz Eder (Swarovski KG) for the supply of high quality brilliant cut diamonds.

Many thanks to Dr. John Stover (The Scatter Works, Inc., Tucson, Arizona) for his subtle technical hints during on-site discussions.

Let me express my special thanks to Prof. Dr. Peter Ott (Hochschule Heilbronn) and Prof. Dr. Michael Pfeffer (Hochschule Ravensburg-Weingarten) for guiding my interest towards optical engineering.

I also want to thank Gabriele Gomez-Hartmann, Bjørn Burkardt, and Kathrin Stilla for very helpful final proof-readings.

I am deeply grateful to my family for their unlimited support, motivation, and patience throughout the past years, which contributed an essential part to the accomplishment of this thesis.

Ehrenwörtliche Erklärung

Ich versichere, dass ich die vorliegende Arbeit ohne unzulässige Hilfe Dritter und ohne Benutzung anderer als der angegebenen Hilfsmittel angefertigt habe. Die aus anderen Quellen direkt oder indirekt übernommenen Daten und Konzepte sind unter Angabe der Quelle gekennzeichnet.

Bei der Auswahl und Auswertung folgenden Materials haben mir die nachstehend aufgeführten Personen in der jeweils beschriebenen Weise unentgeltlich geholfen:

1. Dr. Mark Schürmann, Dr. Peter Munzert, Friedrich Rickelt und Thomas Müller (alle Fraunhofer IOF): Herstellung diverser Schichten.
2. Andreas Gebhardt und Matthias Rohde (alle Fraunhofer IOF): Herstellung von UP diamant gedrehten Oberflächen.
3. Matthias Hauptvogel (Fraunhofer IOF): Erstellung der Software zur Ansteuerung und Automatisierung.
4. David Unglaub (Fraunhofer IOF): Konstruktion eines motorisierten X/Y-Probentisches, einer Justagevorrichtung und Aperturblenden im Rahmen einer von mir betreuten Bachelor Arbeit.
5. Ingo Schmidt und Franz Müller (beide Fraunhofer IOF): CT Messung und CAD Export eines geschliffenen Brillanten.
6. Dr. Luisa Coriand, Christina Wiede, Nadja Felde, und Erik Forwerk (alle Fraunhofer IOF): AFM / WLI Messungen und Unterstützung bei PSD Berechnung.
7. Dr. Markus Sauer und Karl-Heinz Eder (Swarovski KG): Bereitstellung hochwertig geschliffener Brillanten.

Weitere Personen waren an der inhaltlich-materiellen Erstellung der vorliegenden Arbeit nicht beteiligt. Insbesondere habe ich hierfür nicht die entgeltliche Hilfe von Vermittlungs- bzw. Beratungsdiensten (Promotionsberater oder anderer Personen) in Anspruch genommen. Niemand hat von mir unmittelbar oder mittelbar geldwerte Leistungen für Arbeiten erhalten, die im Zusammenhang mit dem Inhalte der vorgelegten Dissertation stehen.

Die Arbeit wurde bisher weder im In- noch im Ausland in gleicher oder ähnlicher Form einer Prüfungsbehörde vorgelegt. Ich bin darauf hingewiesen worden, dass die Unrichtigkeit der vorstehenden Erklärung als Täuschungsversuch bewertet wird und gemäß § 7 Abs. 8 der Promotionsordnung den Abbruch des Promotionsverfahrens zur Folge hat.

(Ort, Datum) (Unterschrift)